論文 / 著書情報
Article / Book Information

題目(和文)	マイクロ流路を用いた二相液滴の生成とポリマー粒子生成への応用
Title(English)	Microfluidic formation of biphasic droplets and their application in fabrication of polymer particles
著者(和文)	XUSiyuan
Author(English)	Siyuan Xu
出典(和文)	学位:博士(工学), 学位授与機関:東京工業大学, 報告番号:甲第11921号, 授与年月日:2021年3月26日, 学位の種別:課程博士, 審査員:西迫 貴志,初澤 毅,進士 忠彦,柳田 保子,石田 忠
Citation(English)	Degree:Doctor (Engineering), Conferring organization: Tokyo Institute of Technology, Report number:甲第11921号, Conferred date:2021/3/26, Degree Type:Course doctor, Examiner:,,,,
学位種別(和文)	博士論文
Category(English)	Doctoral Thesis
種別(和文)	要約
Type(English)	Outline

東京工業大学

2020 年度　博士論文

Microfluidic formation of biphasic droplets and their application in fabrication of polymer particles

指導教員　西迫 貴志　准教授

工学院 機械系

学籍氏名　XU SIYUAN

Table of Contents

Chapter 1 Introduction

Chapter 2 Janus-to-core-shell transition of microfluidic biphasic droplets

Acknowledgement

Achievements

Chapter 1

Introduction

1.1 Background

1.1.1 Simple and complex emulsions

The term of emulsions is the metastable mixture system of two naturally immiscible liquid phases where one liquid is dispersed in the other one. In this case, the formerly dispersed liquid (droplets) is called the disperse phase, and the latter liquid is called the continuous phase. Typically, two types of emulsions can be formed. One is oil-in-water (O/W) emulsion, in which oil is the dispersed phase and water is the continuous phase. The other is a water-in-oil (W/O) type, in which water is the dispersed phase and oil is the continuous phase (Fig. 1.1a-b). More complex emulsions including double emulsions or Janus emulsions have been produced. For example, water-in-oil-water (W/O/W) emulsion is a double emulsion in which W/O emulsion is dispersed in the second aqueous phase [1,2] (Fig. 1.1c). On the other hand, Janus emulsion [3,4] contains droplets comprised of two partially engulfed liquids, dispersed in the continuous phase (Fig. 1.1d).

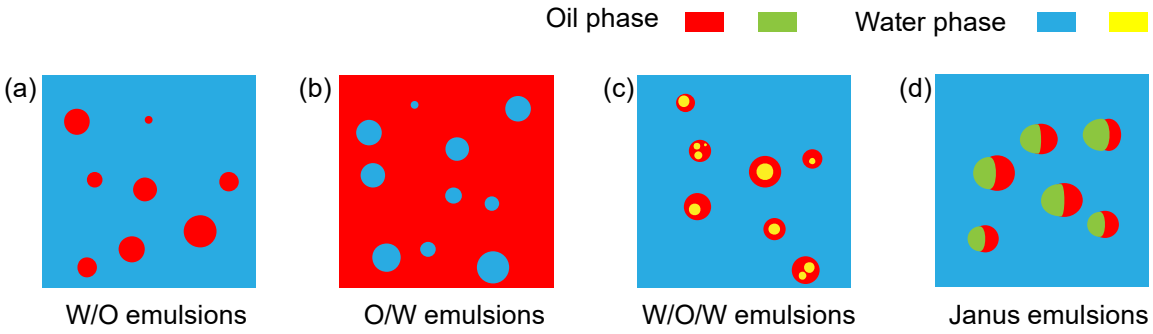

Figure 1.1 Different types of emulsions. (a)Water-in-oil (W/O) emulsion. (b) Oil-in-water (O/W) emulsion. (c) Water-in-oil-in-water (W/O/W) double emulsion. (d) Janus emulsions.

Recently, complex emulsions have been attracting great interest because of their significant potential in many applications such as foods [5], pharmaceuticals [6], cosmetics [7], materials [8], and chemical separations [9].

1.1.2 Conventional methods for producing complex emulsions

(1) Mechanical methods

Typically, the complex emulsions containing biphasic droplets can be prepared by using a rotor-stator homogenizer [10]. For example, W/O/W double emulsion was prepared following a two-step emulsification method. In the first step, the premixed emulsion of W/O was prepared using the rotor-stator homogenizer (Fig. 1.2a). Initially, the premixed solution (i.e., coarse oil-water mixture) was contained in a syringe. Then the solution was pushed into the gap between the rotating rotor and the immobile stator. The sheared emulsion could be recovered at the top of the device. In the second step, the primary premixed W/O emulsion was introduced into the water phase similarly, and the W/O/W double emulsion could be prepared (Fig. 1.2b).

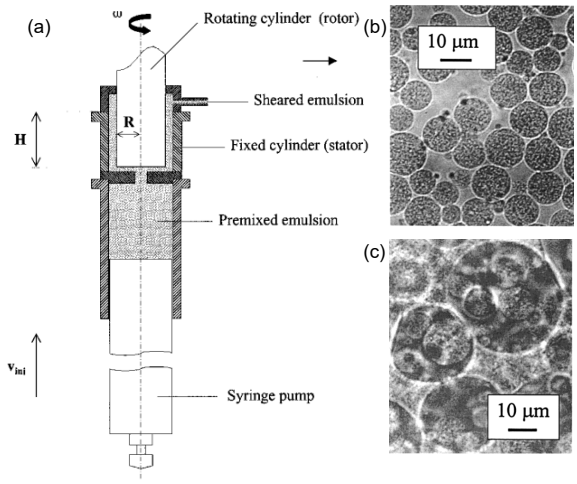

Figure 1.2 Preparation of W/O/W double emulsions [10]. (a) rotor-stator homogenizers. (b) Microscopic image of a typical W/O/W double emulsion. (c) W/O/W/O emulsion obtained when premixed W/O emulsions introduced too fast.

This method can produce W/O/W double emulsion continuously. However, it is necessary to introduce the premixed W/O emulsion into the water at a slow rate (around

0.5 cm^3 every 5 s), because rapid infusion might result in unintended complex structures (Fig. 1.2c).

To prepare Janus emulsions, the mechanical method of one-step vortex mixing could be used [11]. By mixing three immiscible solutions in a tube using a simple vortex mixer, Janus droplets were produced as shown in Fig. 1.3. This approach had the advantages of the simple, scalable, wide size range of formation. However, the droplets had a broad size distribution, and the emulsification process needed to operate for a long-time duration (approximately 2 min).

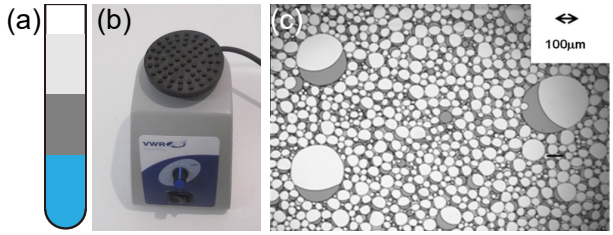

Figure 1.3 Janus emulsion prepared by one-step vortex mixing [11]. (a) Three immiscible solutions in a tube. (b) A vortex mixer used for emulsification. (c) Optical microscopy image of the prepared Janus emulsions.

(2) Membrane emulsification

In membrane emulsification, a pressurized disperse phase permeates through the pores of the membrane and forms droplets, while the continuous phase follows along the membrane surface [12]. For example, a microporous glass membrane protocol was reported to produce W/O/W double emulsions, as shown in Fig. 1.4 [13]. This system consists of (a) a membrane module; (b) a nitrogen gas tank for supplying pressure; (c) a dispersion phase storage tank; (d) an emulsion tank; and (e) a circulation pump. First, the W/O emulsion droplets were prepared via homogenization. Then, the product was added to the water phase through the hydrophilic microporous membrane.

In this method, the size of the droplets could be controlled by changing the pore size of the membrane. Also, membrane systems were suitable for large scale production because it is easy to add more membrane modules. The produced emulsions are quasi-monodisperse, with the coefficient of variation (CV) values around 10%.

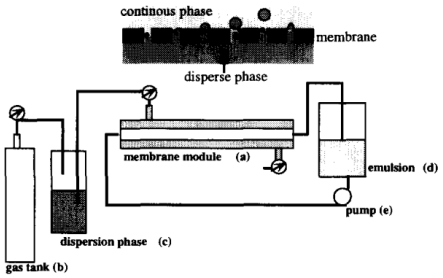

Figure 1.4 Schematic diagram of membrane emulsification [13]

(3) Microchannel (MC) emulsification

The MC emulsification uses lithographically fabricated microdevices, and it exploits the interfacial tension as the driving force to produce droplets effectively [14]. During the droplet formation process, the disperse phase is forced into the microfabricated MC arrays, forming disk-like shapes on the 'terrace' at the exit of the channels. Then, the interfacial tension drives the disk-shaped dispersed phase to transform into spherical droplets at the edge of the terrace spontaneously. One example of the device for MC emulsification is shown in Fig. 1.5. The device consists of a silicon MC plate and a glass plate. The silicon MC plate was fabricated by photolithography and orientation-dependent etching processes.

W/O/W double emulsions could be prepared by using MC emulsification as the second emulsification step. In the first step, W/O emulsion was prepared via homogenization. Then, W/O/W double emulsion was prepared by pressurizing the prepared W/O emulsions into the external water phase through the MC.

In this method, the direct observation of the emulsification process could be achieved. Also, the droplet size could be controlled by changing the MC geometry.

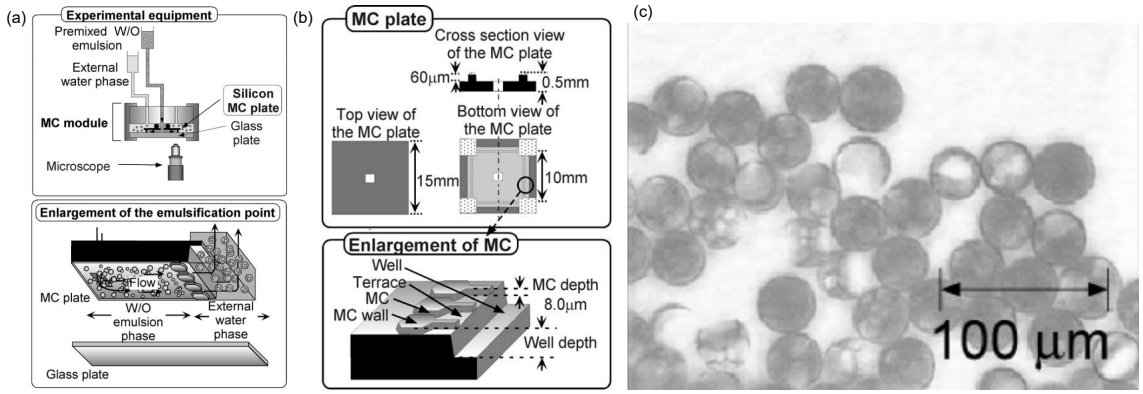

Figure 1.5 Schematic diagram of microchannel (MC) emulsification [14]. (a) Experimental setup; (b) Silicon MC plate; (c) Optical images of prepared W/O/W double emulsions.

(4) Comparison of different emulsification methods

Next, the abovementioned emulsification methods (i.e., mechanical emulsification, membrane emulsification, and MC emulsification) were compared from four aspects.

(a) Range of droplet size

All of the three methods can produce the submicron or micrometer-scale emulsion droplets in the wide size range. In mechanical emulsification, the product size depends on the shear rate of the device. In the membrane emulsification and MC methods, it depends on the size of the micropores or the MCs.

(b) Size distribution

In the mechanical emulsification method, the droplet is generated by the inhomogeneous shear stress in the turbulent field, and the product is considerably polydisperse. In the membrane emulsification method, the droplet tension is produced by the action of the interfacial tension, and the CV value is around 10%. Meanwhile, the MC emulsification can produce monodisperse droplets with the CVs around 5%.

(c) Size tunability

In the mechanical emulsification, the droplets were produced by the rotation speed of the rotor and the flow rate of liquid, and it is possible to control the diameter to some extent. However, precise control is difficult. In the membrane emulsification and MC methods, droplet size depends on pore size or MC size, and it is difficult to vary the droplet size widely in the same apparatus

(d) Applicability for complex emulsions

To produce double emulsions, a two-step emulsification manner was used in all of the three methods. Although Janus droplets could be prepared in a one-step manner using the mechanical method, the product was polydisperse. Meanwhile, membrane emulsification and MC emulsification methods could not be applied to produce Janus emulsions.

Table 1.1 Comparison of different emulsification methods

Method	Droplet size	Size distribution	Size tunability (Independent of the device)	Double/Janus emulsions
Mechanical method	1 to 20 μm	Polydisperse	Yes	Two-step
Membrane emulsification	0.1 and 100 μm	Quasi-monodisperse (CV ~10%)	No	Two-step
MC emulsification	3 to 100 μm	Monodisperse (CV ~5%)	No	Two-step

The above-discussed emulsification methods are summarized in Table 1.1. Based on the discussion, we can understand the disadvantages of each method, and conclude that it is necessary to develop the technique having the following advantages.

(1) The droplet size can be tuned widely in the same device.

(2) The produced droplets are highly monodisperse.

(3) Complex emulsions including double and Janus emulsions can be produced simply and flexibly.

1.2 Droplet microfluidics for complex emulsions

1.2.1 Droplet microfluidics

The definition of microfluidics, described by George M. Whitesides, is the scientific and technical systems that process or manipulate small (10^{-9} to 10^{-18} liters) amounts of fluids, using channels with dimensions of tens to hundreds of micrometers [15]. The origin of the term microfluidics could be traced back to the 1970s when the needs for miniaturization and planarization in biology analyses were proposed. These hopes became reality with the development of microelectromechanical systems (MEMS). By applying the contribution of MEMS, the technique to integrate all typical lab processing on a single microfluidic device often referred to as lab-on-a-chip or micrometer-scale total analysis systems (μTAS) had been successful [16,17].

Among many fields of microfluidics, one subcategory is droplet microfluidics, where the introduction of immiscible multiphase fluids into microchannels forced the formation

and manipulation of droplets. To date, various microfluidic devices with different geometries including T-junction (Fig. 1.6a and b) [18,19], flow-focusing (Fig. 1.7c and d) [20], and co-flowing (Fig. 1.7e) [21] geometries have been developed to produce droplets.

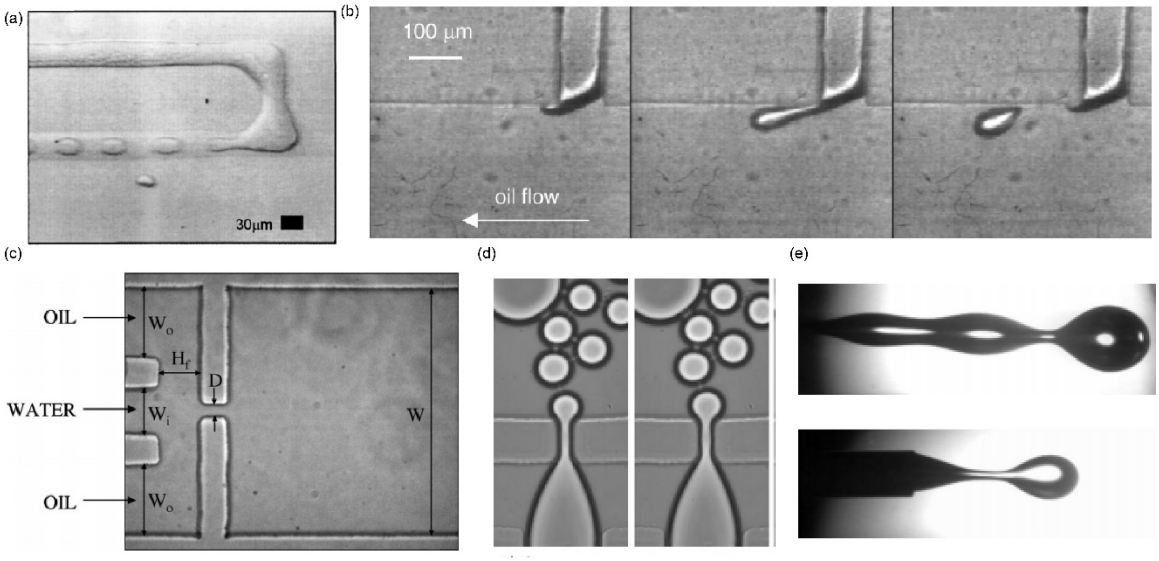

Figure 1.6 Various microfluidic devices for generating W/O emulsion droplets. (a-b) T-junction microfluidic devices for W/O emulsion formation using T-junction microchannels fabricated (a) by soft lithography technology [18]; (b) an end mill [19]; (c) Microfluidic flow-focusing device for generating W/O emulsion droplets [20]. (d) Microscope image of droplets formation using the device in (c). (e) W/O emulsion droplets formed in a co-flowing device at dripping and jetting regime [21].

Compared to other emulsification methods, droplet microfluidics has several extraordinary advantages such as (1) a small volume of reagent consumption; (2) periodically massive generation of droplets with extreme control over size; (3) Wide range variation of the size of the droplets using one device. Owing to these advantages, droplet-based microfluidic technology offered a versatile and promising route to generate droplets.

Recently, droplet microfluidics has extended their function to generate complex emulsions [22,23]. Here, we introduce the microfluidic approach to generate complex emulsions including double emulsions (core-shell droplets) and Janus droplets.

1.2.2 Complex emulsion formation based on surface wettability of microchannels

In droplet microfluidics, the wettability of the microchannel plays an important role because it determines the type of droplets to be generated. The W/O droplets can be generated in the microchannels made of a hydrophobic material, such as polydimethylsiloxane (PDMS). Meanwhile, the O/W droplets can be generated in the microchannels with a hydrophilic material, such as glass.

(a) Core-shell droplets

To generate core-shell droplets, a two-step method with two droplet-generating junctions is generally used. In this method, core drops are generated, and then shell drops encapsulating these core drops are produced in a continuous phase as a separate step. Both PDMS-based and glass-based microfluidic devices have been used to generate core-shell droplets with controlled size.

To generate W/O/W double emulsions, Nisisako et al. designed a glass-based microfluidic device with two T-junctions and modified the wettability of the device walls at a specific junction [24]. In this device, the first junction was modified locally to be hydrophobic for making W/O droplets while the second junction is kept to be hydrophilic for making (W/O)/W droplets. (Fig. 1.7a). The droplets had narrow size distributions with CVs below 3%. Similarly, the authors produced O/W/O droplets by reversing the order of hydrophilic and hydrophobic junctions (Fig. 1.7b). This two-step approach was suitable for controlling the droplet size and number of the inner drops by changing the flow rates.

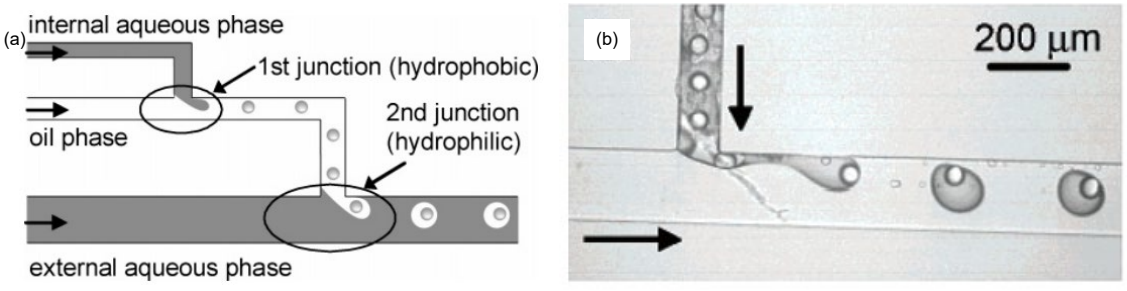

Figure 1.7 W/O/W double emulsions formation [24]. (a) Microfluidic formation of W/O/W double emulsion using T-shaped microchannels. (b) Formation of O/W/O double emulsion at the second hydrophobic T-junction.

Similar two-step double emulsification is also possible using PDMS microfluidic devices with patterned wettability [25]. The upstream junction in Fig. 1.8a had a hydrophilic surface, while the surface of the downstream junction was modified to be hydrophobic. The generated O/W/O droplets are highly monodisperse with CVs below 3%.

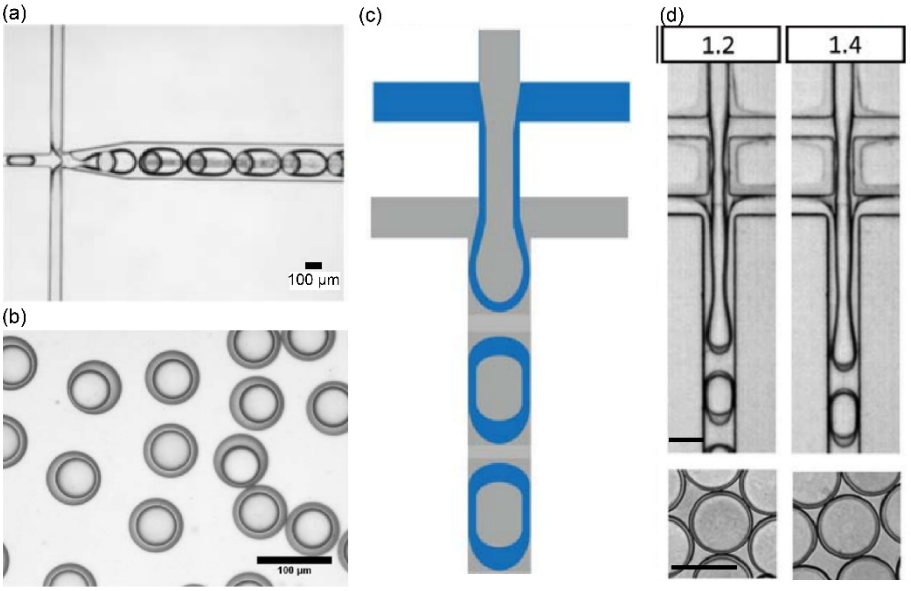

Figure 1.8 Double emulsification in PDMS microfluidic devices. (a-b) Two-step formation of O/W/O double emulsion [25]; (c-d) One-step formation of W/O/W double emulsions [26]. (c) Schematic of one-step double emulsification in a flow-focusing geometry; (d) O/W/O double emulsions produced in one-step manner at different flow conditions. The scale bar: 80 μm.

Abate et al. reported the one-step methods to generate double emulsions using a PDMS microfluidic flow-focusing device. They realized this by increasing the flow rates in the upstream junction and patterning the wettability so that the first junction is hydrophilic and the second junction is hydrophobic, by using a flow-confinement technique [26]. In this way, a jet of the inner phase produced in the first junction would extend into the second junction, forming a coaxial jet flow. Then, the coaxial jet flow was

pinched into double emulsions (Fig. 1.8c,d). This method could produce core-shell droplets with a wide range of shell thickness.

Another straightforward system for generating double emulsions is coaxial microcapillary device. In 2005, Utada et al. reported double emulsification using a 3D glass capillary microfluidic device, as shown in Fig. 1.9a. The device consisted of two cylindrical glass capillary tubes (one of which was a tapered cylindrical) nested within a square glass tube, thus ensuring the good alignment to form a coaxial geometry. Using such a device, the inner fluid and middle fluids flowed in the same direction, forming a co-axial flow, and the outer fluid flowed in the opposite direction. The combination of co-flow and flow-focusing geometry generated the W/O/W double emulsions in a one-step manner [27]. By changing the flow rates, the droplet size and the number of the inner drops could be controlled. Also, the droplet formation regime could be adjusted from dripping to jetting (Fig. 1.9b,c).

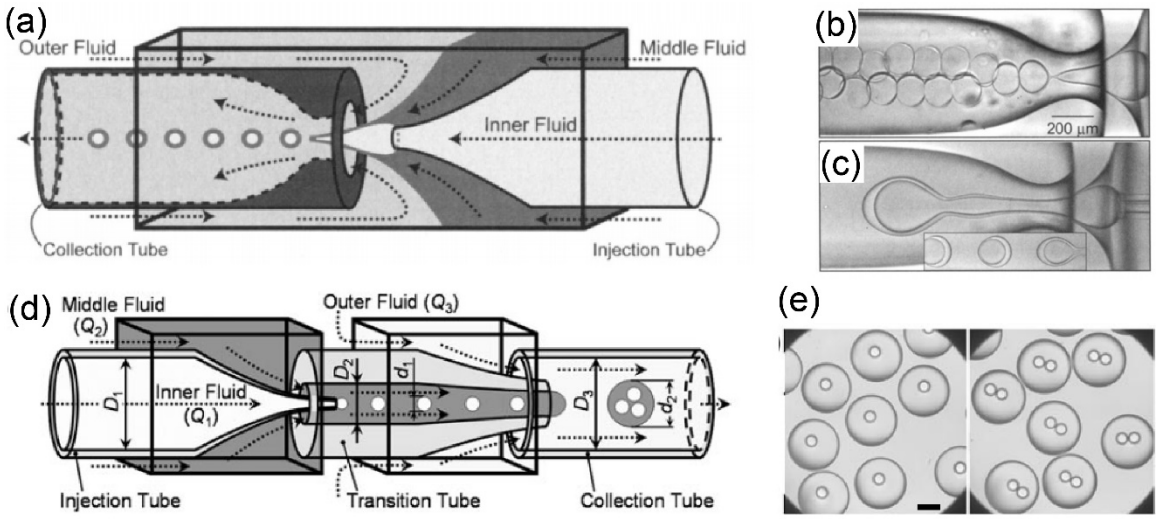

Figure 1.9 Co-axial microcapillary devices for microfluidic double emulsification. (a-c) One-step double emulsification in dripping and jetting regimes [27]. (d,e) Two-step double emulsification in coaxially assembled capillaries [28]. Scale bar: 200 μm.

Chu et al. reported the two-step formation of W/O/W double emulsion by using the sequential assembly of glass capillary microfluidic devices [28]. The device consisted of three modules including one injection tube, one transition tube, and one collection tube, thus producing droplets with their sizes and number of inner drops that could be adjusted

flexibility (Fig. 1.9d,e). Both inner drops and out drops had narrow size distributions with CVs below 3%.

(b) Janus droplets

In 2006, Nisisako et al. reported the formation of Janus droplets using a microfluidic flow-focusing geometry on a planer glass chip [29]. The device consisted of a Y-shaped channel for introducing two disperse phases to form a parallel stream upstream, then the parallel stream was sheared into biphasic droplets by a co-flowing aqueous phase at the junction (Fig. 1.10a). it was clear that the droplets had an obvious boundary separated two disperse phases, forming the O/W Janus droplets with a narrow size distribution of CV below 2%.

Kim et al. reported the formation of O/W Janus droplets using the glass capillary microfluidic device [30]. The device consisted of two inner capillaries and an outer capillary (Fig. 1.10b). Using such a device, the outer aqueous phase forced the two monomers to form O/W Janus droplets with two segments partially exposed to the external phase around the tips of the paired capillaries.

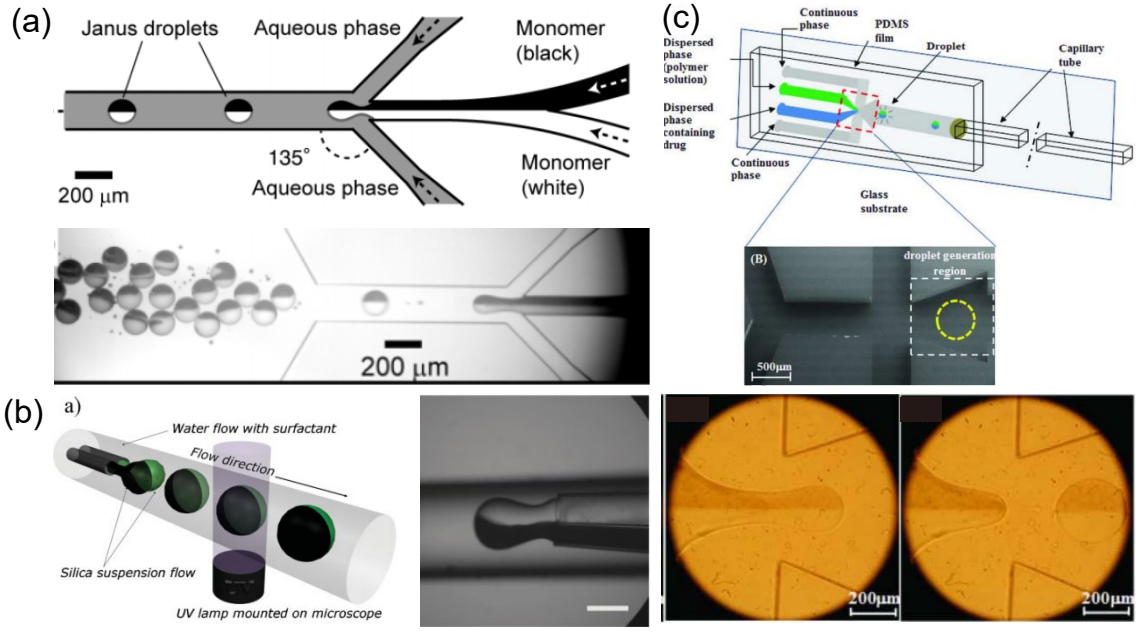

Figure 1.10 Janus droplet formation using different microfluidic devices. (a-c) Scheme and optical image of Janus droplets generated (a) in a microfluidic flow-focusing device [29];

(b) in a paired injection capillaries of a co-flowing microfluidic device [30]; (c) in a surface modified PDMS microchannels [31].

Sundararajan et al. designed the PDMS microchannels for the formation of Janus droplets via soft lithography technology [31]. Before entering the flow focusing region, two disperse phases formed a parallel stream. Near the flow-focusing junction, the parallel stream was sheared by the aqueous phase, forming O/W Janus droplets (Fig. 1.10c). The droplets were uniform in size with CVs below 5%. To generate O/W Janus droplets in PDMS microchannels, the wettability of the channel was modified to hydrophilic via multilayer poly(vinyl alcohol)-adsorbed coating method [32].

The abovementioned studies suggest that the interfacial property between the fluidic phases and the microchannel wall should be considered when producing biphasic droplets. The types of microfluidic device materials with different surface wettability suitable for generating core-shell and Janus droplets are summarized in Table 1.2.

Table 1.2 Microfluidic device materials, surface wettability, and applications

Application	Material	Surface wettability	Ref.
W/O/W double emulsion	Glass	Hydrophilic/localized hydrophobic surface modification	[24]
	Glass	Hydrophilic	[25] [26]
O/W/O double emulsion	PDMS	Hydrophobic/localized hydrophilic surface modification	[27] [28]
O/W Janus droplets	Glass	Hydrophilic	[29] [30]
	PDMS	Hydrophilic surface modification	[32]

The surface of glass-based microfluidic devices are natively hydrophilic, and having the following advantages:

(1) High strength.

(2) High rigidity.

(3) High chemical stability.

Meanwhile, the PDMS-based microfluidic devices are natively hydrophobic with the following merits:

(1) Ease of fabrication.

(2) Low cost.

(3) Nontoxicity.

To systemically discuss the interface property between the fluidic phase and the microchannel wall, we will investigate the possibility of generating biphasic droplets using both glass-based and PDMS-based microfluidic devices in this thesis.

1.2.3 Phase separation via mass transfer

Microfluidic generation of single-phase droplets and subsequent phase separation via mass transfer across the interface between the droplet/carrier phases have been utilized to design complex droplets like core-shell and Janus droplets precisely.

(a) Core-shell droplets

Choi et al. reported the formation of W/W/O double emulsions in a single step with precise control over the size from a single emulsion [33]. First, the single emulsion droplets were produced in PDMS microchannels (Fig. 1.11a,b). Immediately following their formation, the dispersed droplets, which are composed of the monomer and D-solvent, appear as a single phase. The SA molecules, which are dissolved in the continuous phase, can diffuse through the interface between the continuous and disperse phases. Finally, double emulsions with controlled morphology could be generated by changing the concentration of the disperse phase.

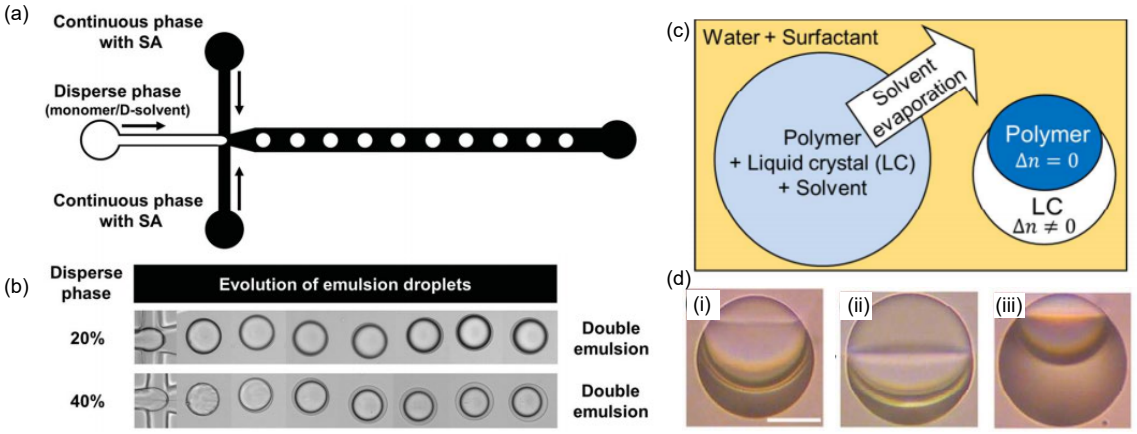

Figure 1.11 Formation of core-shell droplets and Janus droplets based on phase separation [33-34]. (a) Scheme of core-shell droplets formation. (b) Optical image of core-shell droplets generated at different concentrations of PEGDA in the disperse phase. (c) Schematic diagram of phase separation-induced Janus droplet formation from a single droplet. (d) Janus droplets with different shapes by adjusting the volume ratios of two disperse phases at (i) 1:1, (ii) 3:1, and (iii) 1:3. Scale bar: 20 μm.

(b) Janus droplets

Jeong et al. described the Janus droplets prepared from the phase separation of O/W droplets, which were generated in a glass capillary microfluidic device [34]. Once the O/W droplets were generated, the evaporation of the chloroform in the droplet caused the subsequent phase separation, thus forming the Janus droplets with two phase-separated segments. The shape of Janus droplets could be controlled with different volume ratios of two disperse phases (Fig. 1.11c,d).

1.2.4 Minimization of interfacial energies of biphasic droplets

Torza and Mason studied the interaction of two immiscible drops dispersed in a third immiscible phase by shear motion [35]. When a small biphasic droplet comprising of two immiscible phases dispersed in another external phase, the body forces exerting on the droplet can be neglected compared to the surface force, and the geometry of biphasic compound droplets at equilibrium is determined by the minimization of the interfacial energies at three liquid-liquid interfaces.

The relation between three interfacial energies can be described by the spreading parameters S_i, which is defined as:

$$S_i = \gamma_{jk} - (\gamma_{ij} + \gamma_{ki}) \qquad (1\text{-}1)$$

Where γ_{jk}, γ_{ij} and γ_{ki} are three interfacial tensions at the three interfaces ($i \neq j \neq k$ =1, 2, 3).

As shown in Figure 1.12, when the indices 1 and 3 for two phases of droplets are chosen to satisfy the $\gamma_{12} > \gamma_{23}$, the S_1 keeps negative and the biphasic droplets dispersed in the external phase can exhibit the following three morphologies at equilibrium:

(1) When $S_1 < 0$, $S_2 < 0$, $S_3 > 0$, core-shell droplets, where phase 1 is completed engulfed by phase 2.

(2) When $S_1 < 0$, $S_2 < 0$, $S_3 < 0$, Janus droplets, where phase 1 and phase 2 are partially engulfed.

(3) When $S_1 < 0$, $S_2 > 0$, $S_3 < 0$, two separate drops.

This principle offered us another approach to generate core-shell droplets and Janus droplets based on the minimization of interfacial energies.

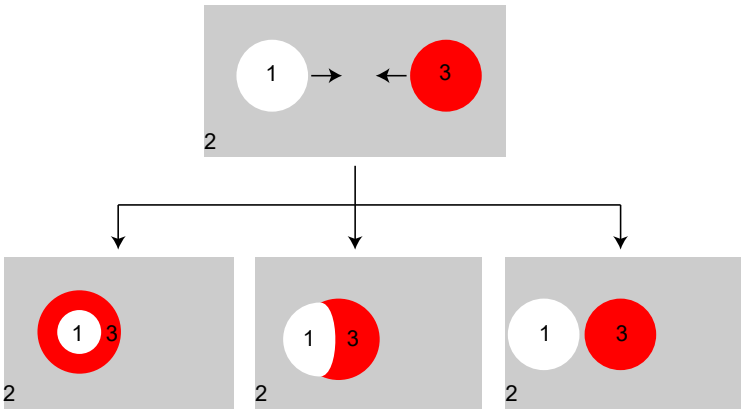

Figure 1.12 Relation between interfacial tensions and three morphologies at equilibrium

Pannacci et al. designed a PDMS microfluidic system having two flow-focusing junctions to generate biphasic droplets [36]. They confirmed that the variation of flow-rate ratios could change the size but not morphologies for a given droplet. Meanwhile, the morphologies were obtained due to minimizing the interfacial energy of the system. By adjusting the external phase, the interfacial tensions among the system were changed. Then, the variation of interfacial tensions appeared to minimize the interfacial energies of the system, causing the monodispersed droplets at equilibrium to change their morphologies from Janus state to core-shell droplets (Fig. 1.13a,b).

Nisisako et al. reported a microfluidic cross-flowing system on a glass chip for generating Janus droplets and core-shell droplets [37]. By using silicone oil or perfluorocarbon fluid as the non-curable phase, the biphasic droplets at equilibrium formed a Janus configuration or a core-shell configuration, respectively, consistent with minimizing the interfacial free energies among the three liquid phases. (Fig. 1.13c,d).

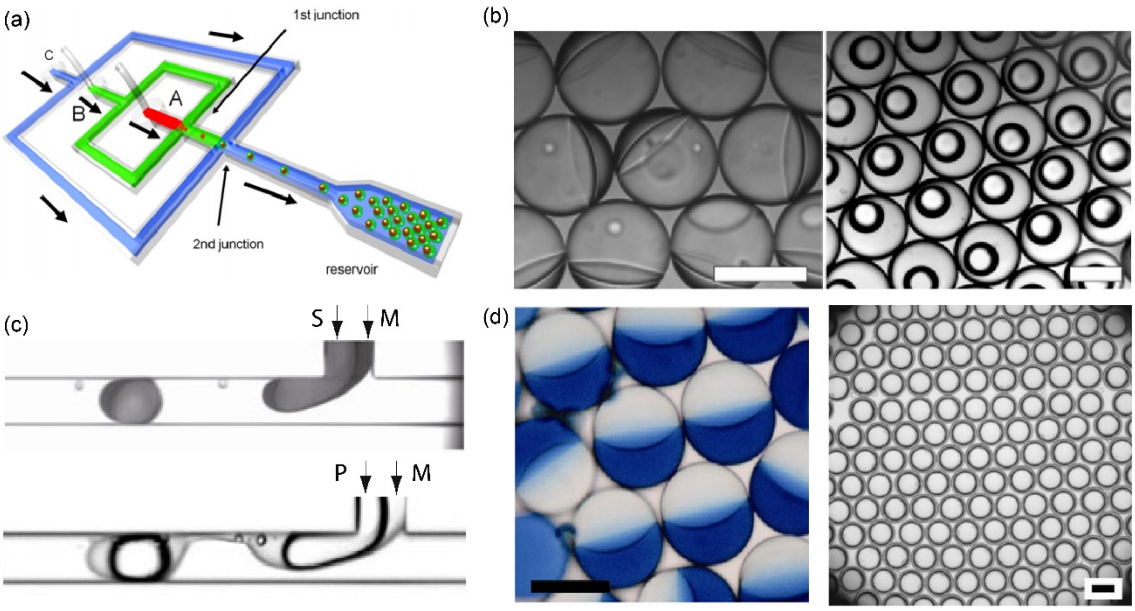

Figure 1.13 Microfluidic biphasic droplets produced via minimization of interfacial energies. (a) A device having two flow-focusing junctions; (b) Optical images of the produced Janus droplets of silicone oil and rapeseed oil dispersed in distilled water (left), and core-shell droplets of fluorinated oil and silicone oil dispersed in aqueous SDS solution (right) [36]. (c) One-step formation in a T-junction; (d) Optical images of the produced Janus droplets of acrylate monomer and silicone oil (left), and core-shell droplets of perfluorocarbon fluid (core) and acrylate monomer (shell) (right) [37]. Scale bars: 100 μm.

Compared to the phase separation via mass transfer, the formation of core-shell droplets and Janus droplets based on minimization of interfacial energies has the following advantages:

(1) Formation of droplets with extreme control over size.

(2) Morphologies of droplets can be controlled and estimated.

(3) Formation of droplets is not limited by the microfluidic device geometry.

(4) Convenient and time-saving

Considering the above analysis and advantages, in this study, we will focus on the formation of core-shell and Janus droplets based on the minimization of interfacial energies technique.

1.3 Microfluidic biphasic droplets and polymeric particles

To date, various polymeric microparticles have been synthesized from microfluidic biphasic droplets including core-shell and Janus droplets.

(a) Core-shell droplets

Core-shell droplets can be used as templates to fabricate microcapsules by solidifying the shell of the droplets. By using a capillary array injection microfluidic device, the formation of W/O/W double emulsions for fabricating microcapsules was reported by Shang et al. [38]. The core-shell droplets could be solidified by photo-induced polymerization because the shell of droplets was a photocurable ethoxylated trimethylolpropane triacrylate (ETPTA) phase (Fig. 1.14a-c). The sizes and shell thickness of the microcapsules emulsions could be controlled by adjusting the flow rates. Also, they demonstrated that the multicomponent microcapsules could also be obtained using the same microfluidic device to generate multi-component double emulsions by controlling types of inner phase.

Microfluidic formation of O/W/O double emulsions for fabricating photonic capsules with hydrogel shells, poly(ethylene glycol) diacrylate (PEGDA), was reported by Kim et al. [39]. First, monodisperse O/W/O double emulsion droplets were generated in a coaxial microcapillary device. Then, ultraviolet (UV) irradiation was used to fabricate microcapsules with CVs below 2% (Fig. 1.14d-f). The microcapsules displayed green color at room temperature, and a color variation from green to red as the temperature increased, thus proposing the application of injectable colorimetric micro-thermometers.

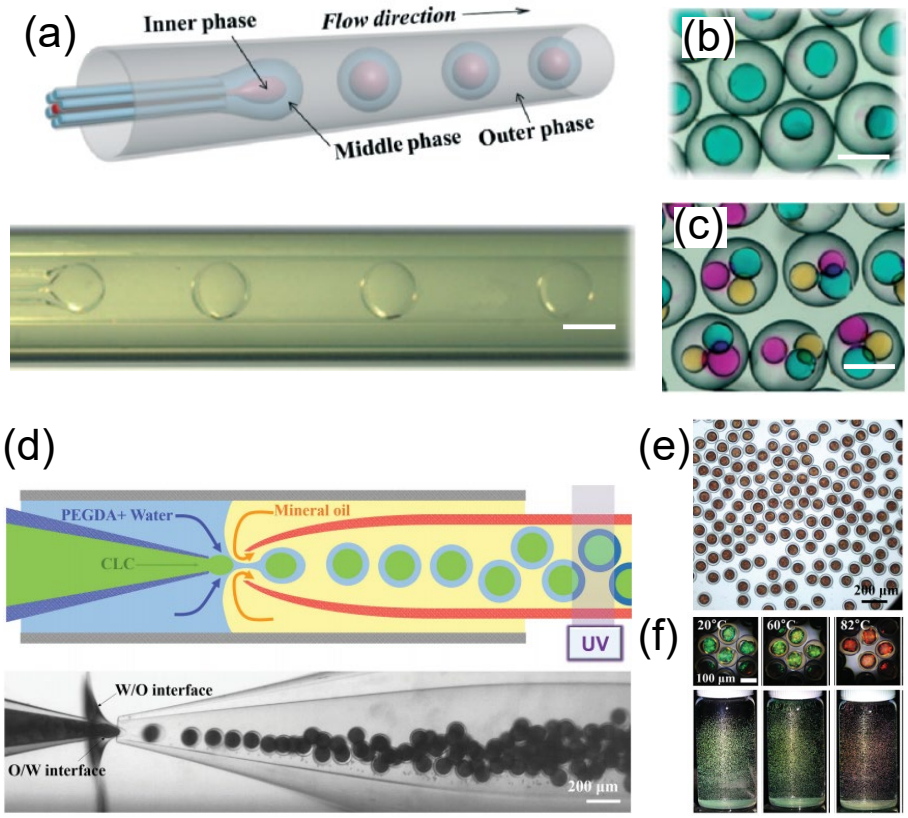

Figure 1.14 Microcapsules templated from double emulsions. (a) W/O/W double emulsion formation in a microcapillary device. (b,c) The produced single-core and three-core capsules [38]. Scale bars: 300 μm. (d) O/W/O double emulsion formation in a microcapillary device. (e,f) The prepared microcapsules and their temperature-responsive structural colors.

(b) Janus droplets

Janus droplet is an ideal template for fabricating anisotropic particles or non-spherical particles. By using a microfluidic flow-focusing device on a glass chip, the formation of Janus particles having electrical and color anisotropies was first reported by Nisisako et al. [29]. First, monodispersed Janus droplets having black (carbon black) and white (titanium oxide) hemispheres were generated. Subsequently, the two-color Janus particles were fabricated via thermal-induced polymerization (Fig. 1.15a-d). Because the carbon black and titanium oxide had different charging properties, the prepared particles were responsive to electric fields.

Meanwhile, non-spherical particles can be fabricated from Janus droplets. For example, Kim et al. reported the microfluidic formation of Janus droplets, comprising curable monomer segment and non-curable oil segment, for fabricating crescent-moon-shaped polymer microparticles (Fig. 1.15e,f) [40]. The shape of particles could be varied by changing the flow-rate ratios of the curable and non-curable segments. Also, the hydrophilic/hydrophobic property of the particles could be controlled via adding hydrophilic silica nanoparticles in the monomer segments, suitable as stabilizers for oil droplets in water.

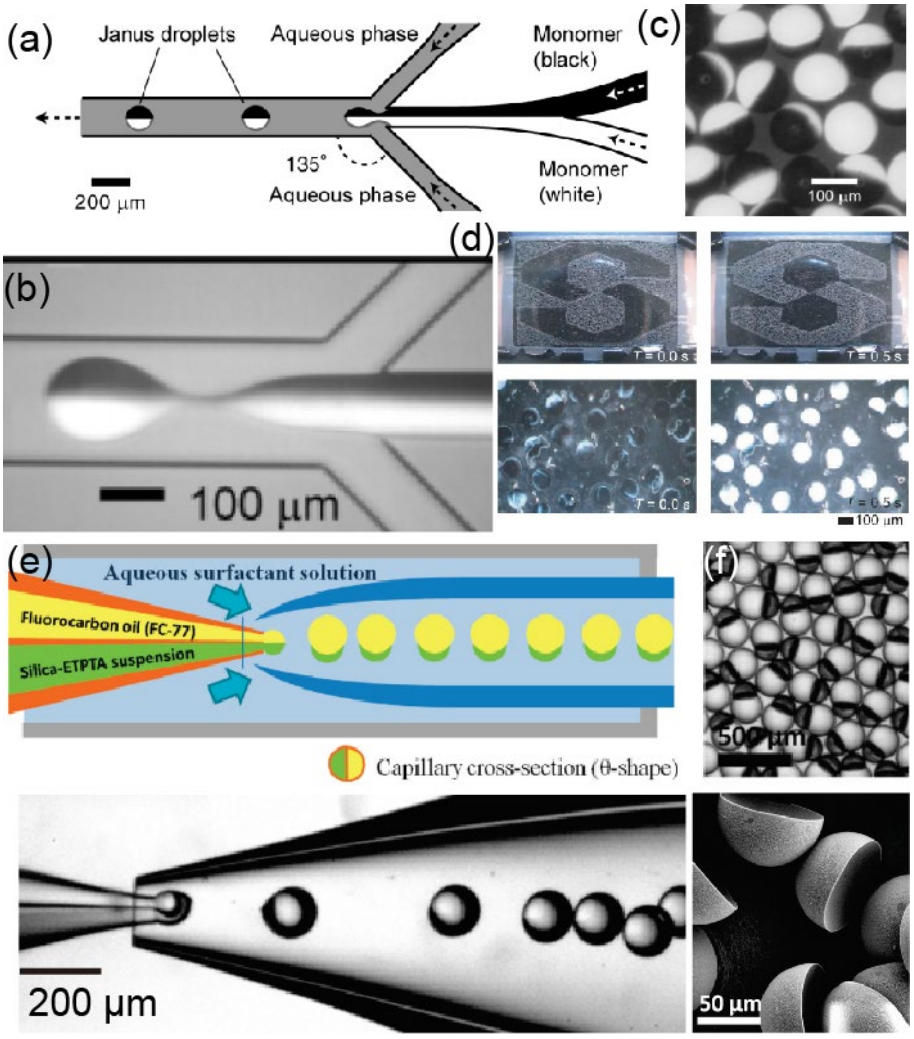

Figure 1.15 Microparticles synthesized from Janus droplets [29, 40]. (a-d) Preparation of Janus particles with electrical and color anisotropy for particles-based display application. (e-f) Preparation of crescent-moon-shaped particles from Janus droplets..

In this thesis, we will focus on the application of biphasic droplets in the field of fabricating microparticles with desired shapes, including microcapsules and anisotropic particles.

1.4 Objectives

The main objectives of this thesis are as follows:

(a) To investigate the new microfluidic approach for generating biphasic core-shell and Janus droplets by considering the minimization of the interfacial energies and surface wettability of microchannels.

(b) To investigate the application of produced biphasic droplets.

(c) To achieve high-throughput production of droplets for industrial production

To achieve objective (a), we focused on the following aspects:

(1) Fabrication of glass-based and PDMS-based devices for generating biphasic droplets.

(2) Observation of droplet formation in microfluidic devices.

(3) Characterization of generated droplets.

(4) Investigation of the hydrodynamic effects on droplet sizes and formation regime.

To achieve objective (b), we focused on the following aspects:

(1) Microfluidic synthesis of polymer microcapsules with tunable shell thickness from core-shell droplets.

(2) Microfluidic synthesis of polymer lens-shaped with controlled morphology from Janus droplets.

To achieve objective (c), we focused on the following aspects:

(1) Design and fabrication of a microfluidic device for generating droplets in parallel.

(2) Generation frequency evaluation of core-shell and Janus droplets.

(3) Evaluation of droplet sizes and shapes.

1.5 Outline of thesis

In Chapter 1, the background of emulsions and their preparation methods were introduced. Then the droplet-based microfluidic technology for generating biphasic droplets and their application was introduced. Finally, the importance of interfacial energy at the interfaces among the involved fluids and channel surfaces on the production of biphasic droplets was emphasized, which pointed out the research objective of this thesis.

In Chapter 2, the Janus to core-shell transition of microfluidic biphasic generated in a microfluidic flow-focusing device is reported for the fabrication of microcapsules with controlled shell thickness.

In Chapter 3, a study on microfluidic surfactant-laden Janus droplets with controlled morphology and enhanced stability is reported for the fabrication of microlens-shaped particles.

In Chapter 4, the formation of microfluidic ternary emulsion droplets with new co-existing components is reported to discuss the scalable fabrication of biconvex polymer particles.

In Chapter 5, one-step formation of W/O/W double emulsions in PDMS microfluidic devices is reported.

In Chapter 6, a new parallelizion device for increasing the production throughput of biphasic droplets is reported.

In Chapter 7, the results and academic achievements, which are conducted based on the objectives stated in Chapter 1, are summarized. Future outlook is also presented.

The relations between each chapter and the process chart of the study are shown in Figure 1.17.

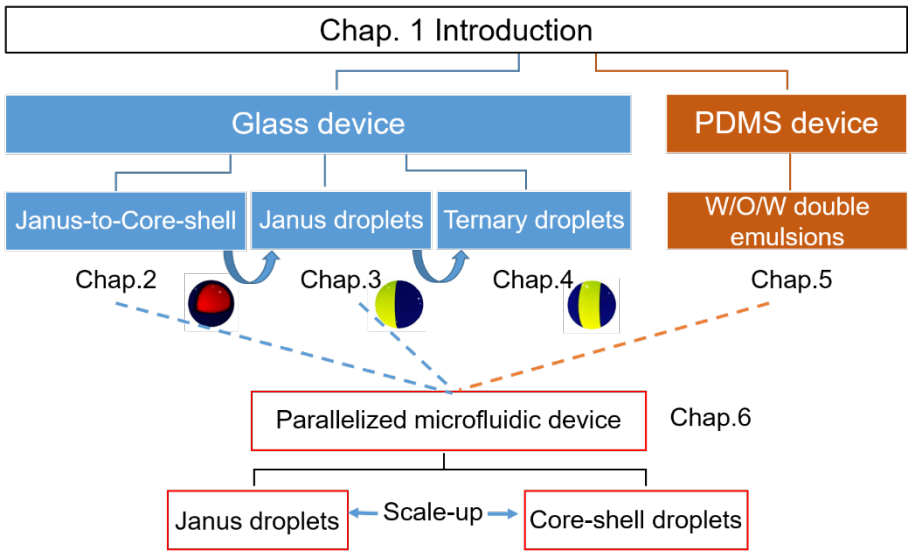

Figure 1.17 The relations between each chapter and the process chart of the study

1.6 References

[1] Adams, L.; Kodger, T. E.; Kim, S. H.; Shum, H. C.; Franke, T.; Weitz, D. A. *Soft Matter* 8, 10719 (2012).

[2] Matsumoto, S; Kang, W.W. *J. Disp. Sci. Tech.* 10, 455 (1989).

[3] Hasinovic, H.; Friberg, S. E. *Langmuir* 27, 11 (2011).

[4] Ge, L.; Jin, H.; Li, X.; Wei, D. Guo, R. *Langmuir* 35, 3490 (2019).

[5] Muschiolik, G. *Curr. Opin. Colloid Interface Sci*. 12, 213 (2007).

[6] Davis, S. S.; Walker, I. M. *Methods Enzymol.* 149, 51 (1987).

[7] Hwang, S.; Nam, J. O.; B. J. Lee, S. W. H. C. S. Lee, *Korean Soc. Biotechnol. Bioeng. J.* 27, 07 (2012).

[8] Chen, C. H.; Abate, A. R.; Lee, D. Y.; Terentjev, E. M.; D. A. Weitz, *Adv. Mater.* 21, 3201 (2009).

[9] Chakravarti, A. K.; Chowdhury, S. B.; Mukherjee, D. C. *Colloids Surf. A* 166, 7 (2000).

[10] Goubault, C.; Pays, K.; Olea, D.; Gorria, P.; Bibette, J.; Schmitt, V.; Leal-Calderon, F. *Langmuir* 17, 5184 (2001).

[11] Hasinovic, H.; Friberg, S. E.; Rong, G. *J. Colloid Interface Sci.* 354, 424 (2011).

[12] Joscelyne, S. M.; Trägårdh, G. *J. Membr. Sci.* 169, 107 (2000).

[13] Mine, Y.; Shimizu, M.; Nakashima, T. *Colloids Surf. B* 6, 261 (1996).

[14] Sugiura, S.; Nakajima, M.; Yamamoto, K.; Iwamoto, S.; Oda, T.; Satake, M.; Seki, M. *J. Colloid Interface Sci.* 270, 221 (2004).

[15] Whitesides, G. M. *Nature* 442, 368 (2006).

[16] Mark, D.; Haeberle, S.; Roth, G.; von Stetten, F.; Zengerle, R. *Chem. Soc. Rev.* 39, 1153 (2010).

[17] Sackmann, E. K.; Fulton, A. L.; Beebe, D. J. *Nature* 507, 181 (2014).

[18] Thorsen, T.; Roberts, R. W.; Arnold, F. H.; Quake, S. R. *Phys. Rev. Lett.* 86, 4163 (2001).

[19] Nisisako, T.; Torii, T.; Higuchi, T. *Lab chip* 2, 24 (2002).

[20] Anna, S. L.; Bontoux, N.; Stone, H. A. *Appl. Phys. Lett.* 82, 364 (2003).

[21] Cramer, C.; Fischer, P. Windhab, E. J. *Chem. Eng. Sci.* 59, 3045 (2004).

[22] Shah, R. K.; Shum, H. C.; Rowat, A. C.; Lee, D.; Agresti, J. J.; Utada, A. S.; Chu, L.Y.; Kim, J. W.; Fernandez-Nieves, A.; Martinez, C. J.; Weitz, D. A. *Mater. Today* 11, 18 (2008).

[23] Choi, C. H.; Kim, J.; Nam, J. O.; Kang, S. M. Jeong, S. G. Lee, C. S. *ChemPhysChem*. 15, 21 (2014).

[24] Okushima, S.; Nisisako, T; Torii, T.; Higuchi, T. *Langmuir* 20, 9905 (2004).

[25] Hwang, S.; Choi, C. H.; Lee, C. S. *Macro. Res.* 20, 422 (2012).

[26] Abate, A. R.; Thiele, J. Weinhart, M. Weitz, D. A. *Lab Chip* 10, 1774 (2010).

[27] Utada, A. S.; Lorenceau, E.; Link, D. R.; Kaplan, P. D.; Stone, H. A.; Weitz, D. A. *Science* 308, 537 (2005).

[28] Chu, L. Y.; Utada, A. S.; Shah, R. K.; Kim, J. W.; Weitz, D. A. *Angew. Chem. Int. Ed.* 119, 128 (2007).

[29] Nisisako, T.; Torii, T.; Takahashi, T.; Takizawa, Y. *Adv. Mater.* 18, 1152 (2006).

[30] Kim, S. H.; Jeon, S. J.; Jeong, W. C.; Park, H. S.; Yang, S. M. *Adv. Mater.* 20, 4129 (2008).

[31] Sundararajan, P.; Wang, J. Rosen, L. A.; Procopio, A.; Rosenberg, K. *Chem. Eng. Sci.* 178, 199 (2018).

[32] Wu, D. P.; Luo, Y.; Zhou, X. M.; Dai, Z. P.; Lin, B. C. *Electrophoresis* 26, 211 (2005).

[33] Choi, C. H.; Weitz, D. A.; Lee, C. S. *Adv. Mater.* 25, 2536 (2013).

[34] Jeong, J.; Gross, A.; Wei, W. S.; Tu, F.; Lee, D.; Collings, P. J.; Yodh, A. G. *Soft Matter* 11, 6747 (2015).

[35] Torza, S.; Mason, S. G. *Science* 163, 813 (1969).

[36] Pannacci, N.; Bruus, H.; Bartolo, D.; Etchart, I.; Lockhart, T.; Hennequin, Y.; Willaime, H.; Tabeling, P. *Phys. Rev. Lett.* 101, 164502 (2008).

[37] Nisisako, T.; Torii, T. *Microfluid Nanofluid.* 9, 427–437(2010)

[38] Shang, L.; Cheng, Y.; Wang, J.; Ding, H.; Rong, F.; Zhao, Y.; Gu, Z. *Lab Chip*, 14, 3489 (2014).

[39] Lee, S. S.; Kim, B. S.; Kim, K. Won, J. C.; Kim, Y. H. Kim, S. H. *Adv. Mater.* 27, 627 (2014).

[40] Kim, S. H.; Alireza, A.; Weitz, D. A. *J. Am. Chem. Soc.* 133, 5516 (2011).

Chapter 2

Janus-to-core-shell transition of microfluidic biphasic droplets

2.1 Introduction

2.1.1 Microcapsules and their applications

Microcapsules have been extensively used in variety of fields, including foods [1,2], cosmetics [3,4], pharmaceutics [5], printing [6,7], and self-healing materials [8,9].

Conventional techniques for producing microcapsules include spray drying (Fig. 2.1), layer-by-layer deposition, interfacial polymerization, coacervation, and membrane emulsification [10–14]. However, it is still difficult to fabricate monodisperse microcapsules with controlled size and high encapsulation efficiency.

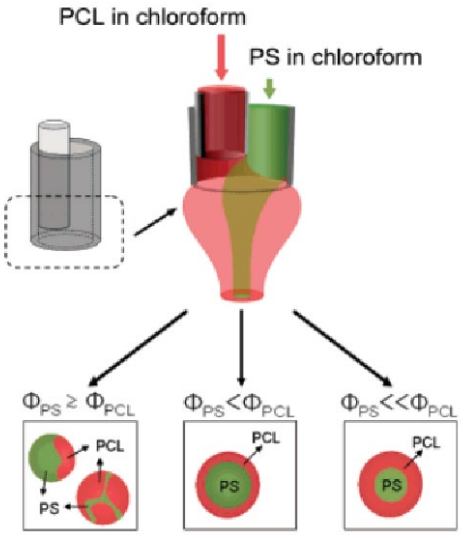

Figure 2.1 An example of the coaxial electrospraying for making core-shell particles [10].

2.1.2 Microfluidic approach for fabricating microcapsules

Droplet microfluidics has recently emerged as a new promising route for preparing microcapsules. Monodisperse core-shell droplets prepared by microfluidics function as excellent precursors for making microcapsules via subsequent various solidification methods, including free-radical polymerization [15,16], solvent evaporation [17], freezing [18], and ionic cross-linking [19].

To date, a two-step (Fig. 2.2) [15, 20–29] or one-step (Fig. 2.3) [30–38] methods have been chosen to make core-shell droplets as precursors. In the two-step method, a technical challenge is that the precise tuning of the flow rates is needed for accurate one-by-one encapsulation of the cores in the shells, causing the difficulty in the control of shell thickness. Meanwhile, in the one-step approach, although it is basically limited for single core droplets, the flow-rate ratio of the core and shell phase can be flexibly varied because both core and shell are produced via one instability. This allows us to tune the shell thickness flexibly compared with the core size, for example, to make the capsules having an ultra-thin shell.

Previously, Nisisako et al. reported the one-step formation of Janus droplets in a T-junction microfluidic device and their interfacial-energy driven evolution to core-shell droplets (Fig. 2.3g-h). The resultant core-shell precursors were photopolymerized to make oil-filled acrylate capsules with tunable shell thickness [31]. To the best of our knowledge, however, there has been no report on the Janus-to-core-shell transition of biphasic droplets in a microfluidic flow-focusing device. In addition, few studies have demonstrated thermal polymerization of microfluidic core-shell droplets to make polymeric microcapsules with ultra-thin shells, which we believe is a more suitable method for many industrial applications.

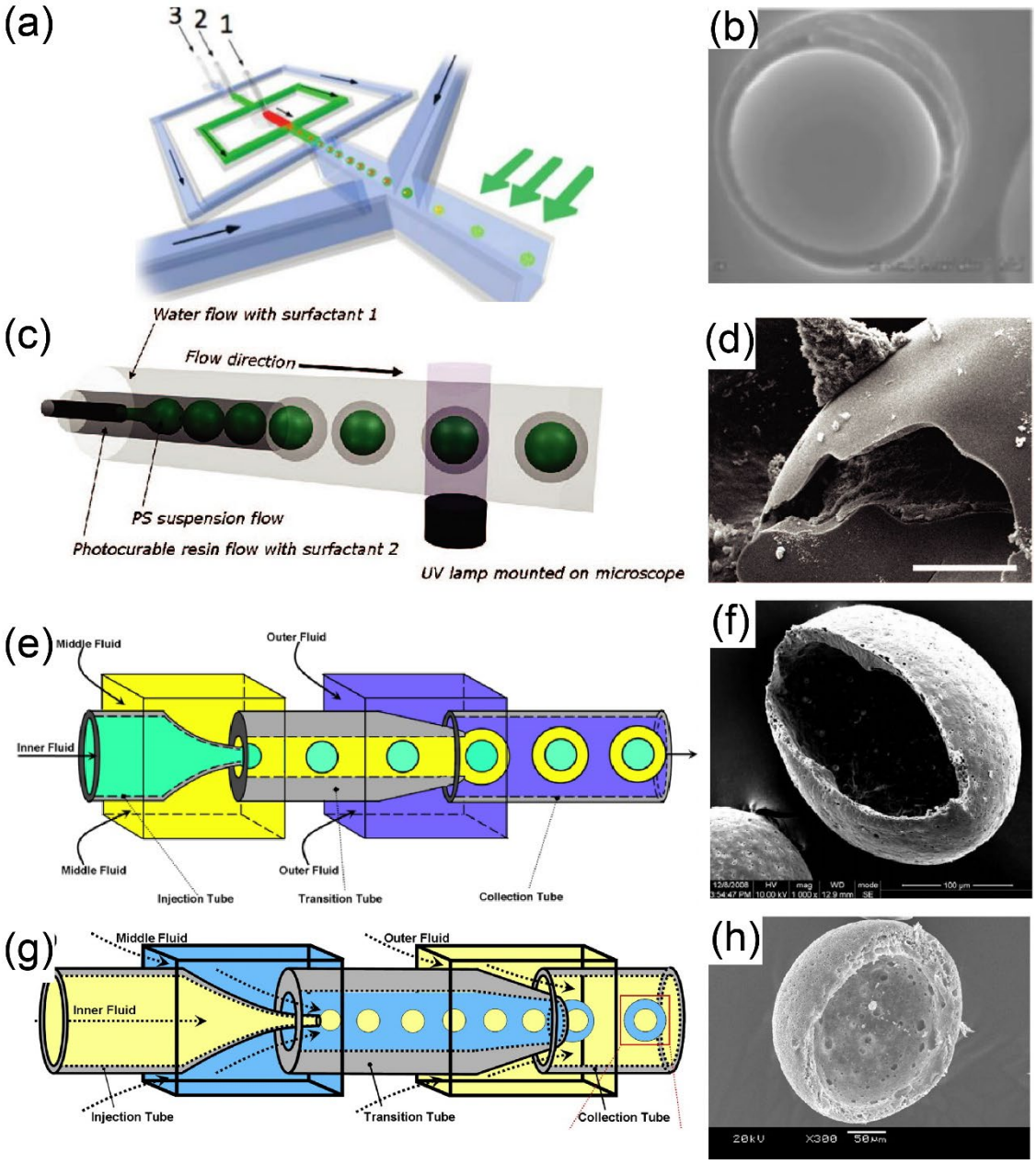

Figure 2.2 Schematic illustration of generating core-shell droplets in a two-step manner (left) and the fabricated microcapsules (right). (a-d) Microcapsules solidified via photo-induced polymerization [15,26]; (e-h) Microcapsules solidified via solvent evaporation [28,29].

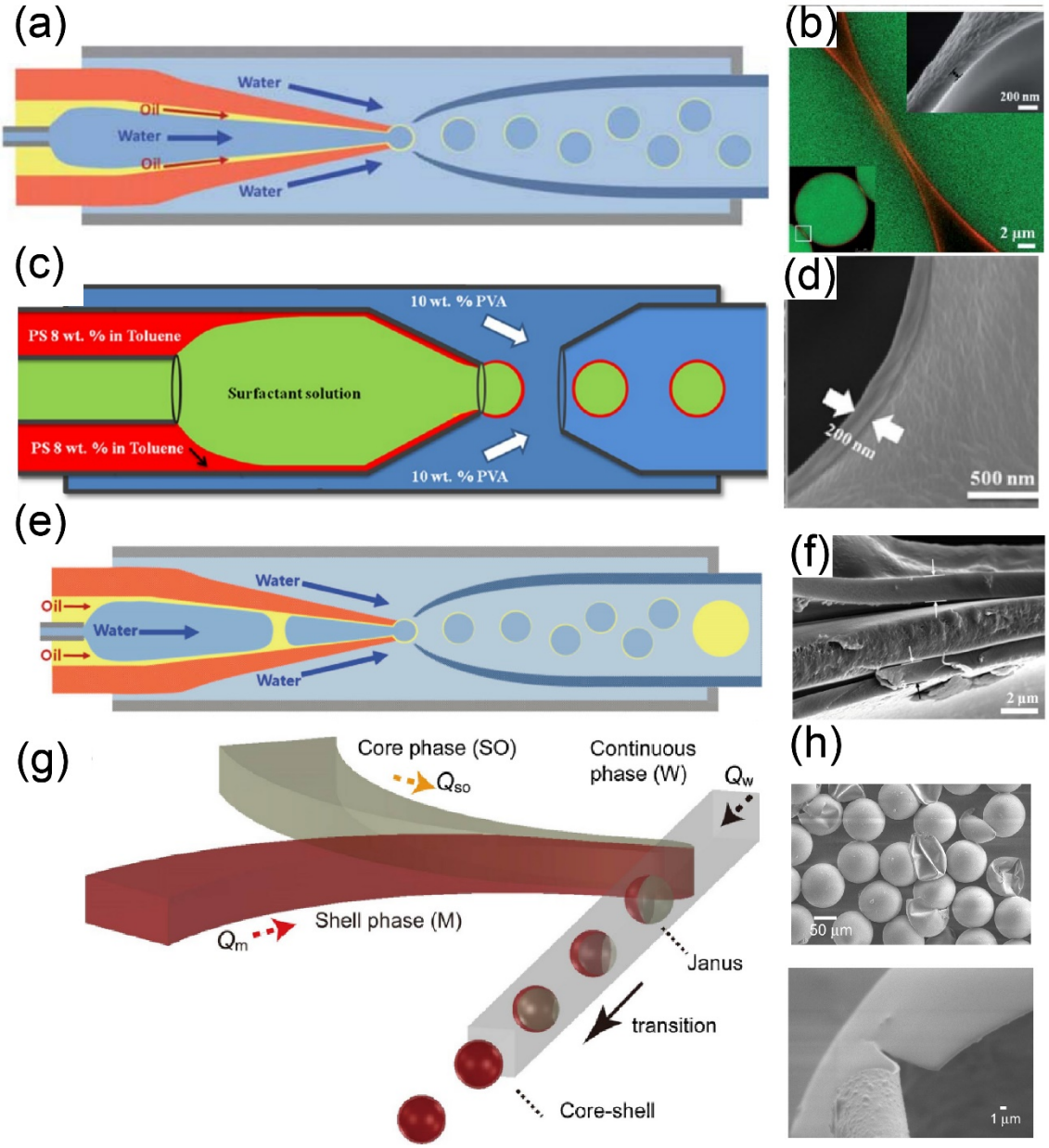

Figure 2.3 Schematic illustration of generating core-shell droplets at one-step manner (left) and the fabricated microcapsules with ultra-thin shell thickness (right). (a-d) Microcapsules solidified via solvent evaporation [36,37]; (e-h) Microcapsules solidified via photo-induced polymerization [31,38].

2.1.3 Objectives

Although the microfluidic one-step method for generating core-shell droplets showed its advantages in fabricating polymer microcapsules, few studies have demonstrated heat-induced polymerization of the polymeric microcapsules with ultra-thin shells. Also, the Janus-to-core-shell transition of biphasic droplets, to the best of our knowledge, symmetric flow-focusing geometry has never been used for demonstrating the formation of Janus droplets and their evolution to the core-shell form. Therefore, in this chapter, we present a novel microfluidic approach to synthesize polymeric microcapsules with tunable shell thickness and surface morphology by using a flow-focusing Janus droplet generator and off-chip photo- and thermally induced polymerization.

2.1.4 Outline

In the 2.1 section, the application and conventional fabrication methods of polymer microcapsules were introduced. Also, the advantages of droplet microfluidics technology for fabricating polymer microcapsules are introduced. Finally, the existing challenges in the current microfluidic fabrication of polymer microcapsules were described, which act as the objectives in this study.

In the 2.2 section, fabrication and assembly of the microfluidic device, materials used for droplet formation, and peripheral equipment for observation and characterization of the products are described.

In the 2.3 section, the experiment results and discussion in four parts including the formation of biphasic droplets (2.3.1), hydrodynamic effect on biphasic droplet formation (2.3.2), characterization of generated biphasic droplets (2.3.3), and fabrication of polymer microcapsules from core-shell droplets (2.3.4) are described.

In the 2.4 section, the results of this study are summarized.

2.2 Materials and experimental methods

2.2.1 Materials and peripheral equipment

Materials and peripheral equipment in this experiment are as follows:

Name	Company
1, 6-hexanediol diacrylate (HDDA)	Shin-Nakamura Kagaku, Wakayama, Japan
Silicone oil	Dow Corning Toray, Tokyo, Japan
Polyvinyl alcohol (PVA)	Mitsubishi Chemical Corporation, Tokyo, Japan
2-Hydroxy-2-methylpropiophenone (Darocur 1173)	Ciba Japan K. K., Japan
2,2'-Azobis(2,4-dimethylvaleronitrile) (V-65)	Fujifilm Wako Pure Chemical Corporation, Osaka, Japan
Oil-soluble dye (Oil Red O)	Sigma-Aldrich, MO, USA
Deionized water	Merck Direct-Q UV, Tokyo, Japan
Acetone	Fujifilm Wako Pure Chemical Corporation, Osaka, Japan
Ethanol	Fujifilm Wako Pure Chemical Corporation, Osaka, Japan
Glass syringes (1000 series)	Hamilton Company, NV, USA
Syringe pumps (KDS200)	KD Scientific, MA, USA
Slide glass (S111)	Matsunami Glass Industry, Tokyo, Japan
Optical microscope (BX-51)	Olympus, Tokyo, Japan
High-speed video camera (Fastcam Mini AX50)	Photron, Tokyo, Japan
Scanning electron microscope (SEM, JSM-6610LA)	JEOL, Tokyo, Japan
Ultra-violet (UV) light source (LA-410UV)	Hayashi-repic, Tokyo, Japan
Software ImageJ	National Institute of Health, NY, USA
Surface Tensiometer (B100)	Asumi Giken, Tokyo, Japan
Ceramic hot stirrer (CHPS-170DN)	AS ONE Corporation, Tokyo, Japan
Nylon mesh sheet (42 μm × 42 μm)	Tokyo Screen, Tokyo, Japan

2.2.2 Device fabrication and assembly

A microfluidic Janus droplet generator with a rectangular cross-section was prepared on a glass chip (15 mm × 15 mm × 3.5 mm) using dry etching [39, 40]. The Y-shaped channel for infusing two disperse phases (an acrylate monomer and silicone oil) and the two co-flowing channels for infusing continuous phase (aqueous PVA solution) has a depth

of 100 μm and a width of 100 μm around the sheath-focusing junction. The drainage channel has a depth of 200 μm and a width of 200 μm. This deeper region was made by fusion bonding of two separate chips each with microfabricated grooves (depth 100 μm) with precise alignment (Fig. 2.4).

The prepared glass chip was assembled with a stainless-steel holder (36 mm × 36 mm × 10 mm), which is linked to the poly(tetrafluoroethylene) (PTFE) tubes (0.8 mm internal diameter, 1.5 mm outer diameter) for the transportation of fluids (For details, see Appendix A.1).

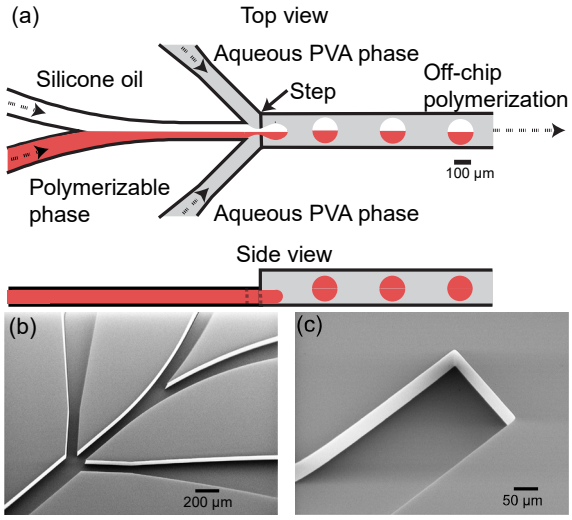

Figure 2.4 A microfluidic flow-focusing Janus droplet generator. (a) Schematic illustration of the geometry; (b-c) SEM images of (b) the flow-focusing region and (c) the deeper drainage channel fabricated on two separate glass chips.

2.2.3 Chemicals

We chose 1,6-hexanediol diacrylate (HDDA, dynamic viscosity η_m = 6.35 mPa s, density ρ_m = 1.02 g cm^{-3}) as a curable droplet phase, and silicone oils of 10, 20, 50, and 100 cSt (SH200-10, 20, 50, 100CS) as a non-curable droplet phase. Unless otherwise specified, the viscosity of silicone oil is 10 cSt. An aqueous 2.0 wt.% polyvinyl alcohol (PVA, GL-03, M_w ~ 20,000 g mol^{-1}, 87-89% hydrolyzed) solution was used as the aqueous phase. For subsequent polymerization, a photoinitiator (Darocur 1173) was added in HDDA to generate a mixture with a concentration of 2.0–10.0 wt.% or a thermal initiator

(V-65) to generate a mixture with the concentration of 2.0–15.0.wt %. An oil-soluble dye (Oil red O) was dissolved in HDDA to differentiate the two organic phases visually.

2.2.4 Formation and characterization of droplets

Liquids were filled in glass syringes and supplied to the microfluidic device using syringe pumps. An optical microscope equipped with a high-speed video camera was used for the observation of droplets generation. Software ImageJ was used to measure the diameters of droplets

2.2.5 Preparation and characterization of polymer microcapsules

The biphasic droplets were solidified via off-chip photo- or thermally induced polymerization. For photo polymerization, the generated droplets were collected in a beaker and continuously exposed to an ultra-violet (UV) light from a light source. The distance for irradiation from the UV light source was about 15–20 cm. For thermal polymerization, the generated droplets were directly guided into a disposable cup containing the aqueous PVA solution via the drainage tube. The disposable cup was placed in a beaker containing pure water heated to 80–85 °C, monitored by a thermometer using a ceramic hot stirrer.

Smaller particles made from satellite droplets were removed by filtration using a nylon mesh sheet (grid size: 42 μm × 42 μm). Then, the microcapsules remaining on the mesh sheet were lightly washed by acetone and ethanol. A scanning electron microscope was used to observe the surface and structure of the microcapsules. For the preparation of the cross-sections of the microcapsules, we dispersed the particles randomly in an epoxy resin and sliced the solidified resin manually using a razor blade.

2.3 Results and discussion

2.3.1 Formation of biphasic droplets

2.3.1.1 Biphasic droplets formed in a microfluidic flow-focusing device

Biphasic droplets of similar sizes were generated one-by-one when the flow rates of

the disperse and continuous phases were controlled within the low Capillary number and Reynolds number regions. The formation of biphasic droplets in the dripping regime, when the flow rates of HDDA (Q_m), silicone oil (Q_s), and PVA solution (Q_c) stream were 0.5 mL h^{-1}, 0.5 mL h^{-1}, and 12.0 mL h^{-1}, respectively, is shown in Fig. 2.5a. Under this flow condition at Q_m: Q_s = 1:1, it was difficult to confirm whether the silicone oil segment was partially engulfed or fully encapsulated within the HDDA part. In contrast, when the flow-rate ratio was set at Q_m: Q_s = 1:9 (Fig. 2.5b), partially exposed HDDA and silicone oil segments could be clearly observed. Biphasic droplets with different volume ratios could be generated at various Q_m/Q_s ratios (Fig. 2.5c). Thus, the Janus geometry of the biphasic droplets immediately following their break-off could be confirmed visually. We could also observe that the Janus droplets after break-off kept their morphology with the silicone oil part gradually engulfed by the HDDA segment, flowing downstream to the outlet.

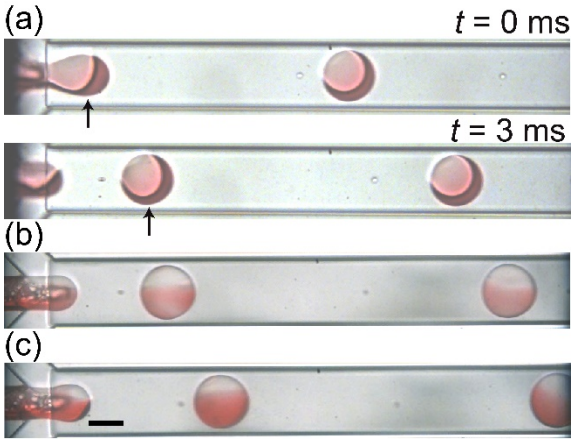

Figure 2.5 Formation of Janus droplets at different flow-rate ratios of the acrylate monomer (Q_m) and silicone oil (Q_s). (a) Break-off of a biphasic droplet (shown with arrows) at Q_m: Q_s = 1:1; (b) Q_m: Q_s = 1:9; (c) 1:4. The total flow rate of two organic phases ($Q_{d,\,total} = Q_m + Q_s$) is 1.0 mL h^{-1}, and the flow rate of the aqueous PVA phase (Q_c) is 6.0 mL h^{-1} × 2. Scale bar: 100 μm.

Because the two droplet phases (i.e., HDDA and silicone oil) in this study were mutually immiscible, the diffusive mixing across the two Janus lobes should not occur [40]. However, we observed the phenomenon of color spreading from HDDA to the silicone oil

segment when the HDDA containing oil-soluble dye was used. We consider the color spreading phenomenon was because of the HDDA forming a layer on the silicone oil segment.

2.3.1.2 Comparison of biphasic droplets generated in flow-focusing and T-shape microfluidic devices

Table 2.1 Dimensions of T-shaped and flow-focusing microfluidic devices

Microfluidic device	Height of inlet (μm)	Width of the inlet (μm)	Height of drainage channel (μm)	Width of drainage channel (μm)
T-shaped [31]	100	100	100	200
Flow-focusing	100	100	200	200

In this study, we confirmed that symmetric flow-focusing geometry was also feasible to generate Janus droplets comprised of the same two immiscible phases. Meanwhile, a previous study also reported the generation of Janus droplets and their morphological transition using the asymmetric T-junction [31]. The dimensions of the two microfluidic devices are shown in Table 2.1.

The similarity between the two studies indicates that the structural difference in microfluidic droplet generators would not affect the final morphology of the biphasic droplets. It is also suggesting that the interfacial energy, rather than the hydrodynamic effects, is playing a crucial role in the phase separation within the droplets. Meanwhile, a flow-focusing geometry offers more stable droplet generation in the dripping regime than a T-junction. This is because the disperse phase in a flow-focusing geometry is surrounded by two symmetric continuous-phase streams and does not wet the sidewalls [41, 42], while the disperse phase at a T-junction stays in contact with one of the sidewalls and eventually wets the sidewall to affect the formation of droplets [43].

2.3.2 Hydrodynamic effect on biphasic droplet formation

In this section, we mainly discussed the influence of flow conditions such as flow rates on the formation regime, generation frequency, and size of droplets. Also, the effect

of adjusting the variation of the silicone oil phase and channel size on the above parameters was demonstrated.

2.3.2.1 Formation regime of biphasic droplets

It is known that droplet formation is the result of fluid interfacial instabilities [44]. Generally, there are four distinct regimes of biphasic droplet formation in microfluidics, including unstable flow, dripping, elongated and jetting regime. In the unstable flow regime, droplets will be generated before the junction. In the dripping regime, the two dispersed phases entering the junction are immediately sheared into uniform droplets by the shear rupturing mechanism. In the jetting regime, polydisperse droplets are generated in an irregular and unstable manner. In the elongated regime, a laminar flow forms downstream and eventually generates a plug-shaped droplet in squeezing regime.

The capillary number for the continuous phase *Ca* is used to predict a dominant mechanism of droplet formation, which is defined as:

$$Ca = \frac{\eta v}{\gamma} \tag{2-1}$$

where η = 1.95 mPa s is the dynamic viscosity of the aqueous PVA solution, v is the mean velocity of the aqueous PVA stream, and γ = 5.95 mN m^{-1} is the average interfacial tension of HDDA/PVA interface and silicone oil/PVA interface.

Figure 2.6 is the flow pattern diagram to understand the condition for the formation of biphasic droplets in this study. The flow diagram has an enclosed mountain-shape [39] with the capillary number (*Ca*) ranging from 10^{-3} to 10^{-1}. The maximum $Q_{d,\,total}$ for generating monodisperse biphasic droplets was ~5.5 ml/h with Q_c ranging from 0.2 ml/h to 30 ml/h. When $Q_{d,\,total}$ was below 0.1 ml/h, the two immiscible parallel organic phases became unstable, and silicone oil droplets were generated in the HDDA phase before the junction. When $Q_{d,\,total}$ was in the range from 0.1 to 5.5 ml/h, the two immiscible parallel organic phases formed a stable laminar flow when Q_c was too low, while the disordered formation of droplets in the jetting regime was observed when Q_c was too high. From such a diagram, we understood that droplets of uniform size could form when we properly set Q_c and $Q_{d,\,total}$.

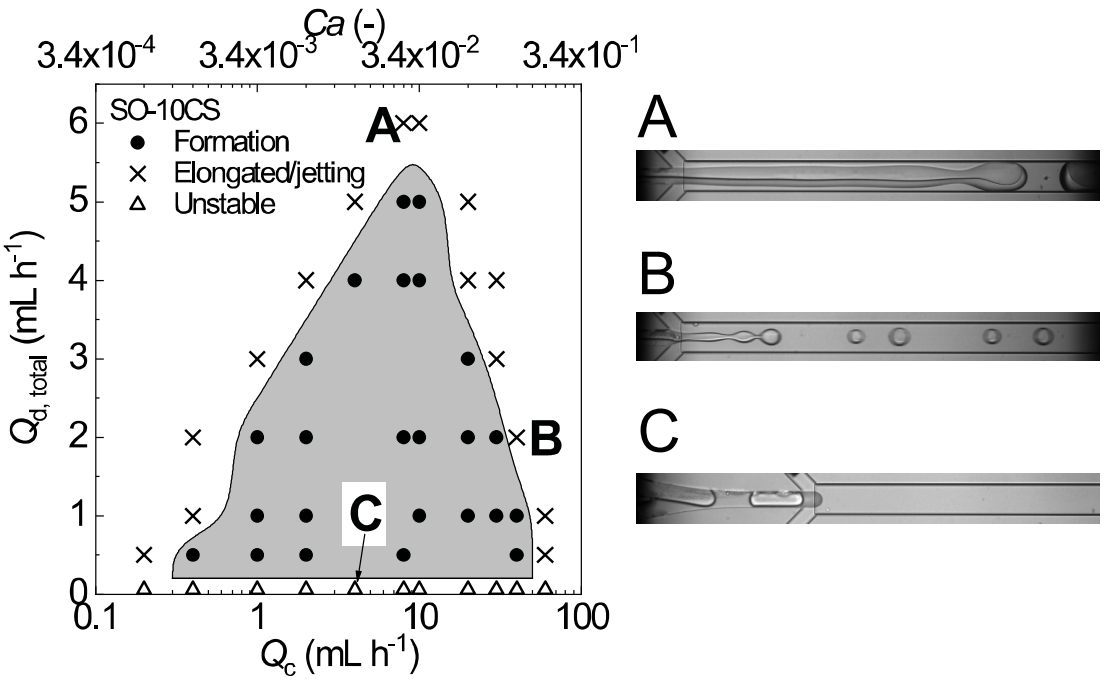

Figure 2.7 A phase diagram for the formation of biphasic droplets with 10-cSt silicone oil. The solid circles are the flow conditions where monodisperse biphasic droplets can form. The crosses are the flow conditions of the elongated steam (inset A) or irregular jetting regime (inset B). The open triangles are the conditions where the acrylate monomer and silicone oil cannot flow in parallel (inset C).

2.3.2.2 Effect of the viscosity of the silicone oil on the formation region

Microfluidic droplet formation is significantly affected by fluid viscosity. For example, it is reported that more viscous disperse phase produces larger droplets at the same flow-rate ratios between the disperse and continuous phases [45]. Therefore, we varied the viscosity of the silicone oil at 10, 20, 50, and 100 cSt and analyzed the flow conditions for generating biphasic droplets when we kept Q_m: $Q_s = 1$. The obtained flow diagrams have an enclosed mountain-shape [46] with the capillary number (Ca) ranging from 10^{-3} to 10^{-1} (Fig. 2.7). With the increase in silicone oil viscosity, the maximum flow rate of the two organic phases capable of producing biphasic droplets reduced gradually, making the region of monodisperse droplets smaller. These results were consistent with the previous study on oil-in-water droplet formation, which reported that the region for the dripping regime became larger when the disperse phase with lower viscosity was used [47].

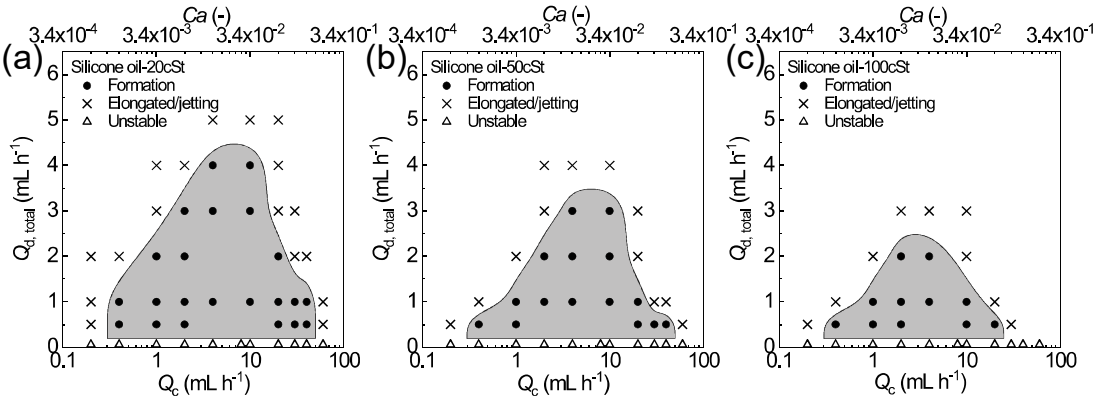

Figure 2.7 Flow pattern diagrams showing the conditions for generating biphasic droplets with different silicone oil viscosities: (a) 20 cSt; (b) 50 cSt; (c) 100 cSt.

2.3.2.3 Effect of the viscosity of the silicone oil and channel size on droplet formation

Next, for the droplets generated in the dripping regime, we analyzed the effect of silicone oil viscosity and channel size on the diameter (D_{avg}) and generation frequency (F) of biphasic droplets by tuning Q_c with a fixed Q_m and Q_s. The D_{avg} was defined as:

$$D_d = \sqrt[3]{\frac{Q_d}{6000\pi F}} \text{ [μm]} \tag{2-2}$$

When the same device was used, the difference in viscosities of silicone oils did not have a significant effect on both D_{avg} and F (Fig. 2.8). The increase of Q_c from 1.0 to 30.0 mL h^{-1} resulted in the decrease of D_{avg} from 325 to 105 μm with the CVs ranging from 1.0% to 4.5% (Fig. 2.8a); F and Q_c had a proportionality relationship and increased linearly from 14 to 434 droplets per second (Fig. 2.8b). These experimental results agreed well with the law discussed in Ref. 48, where the shear-driven breakup mechanism indicates that $D_{avg} \propto Q_c^{-1/3}$, leading to the proportionality relation $F \propto Q_c$. Meanwhile, in contrast to the silicone oil viscosities, the channel size had a significant impact on F and D_{avg}. When the droplets were produced in the flow-focusing geometry without a step [40, 45], F became ~2.2 times higher and D_{avg} was reduced by 20% at a fixed Q_c.

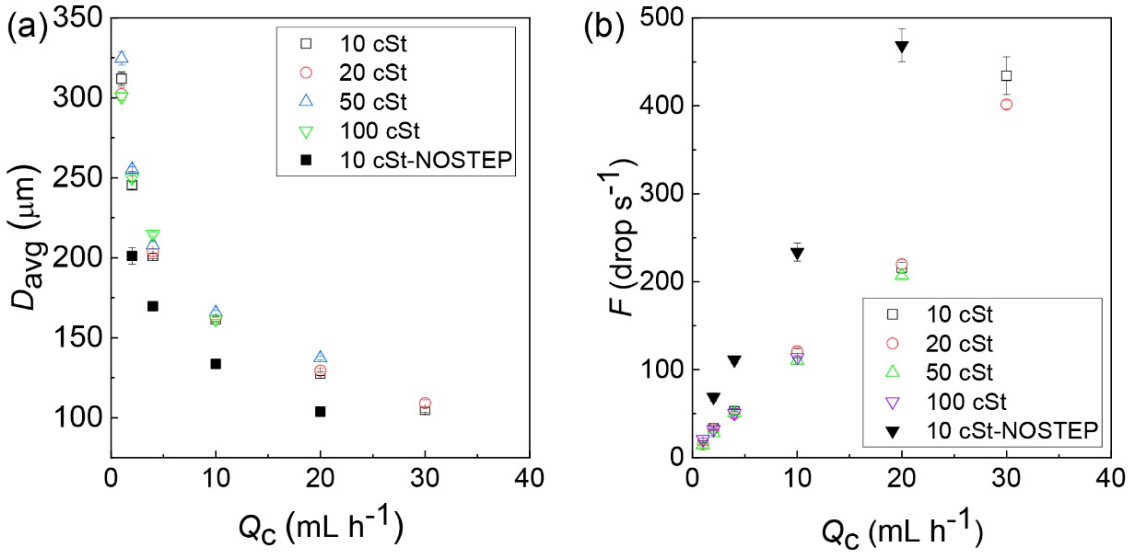

Figure 2.8 Effect of continuous phase flow rate Q_c on droplet size D_{avg} and generation frequency F, measured with silicone oils of different viscosities.

2.3.3 Characterization of generated biphasic droplets

In this section, the Janus-to-core shell transition of biphasic droplets at equilibrium is analyzed. We also demonstrate the effect of flow-rate ratios of two organic phases on the shell thickness of core-shell droplets.

2.3.3.1 Core-shell droplets evolved from Janus droplets based on minimization of interfacial energies

The generated biphasic droplets that flowed out the device through a 5-cm-long PTFE drain tube were collected on a glass slide, and their structure was immediately locked via photopolymerization. Both spherical and non-spherical particles were observed by SEM (Fig. 2.9), suggesting that the biphasic droplets were undergoing a morphological transition, and some of them did not reach the final equilibrium state within the residence time in the microfluidic device.

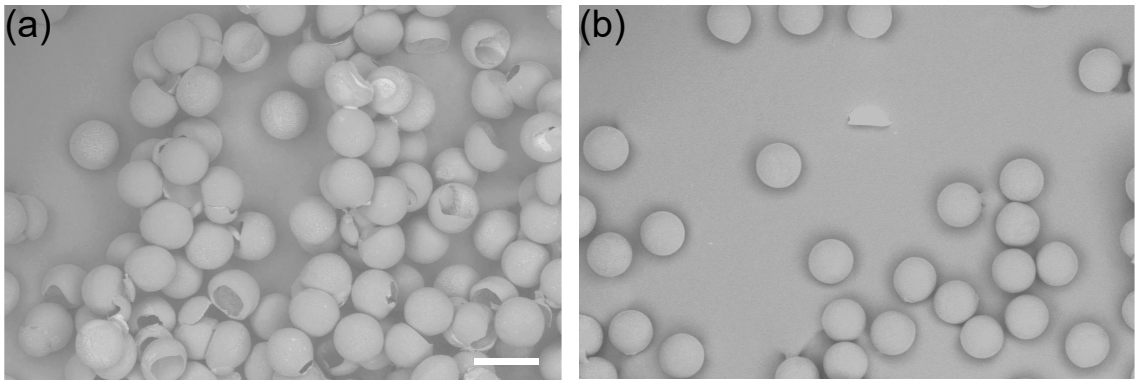

Figure 2.9 Particles obtained using different tube length (a) 5 cm, (b) 150 cm. Q_m:Q_s =1:1. $Q_{d,\,total}$ = 1.0 mL h^{-1}, Q_c = 6.0 mL h^{-1} × 2. Scale bar: 200 μm.

Next, we increased the length of the drainage tube to increase the residence time. When we used a 150-cm-long drain tube, the morphology of the particles became consistent (Fig. 2.9b), suggesting that the morphological transition was complete and the droplets reached the final equilibrium state before photopolymerization.

When a small biphasic droplet comprising of two immiscible phases is dispersed in another external phase, the body forces exerting on the droplet can be neglected compared to the surface forces, and the geometry of the biphasic droplets at equilibrium is given by the interfacial energies at three liquid-liquid interfaces. The relation between interfacial energies and the droplets morphology at equilibrium can be estimated by spreading parameters S_i, as described in **Section 1.2.3**.

In this study, phases 1 and 3 are SO and the HDDA, respectively, and the three interfacial tensions at the three interfaces, i.e. HDDA/PVA (γ_{31}) interface, HDDA/SO (γ_{12}) interface and SO/PVA (γ_{23}) interface measured by the interfacial tension measurement device were shown in Table 2.2. These values resulted in the condition $S_1 < 0$, $S_2 < 0$, $S_3 > 0$, indicating the droplets had a core-shell structure with an SO core and a monomer shell at equilibrium.

Table 2.2 Interfacial tensions among three liquid phases

γ_{23} (mN N^{-1})	γ_{31} (mN N^{-1})	γ_{12} (mN N^{-1})
1.1	2.3	10.8

2.3.3.2 Core-shell droplets with a tunable shell thickness

The shell thickness of the core-shell droplets could be flexibly tuned simply by changing the flow-rate ratios of the two droplet phases. Figure 2.10 showed the bright field micrographs of the core-shell droplets and their size distributions at different Q_m/Q_s ratios when we kept the total flow rate of two organic phases ($Q_{d,\,total} = Q_m+Q_s$) and Q_c as 1.0 mL h^{-1} and 20.0 mL h^{-1}, respectively. These droplets were observed immediately following the collection with a 150-cm-long drain tube. The uniform morphology in each condition indicated that the biphasic droplets reached the equilibrium state. As described above, the morphology of biphasic droplets at equilibrium was the core-shell state with a silicone oil core and a monomer shell, due to the minimization of interfacial energy. This reflected the morphology transition from Janus to core-shell state was complete. As Q_m/Q_s decreased from 9/1 to 1/9, the average of shell diameters varied in the range from 123 to 129 μm, while the average of core diameters increased from 56 to 125 μm, leading to the interfaces of the cores being closer to those of the shells. In all conditions, the core-shell droplets had uniform sizes with the CVs in the range of 1.3% to 3.3% for the cores, and 1.2% to 2.3% for the shells.

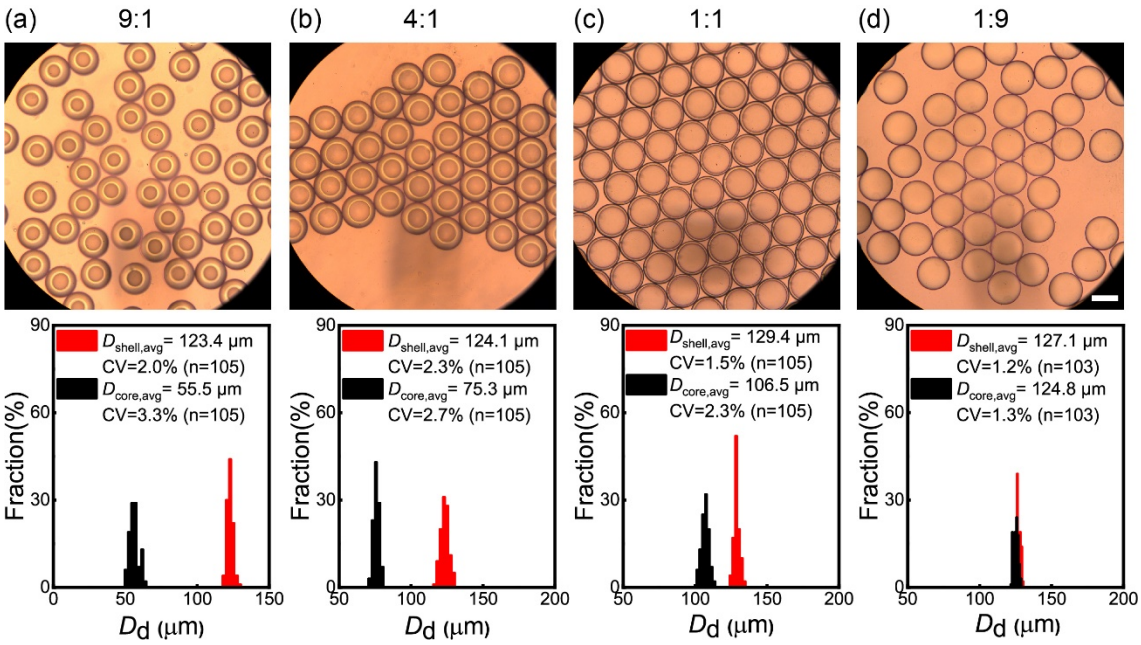

Figure 2.10 Monodisperse core–shell droplets and their size distributions obtained at various Q_m/Q_s ratios. (a) Q_m: Q_s = 9:1, (b) 4:1, (c) 1:1, and (d) 1:9. $Q_{d,\,total}$ =1.0 mL h^{-1}. Q_c = 10.0 mL h^{-1} × 2. Scale bar: 100 μm

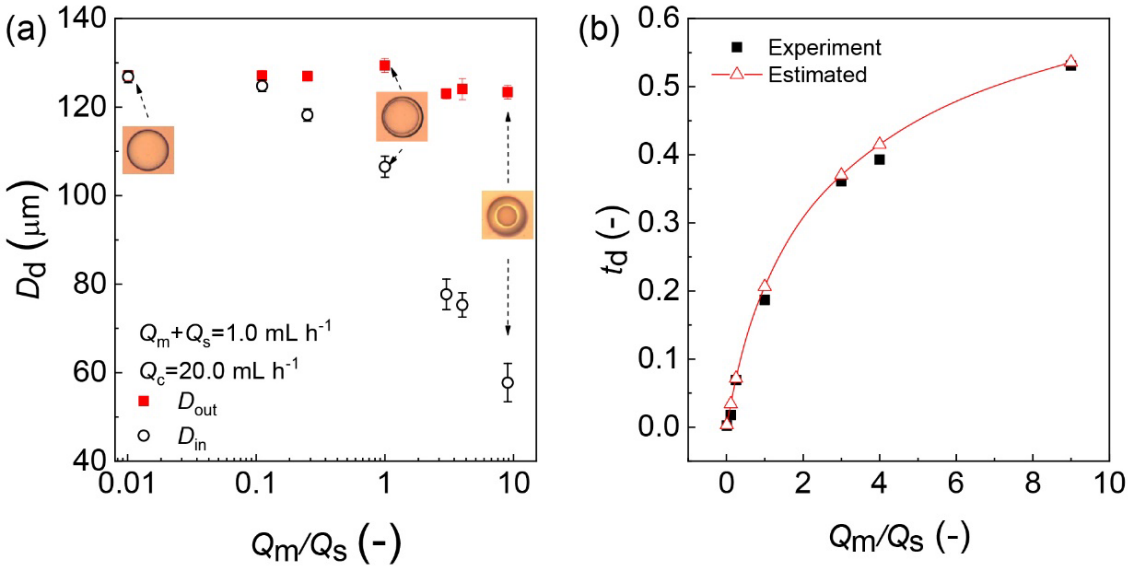

Figure 2.11 Tunable shell thickness of the core-shell droplets. (a) Effect of Q_m/Q_s on the inner (D_{in}) and outer (D_{out}) diameters of core-shell droplets. (b) Effect of Q_m/Q_s on relative shell thickness t_d. The solid line represents the estimation from equation (2-3). The t_d varies from 0.3% to 53% with the increase of Q_m/Q_s from 1/99 to 9/1. $Q_{d,\,total}$ = 1.0 mL h^{-1}, Q_c= 10.0 mL h^{-1} × 2.

The effect of Q_m/Q_s on the inner and outer diameters of the core-shell droplets is shown in Fig 2.11a. With the increase of Q_m/Q_s from 1/99 to 9/1, the outer diameter (D_{out}) did not change significantly (125 ± 4 μm), while the inner diameter (D_{in}) dramatically decreased from 127 μm to 56 μm. In this condition, the shell thickness varied from 1 μm to 67 μm. Thus, we could precisely control the thickness of the core-shell droplets by keeping $Q_{d,\,total}$, and Q_c constant and varying Q_m/Q_s. We define the relative thickness of the core-shell droplets (t_d) as

$$t_d = \frac{D_{out} - D_{in}}{D_{out}} = 1 - \left(1 + \frac{Q_m}{Q_s}\right)^{-1/3} \qquad (2\text{-}3)$$

Figure 2.11b shows the comparison between the experiment and the estimated results of t_d. The estimated t_d decreased from 53% to 0.3% by varying Q_m/Q_s from 9/1 to 1/99. The slight difference between the experiment and estimated results can be explained by the different values of refractive indices of light in the HDDA (n = 1.456) and the aqueous PVA solution (n =1.33), which cause a slight magnification of the cores. A similar phenomenon of difference between experiment and estimated results were found in core-shell droplets generated from the same materials at a T-junction, where t_d ranged from 30% to 0.4%, and the experiment results were slightly smaller than the estimated ones [31].

2.3.4 Fabrication of polymer microcapsules from core-shell droplets

In this section, the fabrication of microcapsules with tunable shell thickness from core-shell droplets via photo- and thermal polymerization is investigated. The effect of photo- and thermal initiator concentration on the fabrication of microcapsules with thinner and ultra-thin shell thickness is also discussed. Finally, the effect of the two polymerization methods on the surface morphology of the microcapsules is investigated.

2.3.4.1 Polymer microcapsules with tunable shell thickness via photopolymerization

For off-chip photopolymerization, the core-shell droplets produced at different Q_m/Q_s ratios were collected and exposed under UV light. The SEM images of the cross-linked particles and their cross-sections in Fig. 2.12 revealed that microcapsules with smooth surfaces could be obtained when Q_m/Q_s=3/1 and 1/1 respectively, with 2.0 wt.% photoinitiator concentration. The particles had narrow size distribution (average diameter 135 μm with a CV of 2.8% at Q_m: Q_s = 1:1), and the shell thickness could be varied by controlling the Q_m/Q_s.

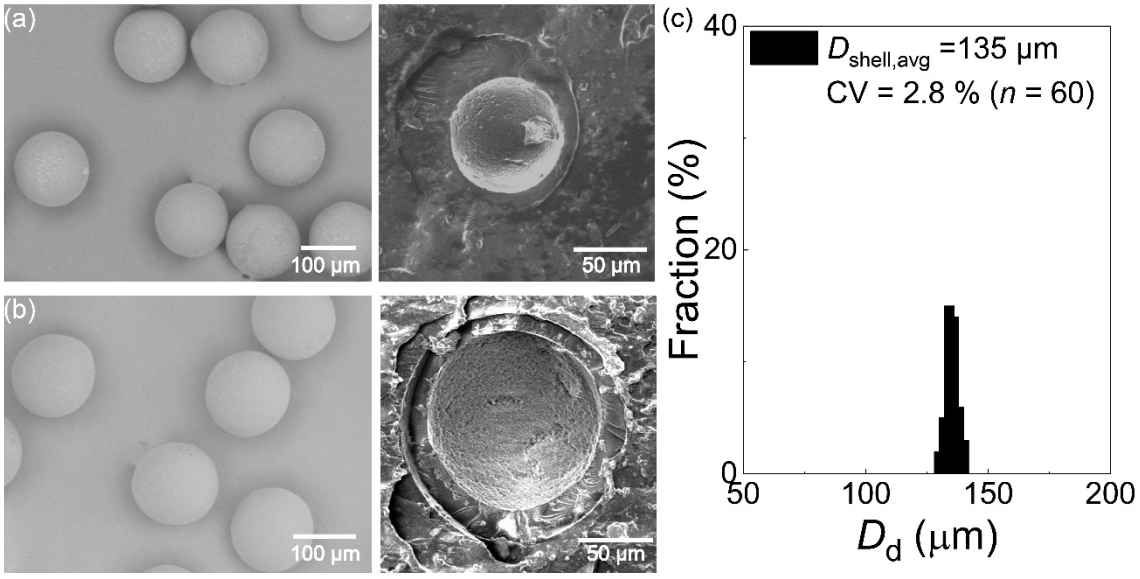

Figure 2.12 Surface morphology and cross-section of photo-polymerized capsules. (a-b) Surface morphology (left) and cross-section (right) images with different shell thickness. (a) Particles prepared with Q_m:Q_s =3:1; (b) Particles prepared with Q_m:Q_s =1:1; (c) Size distribution of the particles in (b). Initiator concentration of 2.0 wt.%. $Q_{d,\,total}$ = 1.0 mL h^{-1}, Q_c= 8.0 mL h^{-1} × 2. $Q_{d,\,total}$ = 1.0 mL h^{-1}, Q_c= 8.0 mL h^{-1} × 2.

2.3.4.2 Effect of photoinitiator concentration on polymerization

Next, the microcapsules with a thinner shell thickness were fabricated. Here, we found that the thinner shells of core-shell droplets generated at lower Q_m/Q_s of 1/9 could not be polymerized with the same 2.0 wt.% photoinitiator concentration. Meanwhile, the insufficient polymerization phenomenon was similarly observed in the previous study with a T-junction device [31]. In this previous study with initiator concentration at 1.0 wt%, the microcapsules could be produced at Q_m/Q_s =3/1, 1/1, 1/7, while the microcapsules with thinner shells at Q_m/Q_s =1/79 could not be fabricated.

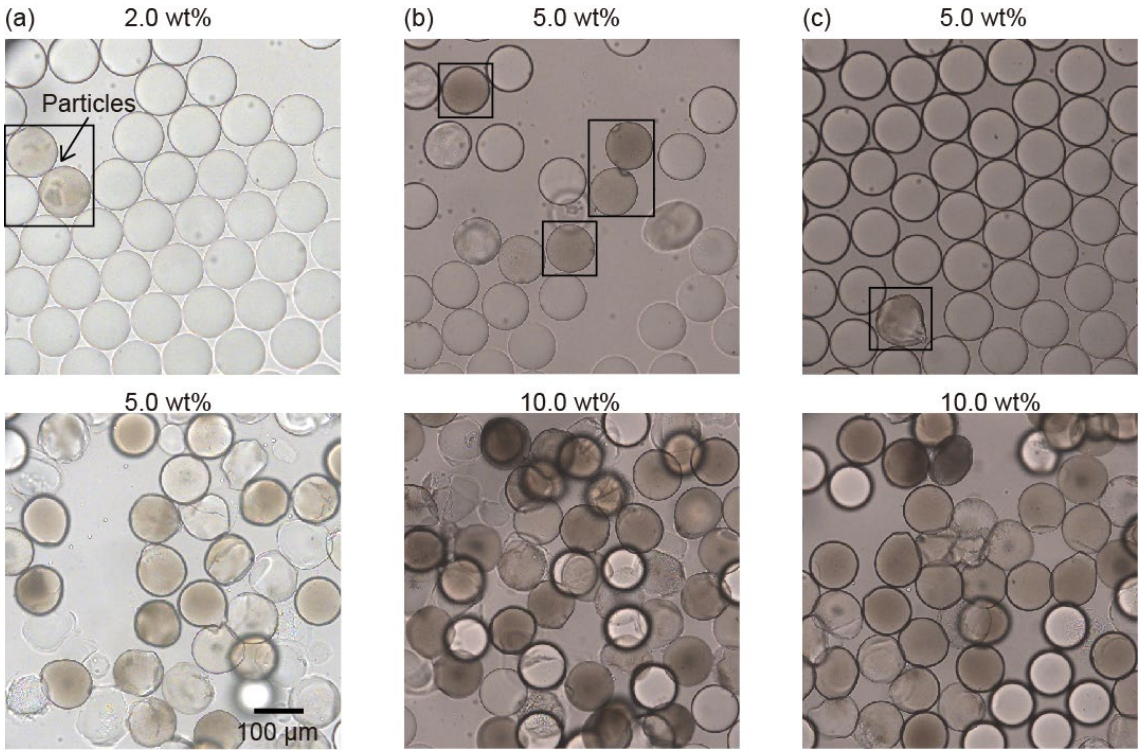

Figure 2.13 Bright-field photomicrographs of the photopolymerized oil-filled microcapsules at different photoinitiator concentration. (a) Particles prepared with Q_m:Q_s =1:9; (b) Particles prepared with Q_m:Q_s =1:24; (c) Particles prepared with Q_m:Q_s =1:99. Solidified particles had a dark color, as marked with black rectangles.

The effect of photoinitiator concentration on photopolymerization was investigated further. For example, as shown in Fig. 2.13, by increasing photoinitiator concentration from 2.0 wt.% and 5.0 wt.%, a larger number of photopolymerized particles could be observed at Q_m/Q_s= 1/9. In this way, we considered one possible reason for the insufficient polymerization phenomenon was the outward diffusion of the photoinitiator in the shell.

To further prove this assumption, the droplets at lower flow-rate ratios of Q_m/Q_s = 1/24 and 1/99 were also exposed under UV light. Although there was almost no particle solidified at an initial concentration of 5.0 wt.%, more photopolymerized particles could be observed when the photoinitiator concentration increased up to 10.0 wt.% (Fig. 2.14b, c). The results of the effect of photoinitiator concentration on solidifying droplets with different flow-rate ratios were summarized in Table 2.3, where ○ represents that it was easy to fabricated particles, △ represents that a small number of particles could be fabricated,

and × represents it was hard to fabricate.

Table 2.3 Effect of photoinitiator concentration on the solidification of droplets produced at different flow-rate ratios

Conc. / Q_m/Q_s	2.0 wt.%	5.0 wt.%	10.0 wt.%
3/1	○	-	-
1/1	○	-	-
1/9	×	○	-
1/24	×	△	○
1/99	×	×	○

2.3.4.3 Photopolymerized microcapsules with an ultra-thin shell thickness

Based on the abovementioned analysis, we confirmed that the method for fabricating microcapsules with thinner and ultra-thin shells could be photopolymerized successfully by simply increasing the initiator concentration. By increasing the concentration from 2.0 to 5.0 wt.%, microcapsules with thinner shells (2 μm thickness) could be fabricated at Q_m/Q_s = 1/9 (Fig. 2.14a). Moreover, microcapsules with ultra-thin shells (800 nm thickness) could be fabricated experimentally when Q_m/Q_s dropped to 1/99 with 10.0 wt.% photoinitiator concentration (Fig. 2.14b). The experimental shell thicknesses were close to the estimated results calculated using the abovementioned Eq. (2-3).

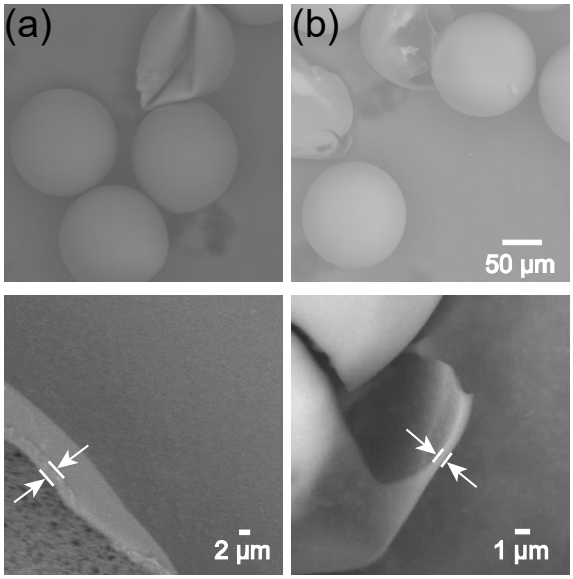

Figure 2.14 Surface morphology (top), and shell thickness (bottom) of the photopolymerized capsules. (a) Particles with thin shell prepared with Q_m:Q_s = 1:9 and 5.0 wt.% initiator concentration; (b) Particles with ultra-thin shell prepared with Q_m:Q_s = 1:99 and 10.0 wt.% initiator concentration. $Q_{d,\,total}$ = 1.0 mL h^{-1}, Q_c= 8.0 mL h^{-1} × 2.

2.3.4.4 Polymer microcapsules with tunable shell thickness via thermal polymerization

For off-chip thermal polymerization, we collected the core-shell droplets produced at different Q_m/Q_s ratios were received in a heated aqueous PVA solution. The SEM observation of the particles prepared at Q_m: Q_s = 9:1 with 2.0 wt.% thermal initiator concentration revealed that they were indeed microcapsules (Fig. 2.15a). Similarly, microcapsules could be obtained when Q_m/Q_s = 1/1 with 2.0 wt.% thermal initiator concentration (Fig. 2.15b). However, the thinner shell of core-shell droplets generated at a lower Q_m/Q_s ratio of 1/9 could not be polymerized with the same initiator concentration (2.0 wt.%), possibly due to the outward diffusion of the thermal-initiator in the shell.

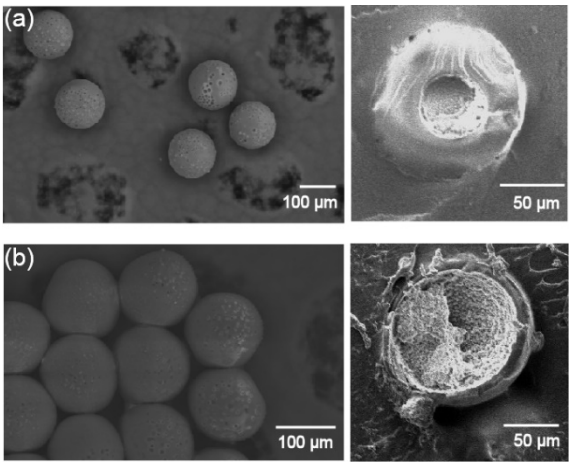

Figure 2.15 Surface morphology (left), cross-section and shell thickness (right) of thermally polymerized oil-filled microcapsules. (a) Particles prepared with Q_m:Q_s =9:1; (b) Particles prepared with Q_m:Q_s =1:1. Initiator concentration of 2.0 wt.%. $Q_{d,\,total}$ = 1.0 mL h^{-1}, Q_c= 8.0 mL h^{-1} × 2.

2.3.4.5 Effect of thermal initiator concentration on polymerization

By increasing the concentration from 2.0 to 5.0 wt.%, microcapsules with thinner shells (2 μm thickness) could be fabricated when Q_m/Q_s = 1/9 (Fig. 2.16a,b). Moreover, microcapsules with ultra-shells (800 nm thickness) could be fabricated when Q_m/Q_s = 1/99 with 15.0 wt % thermal initiator concentration (Fig. 2.16c,d). The results of the effect of thermal initiator concentration on solidifying droplets with different flow-rate ratios were summarized in Table 2.4.

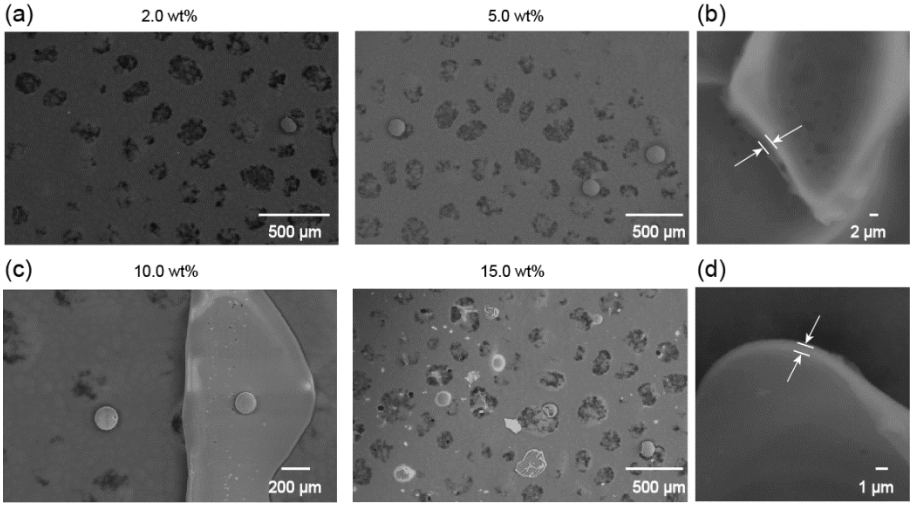

Figure 2.16 SEM images of thermally cross-linked particles at different thermal initiator concentration. (a) Particles prepared with Q_m:Q_s = 1:9 and initiator concentrations of 2.0 wt.% (left) and 5.0 wt.% (right); (b) Shell thickness of the capsules in (a); (c) Particles prepared with Q_m:Q_s = 1:99 initiator concentrations of 10.0.wt% (left) and 15.0 wt % (right); (d) Shell thickness of the capsules in (c). $Q_{d,\,total}$ = 1.0 mL h^{-1}, Q_c = 8.0 mL h^{-1} × 2.

Table 2.4 Effect of thermal initiator concentration on solidifying droplets with different flow-rate ratios

Conc. / Q_m/Q_s	2.0 wt%	5.0 wt%	10.0 wt%	15.0 wt%
9/1	○	-	-	-
1/1	○	-	-	-
1/9	×	○	-	-
1/99	×	×	△	○

2.3.4.6 Comparison between photo- and thermally-induced polymerization

We found that the thermally induced polymerized capsules had many pores on their surfaces, and the surfaces of the microcapsules became smoother when the shells became thinner (Q_m/Q_s decreased from 9/1 to 1/99). Meanwhile, the photopolymerized capsules had smooth surfaces at all the flow-rate ratios (Fig. 2.17).

The porous surface morphology of the thermally cross-linked microcapsules was presumably because the Nitrogen−Nitrogen double bond cleavage of the thermal initiator V-65 (Fig. 2.18) in the HDDA shell produced nitrogen during the thermally induced polymerization. When Q_m/Q_s = 9/1, we consider the relatively thick shell enabled the accumulation and growth of nitrogen bubbles in it, causing the formation of pores on the shells during the solidification. However, with the decrease of volume fraction of HDDA (Q_m/Q_s decrease from 9/1 to 1/99), the shell became thinner, and then the produced nitrogen was released directly without accumulation, resulting in the smoother surfaces.

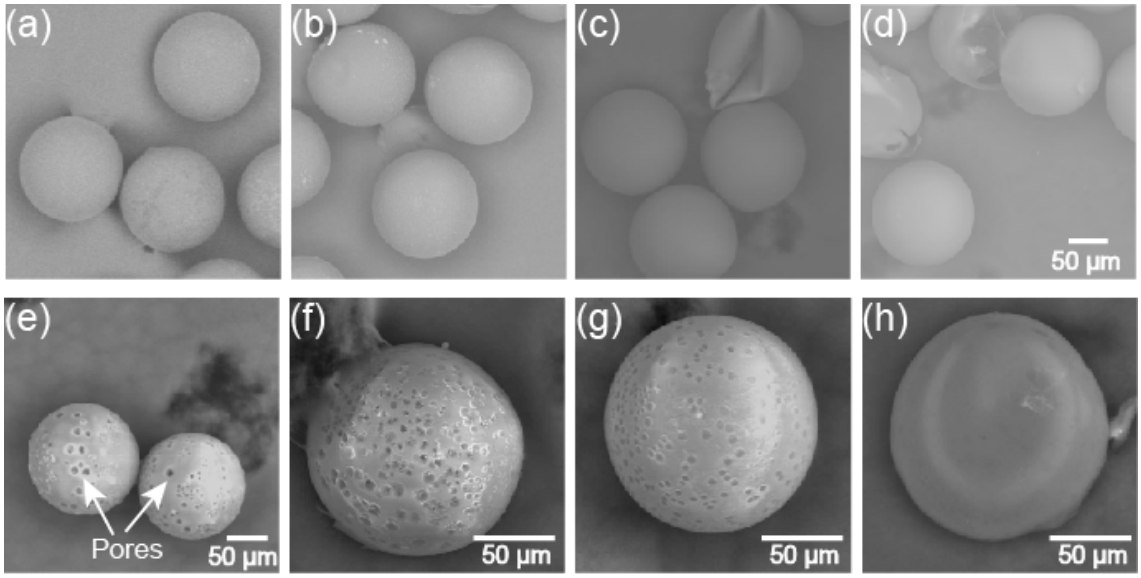

Figure 2.17 Surface morphology of polymerized capsules. (a-d) Photopolymerized particles prepared with (a) Q_m:Q_s = 3:1 (b) Q_m:Q_s = 1:1. (c) Q_m:Q_s = 1:9. (d) Q_m:Q_s = 1:99. (e-h) Thermally polymerized particles prepared with (a) Q_m:Q_s = 9:1 (b) Q_m:Q_s = 1:1. (c) Q_m:Q_s = 1:9. (d) Q_m:Q_s = 1:99. $Q_{d,\,total}$ = 1.0 mL h^{-1}, Qc = 8.0 mL h^{-1} × 2.

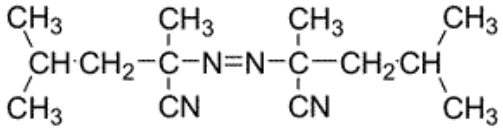

Figure 2.18 Chemical structure of thermal initiator

In the future, we believe our method of increasing the initiator concentrations can be used to fabricate microcapsules of thinner shell thickness, if the biphasic droplets could be produced successfully at a lower Q_m/Q_s ratio.

2.4 Summary

In this chapter, structural evolution of microfluidic biphasic droplets from Janus to core-shell forms was presented. The synthesis of oil-filled polymeric microcapsules with a tunable shell thickness via photo- or heat-induced polymerization was also described. The contents of each section are summarized below.

In the **Introduction** section 2.1, the applications of polymer microcapsules the previous fabrication methods were introduced. Then, the purpose of this study was clarified.

In the **Materials and experimental methods** section 2.2, the device fabrication and assembly, materials for generating droplets, polymerization methods of microcapsules, and peripheral equipment for experiment and characterization were presented.

Results and discussion section 2.3 is summarized as below:

2.3.1 Formation of biphasic droplets. We confirmed that the biphasic droplets prepared at the flow-focusing junction had Janus morphology at various flow-rate ratios between the two droplet phases.

2.3.2 Hydrodynamic effect on biphasic droplet formation. The possible flow rate range for droplets generated at the dripping regime was studied. In this dripping regime, monodisperse core-shell drops with average diameters range from 105 to 325 μm with CVs of 1.0–4.5% could be produced by adjusting the continuous phase flow rate.

2.3.3 Characterization of generated biphasic droplets. Interfacial-tension driven transition of the biphasic droplets from Janus to core-shell state was confirmed. Then, by

adjusting the flow-rate ratios of two organic phases, core-shell droplets with tunable shell thickness at the range of 1–67 μm could be produced.

2.3.4 Fabrication of polymer microcapsules from core-shell droplets. Both photo- and thermal polymerization methods were studied. The polymer microcapsules with an ultra-thin shell thickness of 800 nm could be synthesized when the concentrations of photo- and thermal initiators were sufficiently increased. Compared with the photopolymerized capsules with smooth surfaces, the thermally cured microcapsules had many pores on their surfaces.

2.5 References

[1] Madene, A.; Jacquot, M.; Scher, J.; Desobry, S. *Int. J. Food Sci. Technol.* 41, 1 (2006).

[2] McClements, D. J.; Decker, E. A.; Weiss, J. *J. Food Sci.* 72, 109 (2007).

[3] Peña, B.; Panisello, C.; Aresté, G.; Garcia-Valls, R.; Gumí, T. *Chem. Eng. J.* 179, 394 (2012).

[4] Jacquemond, M.; Jeckelmann, N.; Ouali, L.; Haefliger, O. P. *J. Appl. Polym. Sci.* 114, 3074 (2009).

[5] Zhao, C. X. *Advanced Drug Delivery Reviews* 65, 1420 (2013).

[6] Comiskey, B.; Albert, J. D.; Yoshizawa, H.; Jacobson, J. *Nature* 394, 253 (1998).

[7] Usami, T.; Igarashi, A. *J. Inf. Record* 22, 347 (1996).

[8] Zhang, C. B.; Gao, W.; Zhao, Y. J.; Chen, Y. P. *Appl. Phys. Lett.* 113, 203702 (2018).

[9] Wu, D. Y.; Meure, S.; Solomon, D. *Prog. Polym. Sci.* 33, 479 (2008).

[10] Hwang, Y. K.; Jeong, U.; Cho, E. C. *Langmuir*, 24, 2446 (2008).

[11] Shchukin, D. G.; Shutava, T.; Shchukina, E.; Sukhorukov, G. B.; Lvov, Y. M. *Chem. Mater.* 16, 3446 (2004).

[12] Cho, J. S.; Kwon, A.; Cho, C. G. *Colloid Polym. Sci.* 280, 260 (2002).

[13] Arshady, R. *Polym. Eng. Sci.* 30, 905 (1990).

[14] Akamatsu, K.; Chen, W.; Suzuki, Y.; Ito, T.; Nakao, A.; Sugawara, T.; Kikuchi, R.; Nakao, S.I. *Langmuir* 26, 14854 (2010).

[15] Hennequin,Y.; Pannacci, N.; de Torres, C. n. P.; Tetradis-Meris, G.; Chapuliot, S.; Bouchaud, E.; Tabeling, P. *Langmuir* 25, 7857 (2009).

[16] Peng, S. L.; Zhang, M. Y.; Niu, X. Z.; Wen, W. J.; Sheng, P. *Appl. Phys. Lett.* 92, 012108 (2008).

[17] Choi, S. W.; Zhang, Y.; Xia, Y. N. *Adv. Funct. Mater.* 19, 2943 (2009).

[18] Windbergs, M.; Zhao, Y.; Heyman, J.; Weitz, D. A. *J. Am.Chem. Soc.* 135, 7933 (2013).

[19] Tan, W. H.; Takeuchi, S. *Adv. Mater.* 19, 2696 (2007).

[20] Okushima, S.; Nisisako, T.; Torii, T.; Higuchi, T. *Langmuir* 20, 9905 (2004).

[21] Nisisako, T.; Okushima, S.; Torii, T. *Soft Matter* 1, 23 (2005).

[22] Seo, M.; Paquet, C.; Nie, Z. H.; Xu, S. Q.; Kumacheva, E. *Soft Matter* 3, 986 (2007).

[23] Chen, C. H.; Abate, A.R.; Lee, D.Y.; Terentjev, E. M.; Weitz, D.A.; *Adv. Mater.* 21, 3201 (2009).

[24] Perro, A.; Nicolet, C.; Angy, J.; Lecommandoux, S.; LeMeins, J. F.; Colin, A. *Langmuir* 27, 9034 (2011).

[25] Chu, L.Y.; Utada, A. S.; Shah, R. K.; Kim, J. W.; Weitz, D. A. *Angew. Chem. Int. Ed.* 46*,* 8970 (2007).

[26] Kim, S. H.; Jeon, S. J.; Yang, S. M. *J. Am. Chem. Soc.* 130, 6040 (2008).

[27] Bocanegra, R.; Sampedro, J. L.; Gañán-Calvo, A.; Marquez, M. *J. Microencapsulation* 22, 745 (2005).

[28] Liu, L.; Yang, J. P.; Ju, X. J.; Xie, R.; Yang, L.; Liang, B.; Chu, L. Y. *J. Colloid Interface Sci.* 336, 100 (2009).

[29] Yu, Y. L.; Zhang, M. J.; Xie, R.; Ju, X. J.; Wang, J. Y.; Pi, S. W.; Chu, L. Y. *J. Colloid Interface Sci.* 376, 97 (2012).

[30] Abate, A. R.; Kutsovsky, M.; Seiffert, S.; Windbergs, M.; Pinto, L. F.; Rotem, A.; Utada, A. S.; Weitz, D. A. *Adv. Mater.* 23, 1757 (2011).

[31] Nisisako, T.; Hatsuzawa, T. *Sens. Actuator B-Chem.* 223, 209 (2016).

[32] Vladisavljević, G. T.; Shum, H. C.; Weitz, D. A. *UK Colloids 2011*, 115 (2012).

[33] Utada, A. S.; Lorenceau, E.; Link, D. R.; Kaplan, P. D.; Stone, H. A.; Weitz, D. A. *Science* 308, 537 (2005).

[34] Chen, P. W.; Erb, R. M.; Studart, A. R. *Langmuir* 28, 144 (2012).

[35] Chen, R.; Dong, P. F.; Xu, J. H.; Wang, Y. D.; Luo, G. S. *Lab Chip* 12, 3858 (2012).

[36] Kim, S. H.; Kim, J. W.; Cho, J. C.; Weitz, D. A. *Lab Chip* 11, 3162 (2011).

[37] Abbaspourrad, A.; Carroll, N. J.; Kim, S. H.; Weitz, D. A. *J. Am. Chem. Soc.* 135, 7744 (2011).

[38] Kim, S. H.; Park, J. G.; Choi, T. M.; Manoharan, V. N.; Weitz, D. A. *Nat. Commun.* 5, 3068 (2014).

[39] Nisisako, T.; Torii, T.; Takahashi, T.; Takizawa, Y. *Adv. Mater.* 18, 1152 (2006).

[40] Nisisako, T. *Curr. Opin. Colloid Interface Sci.* 25, 1 (2016).

[41] López-Juárez, B. P.; García-Ramírez, M. A.; Pérez-Luna, V. H.; Gonzalez-Reynoso, O. *Mater. Today: Proc.* 13, 374 (2019).

[42] Mastiani, M.; Seo, S.; Riou, B.; Kim, M. *Biomed. Microdevices* 21, 50 (2019).

[43] Vladisavljević, G. T.; Kobayashi, I.; Nakajima, M. *Microfluid. Nanofluid.* 13, 151 (2012).

[44] Seemann, R.; Brinkmann, M.; Pfohl T.; Herminghaus, S. *Rep. Prog. Phys*. 75, 016601 (2012).

[45] Nie, Z. H.; Seo, M. S.; Xu, S. Q.; Lewis, P. C.; Mok, M.; Kumacheva, E.; Whitesides, G. M.; Garstecki, P.; Stone, H. A. *Microfluid. Nanofluid.* 5, 585 (2008).

[46] Nisisako, T.; Torii, T. *Adv. Mater.* 19, 1489 (2007).

[47] Wu, Z.; Cao, Z.; Sunden, B. *ASME 2017 Summer Heat Transfer Conference* Bellevue, Washington, USA, July 9-12 (2017).

[48] Garstecki, P.; Fuerstman, M. J.; Stone, H. A.; Whitesides, G. M. *Lab Chip* 6, 437 (2006).

Chapter 3

Microfluidic formation of surfactant-laden Janus droplets

3.1 Introduction

3.1.1 The properties and preparation methods of Janus droplets

Janus droplets are compound droplets that consist of two physically and chemically distinct exposed segments, and they have attracted significant interest recently due to their unique and promising properties. For example, Janus droplets can be used as templates in the fabrication of various functional microparticles, which are valuable for potential applications as electrically and magnetically driven actuators [1–2], interfacial stabilizers [3], and building blocks for self-assembly [4]. A conventional method such as vibration mixing [5] was reported to prepare Janus droplets comprised of mutually immiscible silicone oil and vegetable oil phases (Fig. 3.1), but it is facing a problem of their broad size distribution and poor control over compositions.

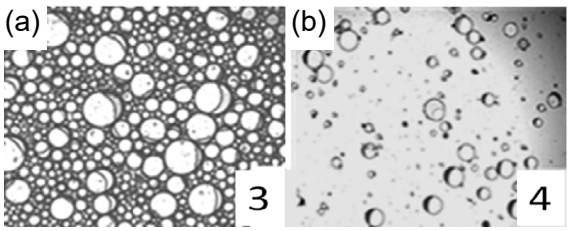

Figure 3.1 Janus droplets prepared by vibration mixing [5]. (a-b) Janus droplets generated in (a) 0.3 and (b) 0.9 weight fraction of external phase.

3.1.2 Microfluidic formation of Janus droplets

Nowadays, droplet microfluidics has been used to produce Janus droplets, comprising two miscible [7] or two immiscible segments [8], with extreme control over size and shape. For the produced microfluidic Janus droplets having two miscible segments, the convective and diffusive transport causes the mixture between the two segments over time. Meanwhile, Janus droplets comprised of two immiscible segments can keep their configuration, based on the minimization of interfacial free energy among the three liquid phases, without mixture of the two segments. For instance, Nisisako et al. reported the formation of Janus droplets, comprising two immiscible curable and non-curable segments, which could be used as templates for fabricating lens-shaped polymer particles [9–11]. In general, two microfluidic approaches can be used to prepare Janus droplets with two immiscible segments: (a) solvent-evaporation-induced phase separation within a droplet [12] and (b) formation of a two-phase parallel stream by introducing two immiscible disperse phases separately. The approach (a) is a time-consuming process, and it needs a suitable co-solvent. Approach (b) is realized through emulsifying the parallel stream into a co-flowing continuous phase as biphasic droplets, by using the microfluidic devices with different geometries including T-shaped [13], flow-focusing [8–11], and 3D microcapillaries [3,14].

3.1.3 Microfluidic Janus droplets with controlled morphology

Morphology of the microfluidic Janus droplets comprised of two immiscible compartments has a strong relationship with their application [8]. Typically, two approaches can be applied to control the morphology of Janus droplets:

(a) Flow-rate-ratio based control

One widely used approach to control the morphology of Janus droplets was based on controlling the volume ratio of the two Janus segments, through adjusting the flow-rate ratios of the two Janus compartments. The poly(N-isopropyl acrylamide) Janus hydrogels with controlled shapes, for example, were fabricated from water-in-oil (W/O) Janus droplets generated in the polydimethylsiloxane (PDMS) microfluidic device[15]. Also, Weitz, et al. [16] reported the formation of oil-in-water (O/W) Janus droplets with

controlled shapes in a capillary microfluidic device, suitable for fabricating crescent-moon-shaped amphiphilic polymer particles (Fig. 3.2).

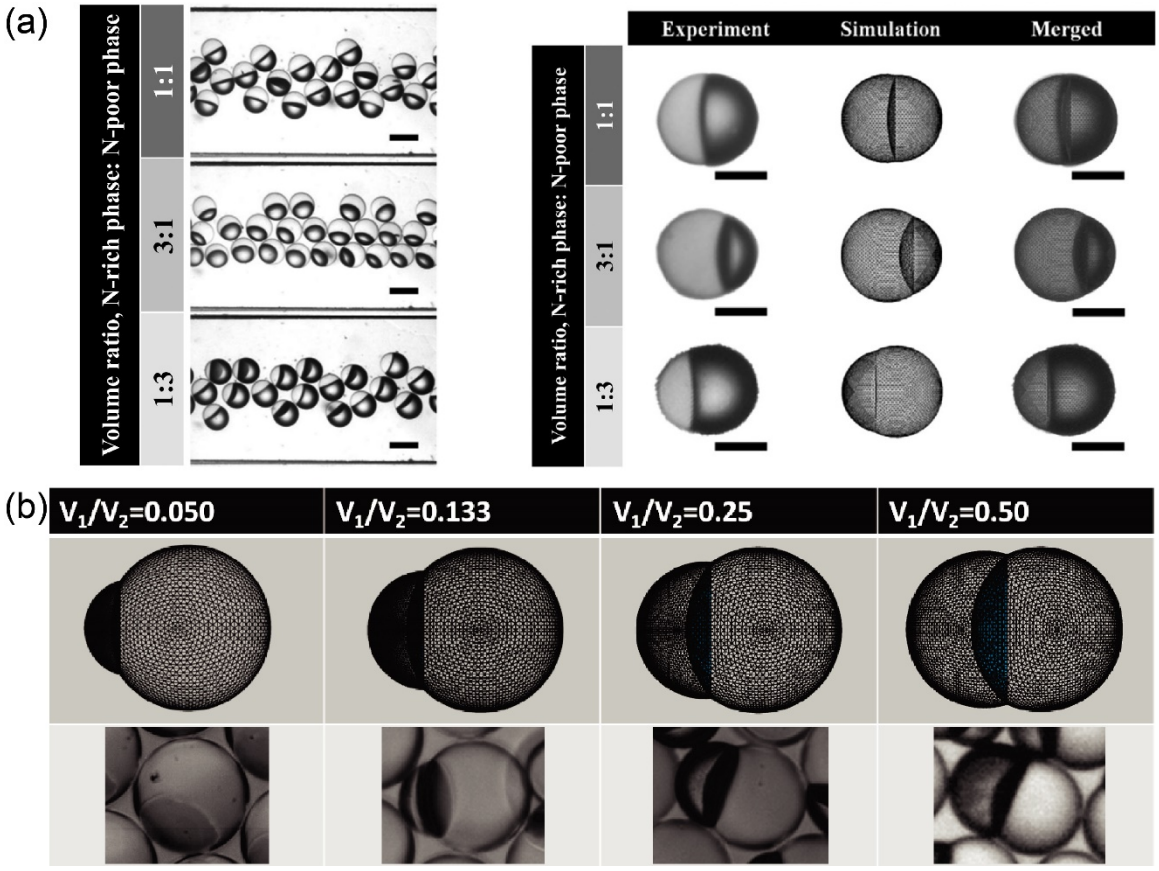

Figure 3.2 Flow-rate-ratio based controlled shape variation of Janus droplets for fabricating particles. (a) W/O Janus droplets obtained in the experiment (left) and simulation (right) for fabricating Janus hydrogels [15]. Scale bars: 100 μm; (b) O/W Janus droplets obtained in simulation (top) and experiment (bottom) for fabricating crescent-moon-shaped amphiphilic polymer particles with controlled shapes [16].

(b) Interfacial-tension driven control

Another approach is to control the interfacial tensions between three liquid phases. This approach was inspired by the fact that the morphology of a biphasic droplet with two immiscible phases, suspended in another continuous phase, is determined by three interfacial tensions [17]. For example, for the microfluidic Janus droplets comprised of

PLGA [poly(lactic-co-glycolic acid)] and silicone oil (SO), the variation in shapes was demonstrated by increasing the concentrations of polyvinyl alcohol (PVA) in the external aqueous phase from 0 to 10 wt.% [18]. Also, Ge et al. reported the spherical-to-dumbbell shape transformation of microfluidic Janus droplets, comprising liquid paraffin and ethoxylated trimethylolpropane triacrylate (ETPTA), through replacing the ambient solution collected in a petri dish between pure water and a 2.0 wt.% aqueous solution of Pluronic F-127 [19]. Furthermore, Zarzar et al. reported the variation in morphology of compound droplets from core-shell and Janus states by using the stimuli-responsive surfactants (Fig. 3.3) [20].

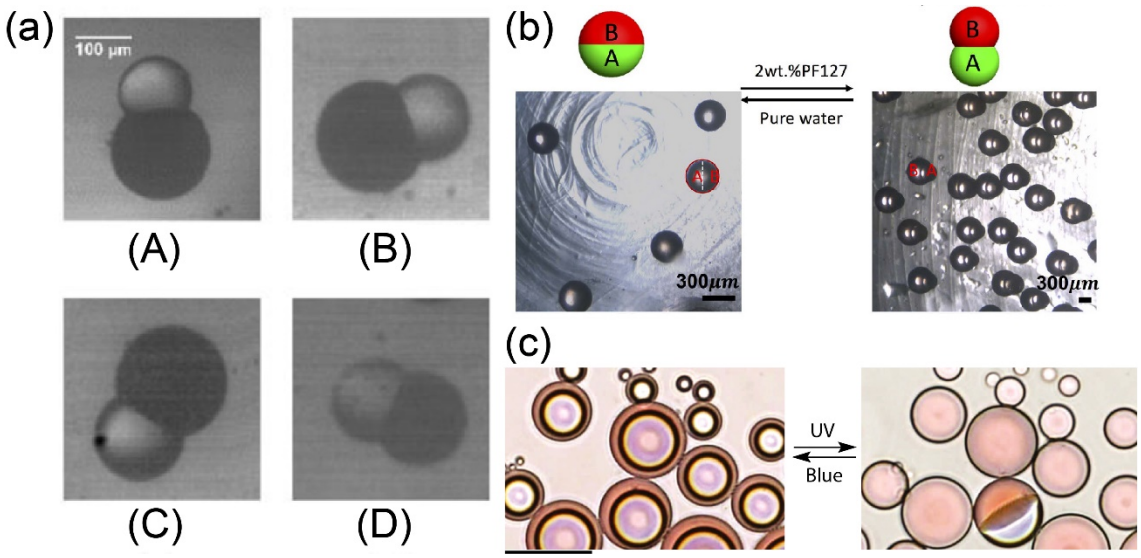

Figure 3.3 Interfacial-tension driven control controlled shape variation of Janus droplets for fabricating particles. (a) Morphologies of Janus droplets dispersed inthe aqueous PVA solution at various concentrations:(A) 0.2 wt.%; (B) 2.0 wt.%;(C) 4.5 wt.%; (D) 10.0 wt.% [18]. (b) Janus droplets comprised of liquid paraffin and ETPTA having spherical morphology in deionized water (left) and dumbbell morphology in a 2.0 wt.% aqueous solution of Pluronic F-127 (right) [19]. (c) Light-responsive surfactant molecules reversibly alternates the morphology of compound droplets between the core-shell and Janus states under ultraviolet (UV) and blue light [20]. Scale bar: 50 μm.

The abovementioned studies focused on controlling Janus droplets morphology through adjusting the surfactant concentrations in the continuous phase. To our knowledge, however, control of Janus droplet morphologies simply via adjusting the surfactant concentrations in the dispersed phase has never been reported. Previously, Nisisako et al. demonstrated the generation of microfluidic Janus droplets with a photocurable acrylate monomer and non-curable SO containing a surfactant in an aqueous sodium dodecyl sulfate (SDS) solution, suitable for fabricating biconvex polymer microlenses for use in micro-optics and imaging applications [9,11]. However, one shortcoming of these droplets is their instability against coalescence after collection, reducing the yield efficiency. Therefore, there remains a significant challenge in producing new microfluidic Janus droplets with controlled shapes and enhanced stability against coalescence for fabricating lens-shaped polymer particles.

3.1.4 Objectives

In this chapter, we aim to produce novel microfluidic Janus droplets with controlled morphology and improved stability against coalescence for the fabrication of lens-shaped microparticles.

3.1.5 Outline

In the 3.1 section, the advantages of the microfluidic approach for producing monodisperse Janus droplets comprised of two immiscible segments, in comparison with the general method were stated. Then, the importance of shape variation of Janus droplets for fabricating polymer particles was introduced. Finally, the existing problems in the current approach for producing microfluidic Janus droplets with controlled shape/size were pointed, which act as the research objective in this research.

In the 3.2 section, the microfluidic device, materials used for droplet formation, peripheral equipment for observation and characterization of the products, and morphology simulation of droplets and particles are demonstrated.

In the 3.3 section, the experiment results and discussion are described in four parts including the formation of surfactant-laden droplets (3.3.1), the effect of inner surfactant

concentration on Janus morphology (3.3.2), stability assessment of Janus droplets (3.3.3), and fabrication and characterization of microlens-shaped particles (3.3.4).

In the 3.4 section, the results of this study are summarized.

3.2 Materials and experimental methods

3.2.1 Materials and peripheral equipment

Materials and peripheral equipment in this experiment are as follows:

Name	Company
1, 6-hexanediol diacrylate (HDDA)	Shin-Nakamura Kagaku, Wakayama, Japan
Silicone oil	Dow Corning Toray, Tokyo, Japan
Polyvinyl alcohol (PVA)	Mitsubishi Chemical Corporation, Tokyo, Japan
Sodium dodecyl sulfate (SDS)	Fujifilm Wako Pure Chemical Corporation, Osaka, Japan
Cyclopentasiloxane and polyoxyethylene glycol/polyoxypropylene glycol-19/19 dimethicone (BY11-030)	Dow Corning Toray, Tokyo, Japan
2-Hydroxy-2-methylpropiophenone (Darocur 1173)	Ciba Japan K. K., Japan
2,2'-Azobis (2,4-dimethylvaleronitrile) (V-65)	Fujifilm Wako Pure Chemical Corporation, Osaka, Japan
Oil-soluble dye (Oil Red O)	Sigma-Aldrich, MO, USA
Deionized water	Merck Direct-Q UV, Tokyo, Japan
Acetone	Fujifilm Wako Pure Chemical Corporation, Osaka, Japan
Ethanol	Fujifilm Wako Pure Chemical Corporation, Osaka, Japan
Glass syringes (1000 series)	Hamilton Company, NV, USA
Syringe pumps (KDS200)	KD Scientific, MA, USA
Slide glass (S111)	Matsunami Glass Industry, Tokyo, Japan
Optical microscope (BX-51)	Olympus, Tokyo, Japan
High-speed video camera (Fastcam Mini AX50)	Photron, Tokyo, Japan
Scanning electron microscope (SEM, JSM-6610LA)	JEOL, Tokyo, Japan
Ultra-violet (UV) light source (LA-410UV)	Hayashi-repic, Tokyo, Japan
Software ImageJ	National Institute of Health, NY, USA

Surface Tensiometer (B100)	Asumi Giken, Tokyo, Japan
Ceramic hot stirrer (CHPS-170DN)	AS ONE Corporation, Tokyo, Japan
Nylon mesh sheet (42 μm × 42 μm)	Tokyo Screen, Tokyo, Japan

3.2.2 Microfluidic device

The same microfluidic flow-focusing device described in Chapter 2 was used, which had a Y-shaped channel and a deeper drainage channel (Fig. 3.4). The Y-shaped channel is used for two organic phases, with two co-flowing channels for aqueous streams of 100 μm deep and 100 μm wide around the sheath-focusing junction; the drainage channel is 200 μm deep and 200 μm wide. The cross-section of microchannels is rectangular. The device was prepared on a glass chip (15 × 15 × 3.5 mm^3, for details, see Appendix A.1) [22].

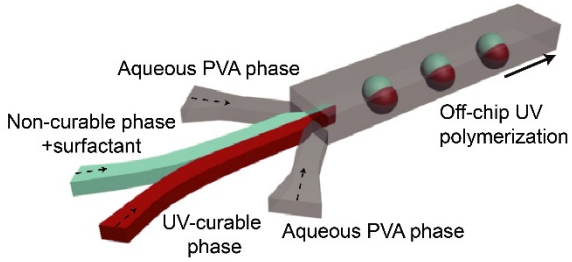

Figure 3.4 Schematic illustration of a microfluidic biphasic droplet generator with a deeper drainage region for generating Janus droplets.

3.2.3 Chemicals

An acrylate monomer (HDDA, dynamic viscosity η_m = 6.35 mPa s, density ρ_m = 1.02 g cm^{-3}) was used as the curable disperse phase. For photo-induced polymerization, a photoinitiator (Darocur 1173) was dissolved in HDDA to prepare a 2.0 wt.% mixture. For thermal polymerization, a thermal initiator (V-65) was dissolved in HDDA to prepare a 2.0 wt.% mixture. For a non-curable disperse phase, a surfactant (BY11-030, HLB 3.5) was dissolved in 10-cSt SO (SH200-10CS) to prepare mixture solutions with concentrations ranging from 0.1 to 5.0 wt.%. For the continuous aqueous phase to produce surfactant-laden Janus droplets, PVA (GL-03, M_w ~20,000 g mol^{-1}, 87%–89% hydrolyzed) was dissolved in deionized water to prepare a 2.0 wt.% mixture. For the continuous aqueous phase to produce surfactant-free Janus droplets, SDS was dissolved in deionized water to

prepare a 0.3 wt.% mixture. To visually differentiate the two organic phases, the oil-soluble dye (Oil Red O) was dissolved into the HDDA solution.

3.2.4 Formation and characterization of droplets

Three syringe pumps and glass syringes were used to infuse the fluids into the microfluidic device to generate droplets. The droplet formation in the microfluidic device was monitored using an optical microscope equipped with a high-speed video camera. The interfacial tensions between the two liquids were measured using the pendant drop method. We used the software ImageJ to measure the aperture diameters of Janus droplets.

3.2.5 Preparation and characterization of polymer microparticles

Polymer particles were prepared by solidifying generated droplets via an off-chip photo- or thermally induced polymerization. To prepare photo-polymerized particles, the curable segments of the generated Janus droplets were solidified continuously via off-chip photopolymerization using an ultraviolet (UV) light source with an irradiation distance of approximately 15–20 cm. To prepare thermally polymerized particles, the generated droplets were guided into a plastic cup containing the PVA solution directly via the PTFE tube. The plastic cup was placed in a beaker containing pure water and heated to 80–85 °C, monitored by a thermometer using a ceramic hot stirrer.

The products were filtered using a nylon mesh sheet to remove smaller particles produced from satellite droplets. The particles were lightly washed using acetone (> 99.5%) and ethanol (> 99%) to remove residual non-curable fluid and dust. We also used a scanning electron microscope to observe the shape of the polymer particles.

3.2.6 Morphology simulation of droplets and particles

Surface Evolver was used to simulate the effect of interfacial tensions on the shape of surfactant-laden Janus droplets and resultant particles [23]. The Surface Evolver is an interactive program for the study of surfaces shaped by surface tension and other energies.

When the user defines an initial surface in a data file. The software evolves the surface toward minimal energy by a gradient descent method.

To simulate the morphology of the Janus droplets at equilibrium, we defined the surfaces represented by the basic geometric elements including vertices, edges, facets, and bodies. The surfaces bounded two bodies (Fig. 3.5). In this way, by defining the interfacial tensions, and volumes of two bodies, the morphology of the Janus droplets at equilibrium was calculated.

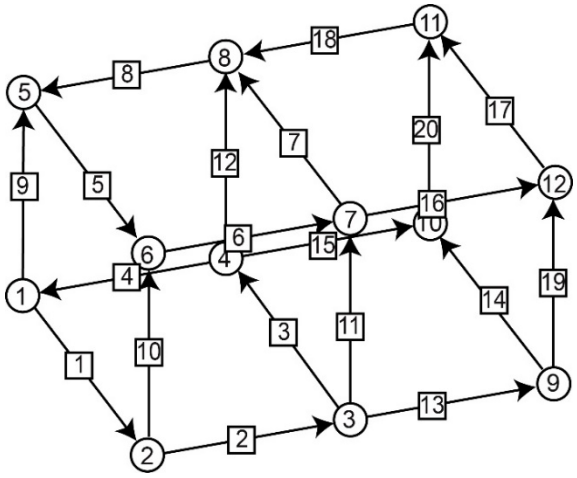

Figure 3.5 The cube skeleton for simulating the morphology of the Janus droplets at equilibrium. The circles and rectangules represented the vertices and edges, respectively.

3.3 Results and discussion

3.3.1 Formation of surfactant-laden Janus droplets

3.3.1.1 Biphasic droplets formed in a microfluidic flow-focusing device

Monodisperse biphasic droplets could be generated around the junction one by one when we infused HDDA and SO containing the surfactant at 0.1 wt.% as the two disperse phases and the aqueous PVA solution as the continuous phase at appropriate flow rates. For example, by setting the flow rates of HDDA (Q_m), SO (Q_s), and the aqueous PVA solution (Q_c) at 0.3, 0.3, and 8.0 mL h^{-1}, respectively, the two organic phases were emulsified into the aqueous PVA solution as a biphasic droplet within 14 ms, with the production rate of ~78 drops s^{-1} (Fig. 3.6a). By observing the droplets flowing through the

drainage tube (Fig. 3.6b), their Janus morphology could be confirmed more clearly than the droplets immediately following their break-off, indicating interfacial-energy-driven structural evolution.

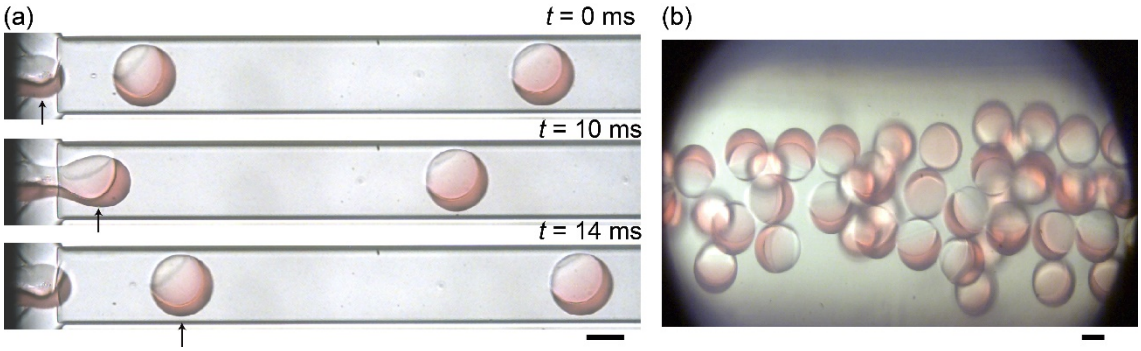

Figure 3.6 Formation of surface-laden Janus droplets. (a) Sequential high-speed photomicrographs showing the break-off of a Janus droplet. Arrows indicate the observed droplet (b) Biphasic droplets in (a) flowing through the drain tube. The flow rate ratio of acrylate monomer (Q_m) and silicone oil (Q_s) is Q_m: Q_s = 1:1. The total flow rate of two organic phases ($Q_{d,\ total} = Q_m + Q_s$) is 0.6 mL h^{-1}, and the flow rate of the aqueous PVA phase (Q_c) is 4.0 mL h^{-1} × 2. Scale bars: 100 μm.

The volume ratios of the two Janus compartments could be varied easily by changing the flow-rate ratio of the two disperse phases. For example, the formation of surface-laden Janus droplets at Q_m: Q_s = 9:1 and Q_m: Q_s = 11:1 were shown in Fig. 3.7.

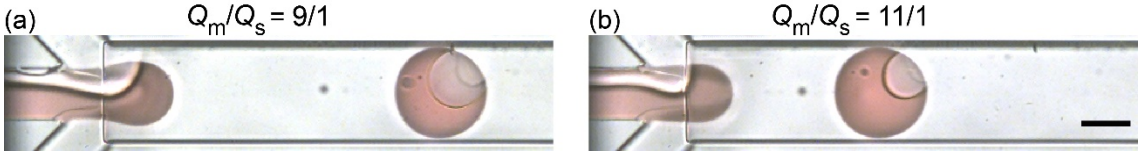

Figure 3.7 Formation of surface-laden Janus droplets at (a) Q_m: Q_s = 9:1.and (b) Q_m: Q_s = 11:1. $Q_{d,\ total}$ = 0.6 mL h^{-1}, Q_c = 8.0 mL h^{-1}. Scale bar: 100 μm.

3.3.1.2 Formation region of surfactant-laden Janus droplets

By modulating the flow rates under low Reynolds and capillary number conditions, the formation region of Janus droplets with a surfactant concentration of 0.1 wt.% was plotted as shown in Fig. 3.8. The open triangles represent the condition where the HDDA

and SO two-phase parallel stream became unstable (inset A). The crosses represent the condition of elongated steam (inset B) or irregular jetting regime (inset C).

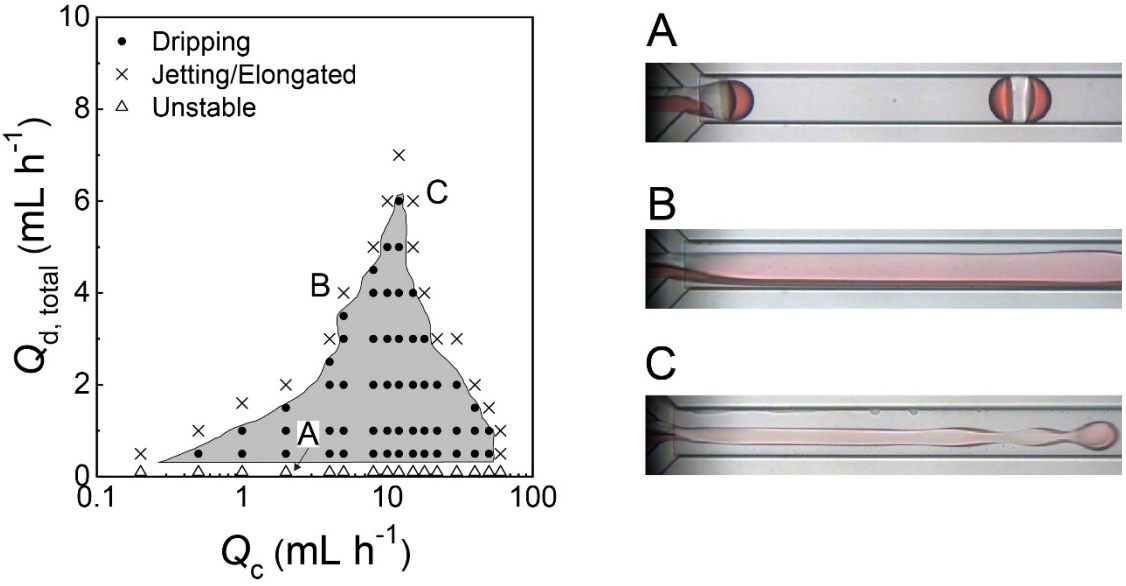

Figure 3.8 A flow pattern diagram showing the condition for the formation of Janus droplets with the surfactant concentration of 0.1 wt.%.

3.3.1.3 Effect of flow rate on droplets size and generation frequency

For the droplets produced in the dripping regime in Fig. 3.8, the effect of continuous phase flow rate on droplet size and generation frequency was investigated by varying Q_c from 1.0 to 30.0 mL h^{-1} while Q_m and Q_s kept equal values of 0.2 or 0.4 mL h^{-1}. As shown in Fig. 3.9, with the increase of Q_c, the production rate (F) increased from 18 to 205 drop s^{-1}, on the other hand, the droplet size (D_{avg}) and decreased from 101 to 242 μm. Also, for a fixed Q_c, higher Q_m and Q_s ($Q_m = Q_s = 0.4$ mL h^{-1}) obtained higher F and Q_c.

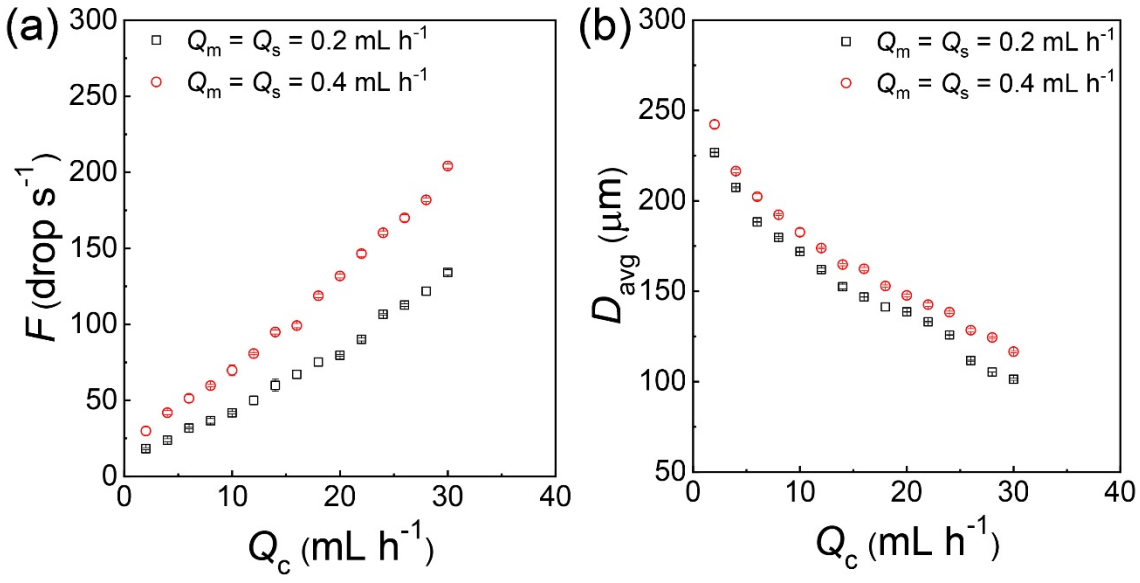

Figure 3.9 (a) The continuous phase flow rate Q_c vs. generation frequency F. (b) The Q_c vs. average diameter of the biphasic droplets D_{avg}, calculated from F and $Q_{d,\,total}$, based on the assumption that droplets are spherical.

3.3.1.4 Characterization of produced surfactant-laden Janus droplets

Figure 3.10a showed the off-chip optical image of the surfactant-laden Janus droplets produced at Q_m/Q_s = 1/1. All the droplets had a snowman-like Janus geometry, where a concave-convex HDDA and biconvex SO segments were separated by a curved inner interface. Both the aperture diameters of the HDDA (D_m) and SO (D_s) segments were uniform in size, with coefficient-of-variation (CV) values of ~ 2% (Fig. 3.10b).

The aperture diameters could be controlled by changing the Q_m/Q_s ratio, and keeping the sum of Q_m and Q_s constant (= 0.6 mL h^{-1}). As Q_m/Q_s increased from 1/9 to 19/1, D_m increased from 103 to 168 μm with the CV varied from 1.0% to 2.2%, and D_s decreased from 162 to 75 μm with the CV varied from 0.8% to 2.4% (Fig. 3.11a). The optical images of droplets generated at Q_m/Q_s = 1/9 and 19/1 were shown in Fig. 3.11b.

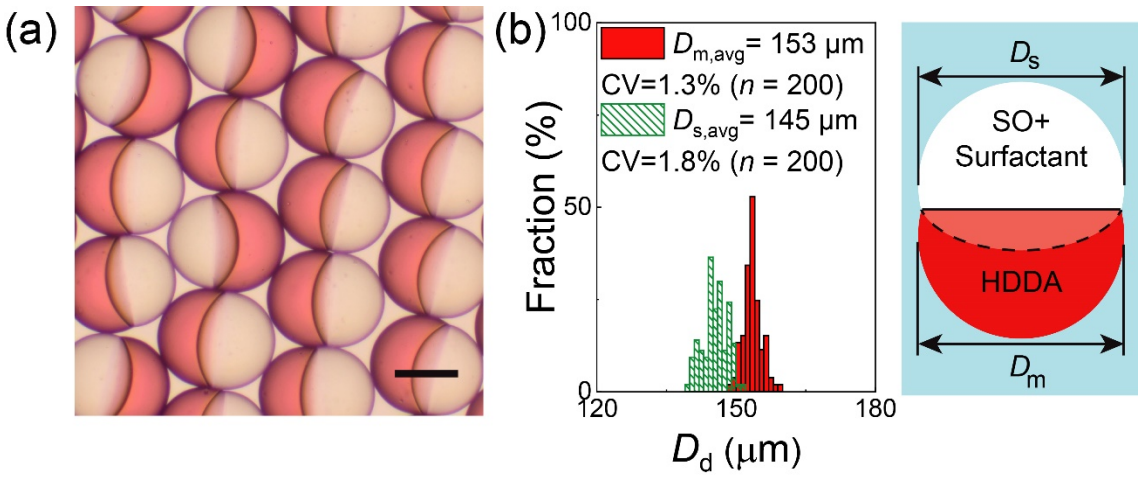

Figure 3.10 Characterization of Janus droplets with a surfactant concentration of 0.1 wt.% at equilibrium. (a) Photomicrograph of Janus droplets generated at Q_m: Q_s = 1:1; (b) Size distributions of Janus segments in (a). The inset explains the measured dimensions of D_m and D_s. Q_m : Q_s = 1:1. $Q_{d,\,total}$ = 0.6 mL h^{-1}, Q_c = 4.0 mL h^{-1} × 2. Scale bar: 100 μm.

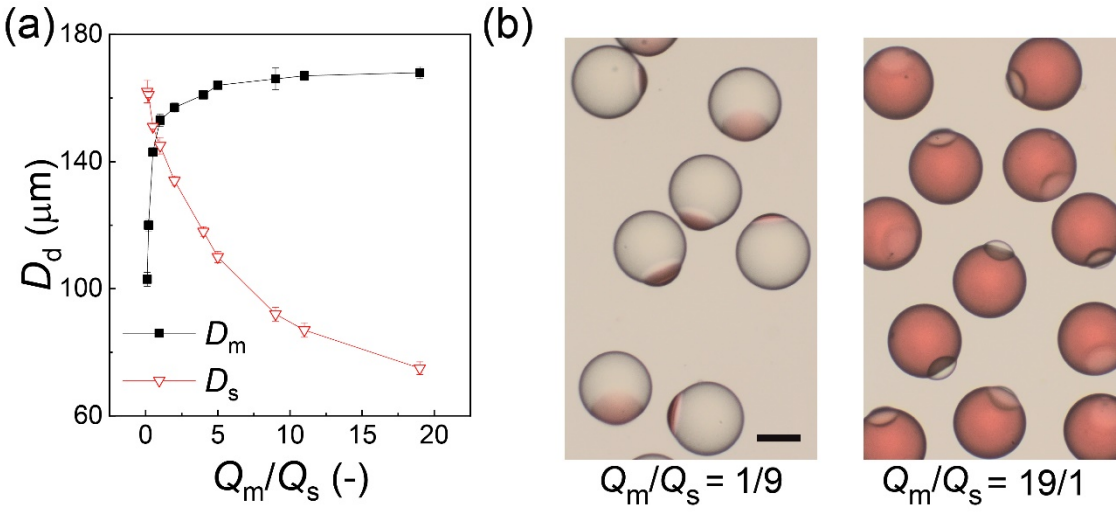

Figure 3.11 (a) Experimental relationship between Q_m/Q_s and droplet size. (b) Photomicrographs of Janus droplets generated at Q_m:Q_s = 1:9 (left) and 19:1 (right) when $Q_{d,\,total}$ = 0.6 mL h^{-1} and Q_c = 8.0 mL h^{-1}. Scale bar: 100 μm.

3.3.1.5 Effect of the presence of surfactant on biphasic droplets morphology

In Chapter 2, we reported that the biphasic droplets comprised of HDDA and SO without surfactant formed a core-shell geometry in an aqueous PVA solution at equilibrium [21, 22]. In contrast, in this chapter, we confirmed that the addition of the surfactant to the

SO phase resulted in the biphasic droplets with Janus morphology at equilibrium. This difference in morphology can be explained by spreading parameters $S_i = \gamma_{jk} - (\gamma_{ij} + \gamma_{ki})$ [17], where, γ_{jk}, $\gamma_{jk,}$ and γ_{jk} are the three interfacial tensions at the three interfaces ($i \neq j \neq k = 1$, 2, 3); see details in Section 1.2.4.

Next, we measured the three interfacial tensions and calculated the three spreading parameters to illustrate this difference in morphology. Here, phase 1 and 3 were SO and HDDA, respectively. In the Chapter 2 without a surfactant [21], three interfacial tension values were $\gamma_{31} = 2.2$ mN m^{-1}, $\gamma_{12} = 10.8$ mN m^{-1}, and $\gamma_{23} = 1.1$ mN m^{-1}, thereby causing $S_1 < 0$, $S_2 < 0$, $S_3 > 0$, forming a core-shell structure. Meanwhile, in this study, the addition of surfactant in SO at the concentration of 0.1 wt.% caused the values of γ_{31} and γ_{12} changed to $\gamma_{31} = 1.63 \pm 0.07$ mN m^{-1} and $\gamma_{12} = 9.61 \pm 0.06$ mN m^{-1}, while γ_{23} maintained a value of 1.13 ± 0.02 mN m^{-1} ($n = 5$). These values correspond to the core-shell condition ($S_1 < 0$, $S_2 < 0$, $S_3 > 0$), which is inconsistent with the Janus morphology we confirmed in our experiments. One possible reason for this discrepancy is that there might be some HDDA molecules at the interface between the SO and the aqueous PVA phases, reducing the interfacial energy at the SO/water interface [8]. This reduced interfacial tension (γ'_{12}) was estimated using the following equation [24]:

$$\gamma'_{12} = \gamma_{23} \cos\alpha + \gamma_{31} \cos\beta \tag{3-1}$$

where α and β are the contact angles, as shown in Fig. 3.12. We obtained $\alpha = 10.4° \pm 1.0°$ and $\beta = 35.6° \pm 0.6°$ ($n = 5$) here, thus we calculated γ'_{12} ~2.17 mN m^{-1}. This satisfies $S_1 < 0$, $S_2 < 0$, $S_3 < 0$, corresponding to the condition for a Janus morphology.

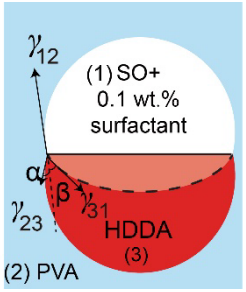

Figure 3.12 Schematic illustration of a Janus droplet with the surfactant concentration in the SO segment of 0.1 wt.%. Q_m:Q_s = 1:1.

3.3.2 Effect of loaded surfactant concentration on Janus morphology

3.3.2.1 Formation of Janus droplets with different inner surfactant concentration

First, surfactant-laden biphasic droplets with the concentration ranging from 0.1 to 5.0 wt.% were produced. The Q_m/Q_s ratio were set at 1/2, 1/1, and 2/1 (Fig. 3.13).

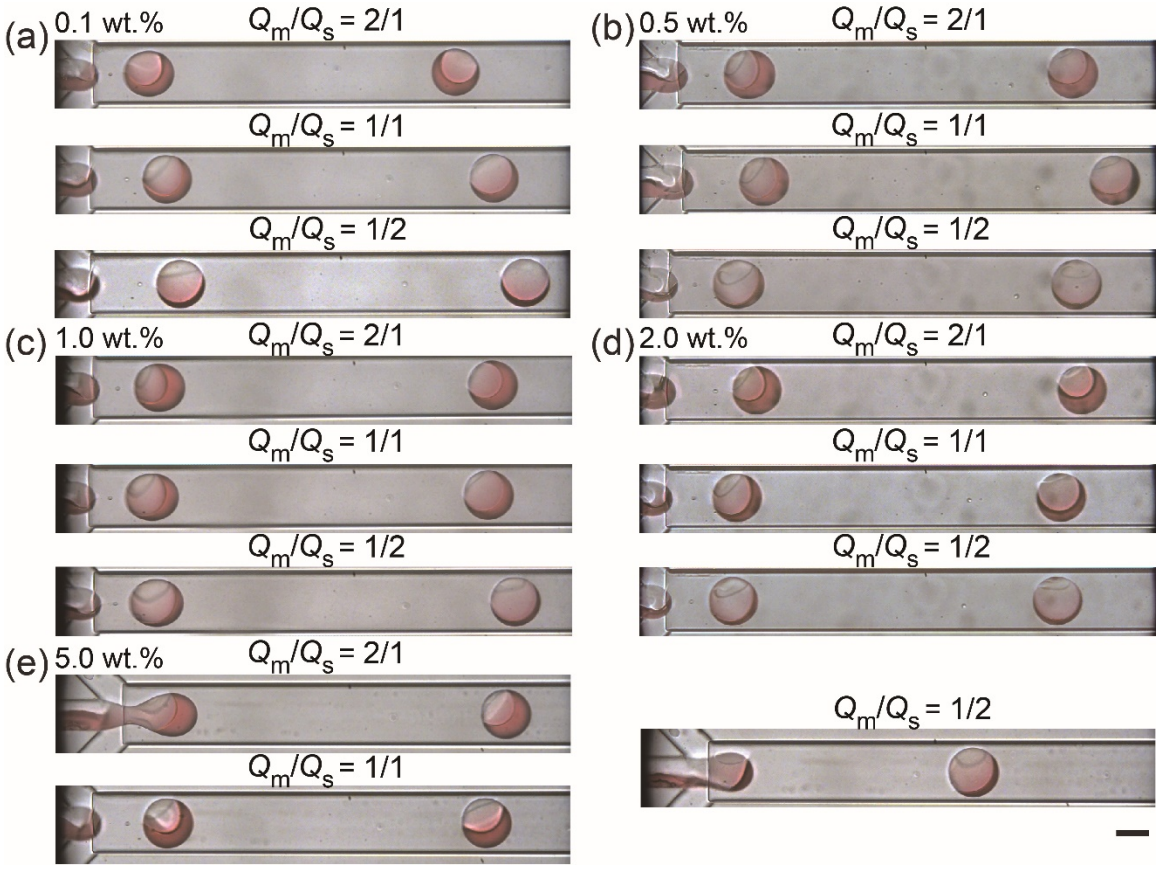

Figure 3.13 Formation of Janus droplets in the aqueous PVA solution with the concentration of surfactant in the silicone-oil segment at (a) 0.1 wt.%, (b) 0.5 wt.%, (c) 1.0 wt.%, (d)2.0 wt.%, and (e) 5.0 wt.%, produced with Q_m/Q_s at 2/1, 1/1 and 1/2. $Q_{d,\,total}$ = 0.6 mL h^{-1}, Q_c = 8.0 mL h^{-1}. Scale bar: 100 μm.

3.3.2.2 Morphology comparison between experiment and simulation

The produced droplets were collected on a glass slide. Different Janus morphologies were observed when surfactant concentration in the SO phase varied from 0.1 to 5.0 wt.% under the flow rate ratios of Q_m/Q_s = 1 (Fig. 3.14). Typically, the increase of surfactant concentration in the SO phase caused the curvature variation of the inner HDDA/SO

interface, leading to a variation in the shape of the HDDA segment from concave-convex to biconvex, and that of the SO segment from biconvex to concave-convex. At low surfactant concentrations (0.1, 0.5, or 1.0 wt.%), the HDDA and SO segments of the droplets had a concave-convex shape and a biconvex shape, respectively (Fig. 3.14A–C). At surfactant concentration of 2.0 wt.%, the two segments became hemispherical separated by the planar interface (Fig. 3.14D). At surfactant concentration of 5.0 wt.%, Janus droplets with biconvex HDDA and concave-convex SO segments were observed (Fig. 3.14E).

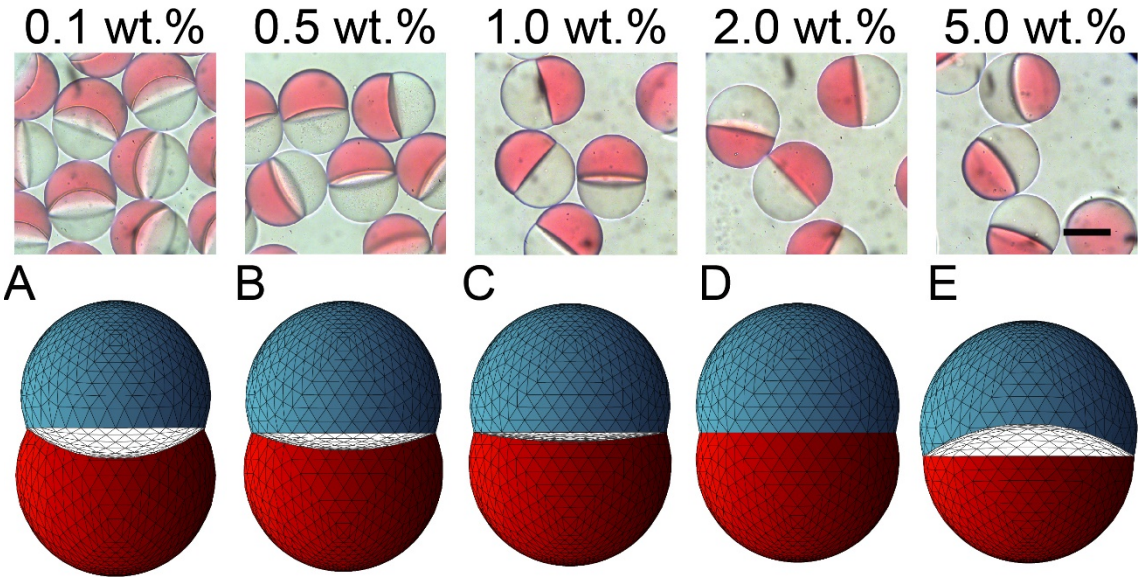

Figure 3.14 Photomicrographs showing a structural variation of Janus droplets carrying surfactant at concentrations ranging from 0.1 to 5.0 wt.% (top) and their corresponding calculated 3D shapes (A to E, bottom). Flow conditions were $Q_m = Q_s = 0.3$ mL h^{-1}, and $Q_c = 8.0$ mL h^{-1}. Scale bar: 100 μm.

A similar variation in the curvature of the inner HDDA/SO interface could also be confirmed as the surfactant concentration was varied at Q_m/Q_s ratios of 1/2 and 2/1, although the ranges of the concentrations for the concave-convex and biconvex shapes were different. For the droplets produced at $Q_m/Q_s = 2/1$, the HDDA and SO segments presented concave-convex and biconvex shapes, respectively when the surfactant concentration was in the range from 0.1 to 2.0 wt.%. At 5.0 wt.%, the HDDA and SO segments became biconvex and concave-convex, respectively (Fig. 3.15a). Meanwhile, For

the droplets produced at Q_m/Q_s = 1/2, concave-convex HDDA and biconvex SO segments were obtained when the concentration was below 0.5 wt.%, while biconvex HDDA and concave-convex SO segments were obtained when the concentration was above 0.5 wt.% (Fig. 3.15b).

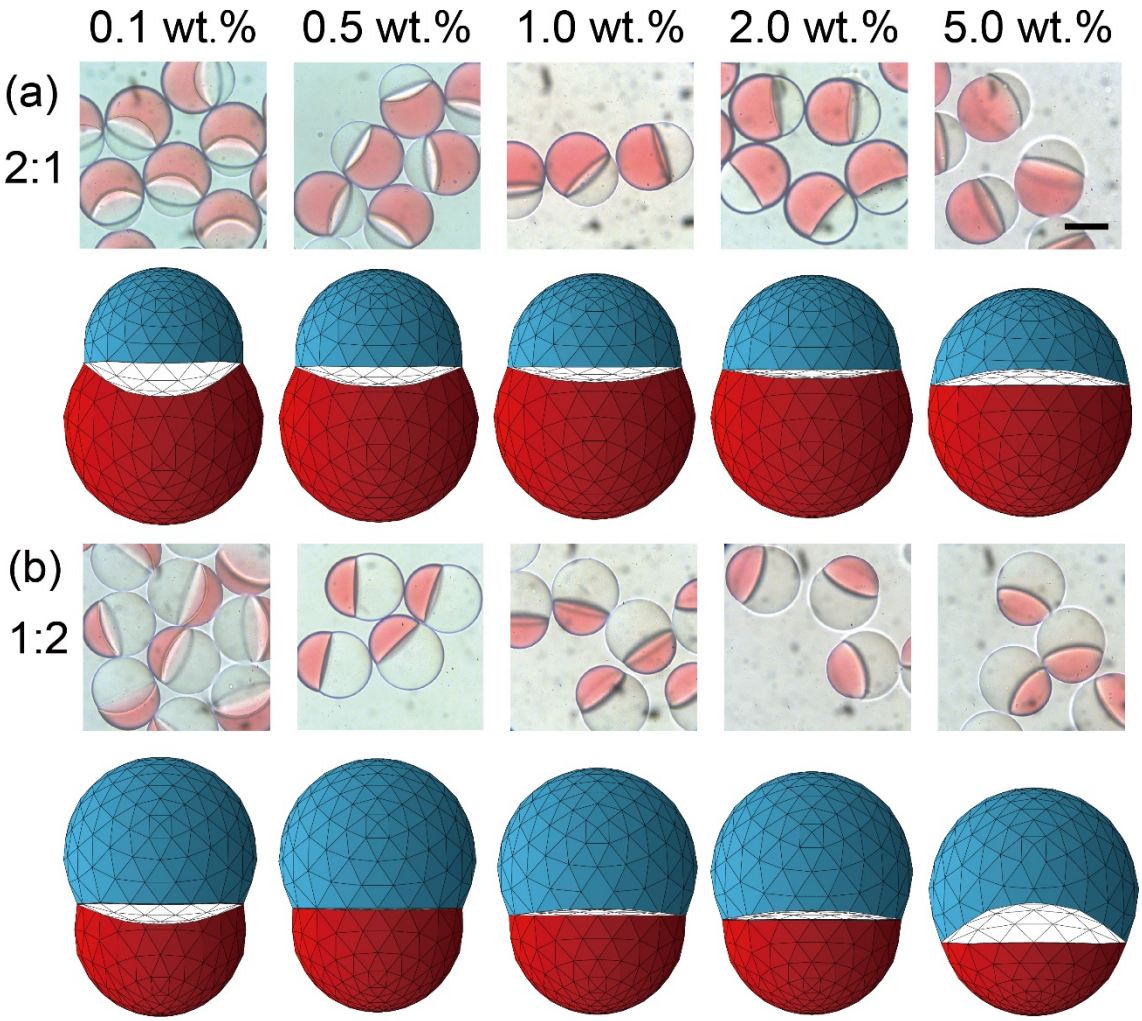

Figure 3.15 Morphology variation of Janus droplets with the concentration of surfactant in the SO segment ranging from 0.1 to 5.0 wt.% (top) and their corresponding 3D shapes (bottom) when (a) Q_m:Q_s = 2:1, and (b) Q_m:Q_s = 1:2. Droplets were produced at $Q_{d,\,total}$ = 0.6 mL h^{-1}, and Q_c = 8.0 mL h^{-1}. Scale bar: 100 μm.

To estimate the 3D morphology of the produced droplets, the interfacial tension values of γ_{31}, γ_{23}, and γ'_{12} at different surfactant concentrations were measured/calculated. As the

surfactant concentration increased from 0.1 wt.% to 5.0 wt.%, γ_{23} maintained a value of 1.1 mN m^{-1}, while γ_{31} decreased from 1.6 to 0.3 mN m^{-1}. By measuring the contact angles (α and β) of droplets generated at Q_m: Q_s = 1:1 with different surfactant concentration, the value of γ'_{12} was calculated (Table 3.2). The relation between surfactant concentration and interfacial tensions (γ_{31} and γ'_{12}) was shown in Fig. 3.16a. Based on the values of γ_{31}, γ_{23}, and γ'_{12}, morphologies of the produced droplets were estimated. The calculated results agreed well with the shape of the HDDA segments of the experimentally obtained droplets (Figs. 3.14 and 3.15).

Table 3.2 Relation between surfactant concentration and contact angles/interfacial tensions

Surfactant concentration	α	β	γ_{12} (mN m^{-1})	γ'_{12} (mN m^{-1})
0.1 wt.%	10°	36°	9.6	2.1
0.5 wt.%	8°	70°	8.6	1.3
1.0 wt.%	5°	75°	7.2	1.2
2.0 wt.%	2°	88°	5.4	1.1
5.0 wt.%	1°	120°	2.2	0.96

3.3.2.3 Phase diagram of biphasic droplets

To better understand the effect of surfactant concentration on the variation of Janus configurations, we plotted the conditions under different surfactant concentrations on a phase diagram, which can theoretically estimate the possible morphologies of a biphasic droplet based on the interfacial tensions [9, 25], including core-shell, Janus, and non-engulfing states (Fig. 3.16b). The white region in the middle of the diagram showed the region for Janus morphology. In this region, the biconvex HDDA and concave-convex SO segments form above the $Y = X$ line, and the concave-convex HDDA and biconvex SO segments form below the $Y = X$ line. Also, the HDDA/SO interface becomes planar if the condition is on the line of $Y = X$. As shown in Fig. 3.16b, all the experimental conditions (A–E) were located in the Janus region. For the conditions of A, B, and C, they fell in the region for the concave-convex HDDA segment, D nearly fell on the line of $Y = X$ for the planar HDDA/SO interface, and E fell in the biconvex HDDA region. These results agreed well with the experimental results (Fig. 3.14). Thus, we can understand the transition of droplet morphology when we vary the surfactant concentration in the SO segment.

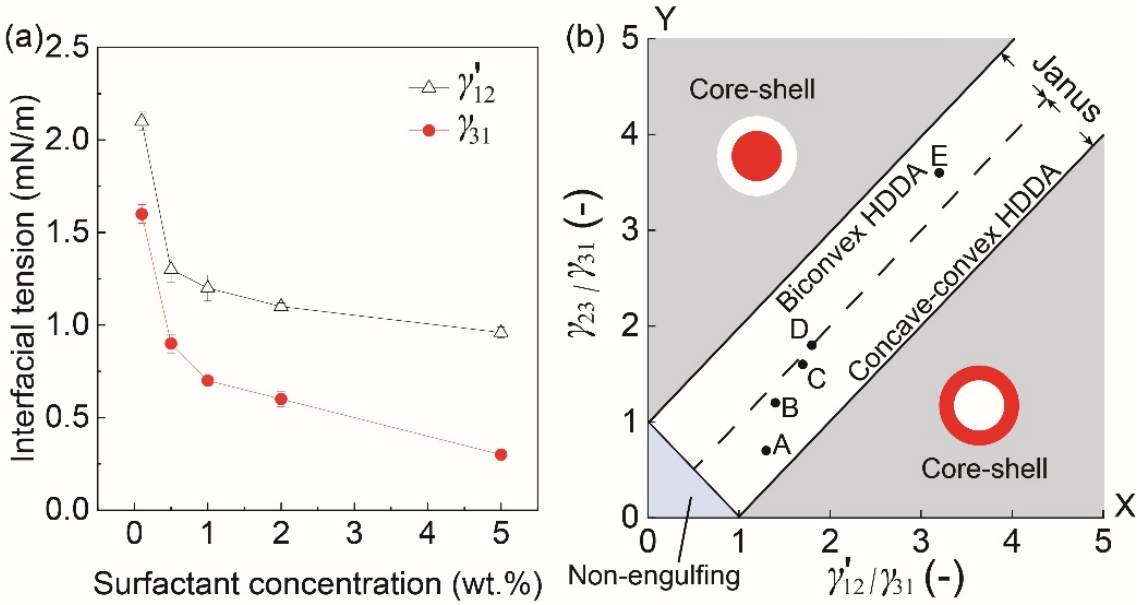

Figure 3.16 Interfacial energy and droplet morphology. (a) Interfacial tensions γ'_{12} and γ_{31} in response to surfactant concentration in the silicone oil; (b) A phase diagram showing the relation between the ratio of interfacial tensions γ'_{12}/γ_{31} and the morphologies of the biphasic droplets when $Q_m/Q_s = 1$. Solid circles with labels of A to E correspond to the droplets in Fig. 3.14.

3.3.3 Stability assessment of Janus droplets

3.3.3.1 Formation of surfactant-free Janus droplets in aqueous SDS solution

For comparison, we produced the surfactant-free biphasic droplets in the aqueous SDS solution at $Q_{d,\,total} = 0.6$ mL h^{-1} and $Q_c = 8.0$ mL h^{-1} (4.0 × 2 mL h^{-1}). As shown in Fig. 3.17a–c, by introducing HDDA and SO streams at Q_m: Q_s = 2:1, 1:1, and 1:2, biphasic droplets comprised of one HDDA segment and one SO segment could be produced continuously. The off-chip observation of the produced droplets confirmed that the surfactant-free biphasic droplets had a Janus geometry with a biconvex SO segment and concave-convex HDDA segment (Fig. 3.17d).

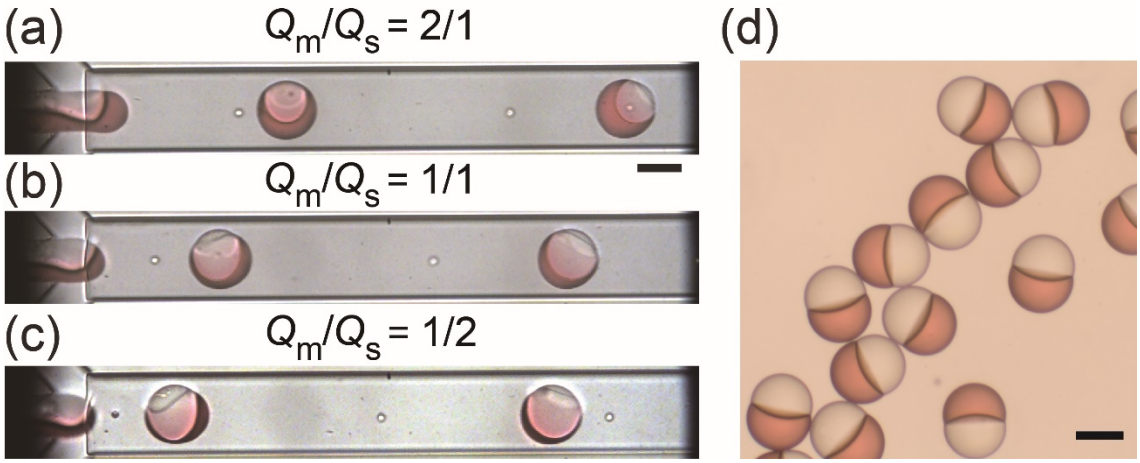

Figure 3.17 Surfactant-free Janus droplets in aqueous SDS solution. (a-c) Droplets generated at Q_m/Q_s of (a) 2/1, (b) 1/1 and (c) 1/2; (d) Photomicrograph of Janus droplets generated in (b). $Q_{d,\,total}$ = 0.6 mL h^{-1}, Q_c = 8.0 mL h^{-1}. Scale bars: 100 μm.

3.3.3.2 Surfactant-laden Janus droplets with improved stability against coalescence

Figure 3.18a shows the qualitative stability comparison results at Q_m/Q_s = 1/1. Immediately following the collection of the surfactant-free Janus droplets in the 0.3 wt.% aqueous SDS solution in a petri dish (at t = 0 s), the droplets floated at the air-water interface, maintaining their Janus morphology for a short period (t = 10 s). However, at t = 40 s, we observed that many Janus droplets were already lost, indicating their morphology rupture due to coalescence. In contrast, for the surfactant-laden Janus droplets in the aqueous PVA solution, no coalescence was observed at t = 40 s, suggesting better stability (Fig. 3.18a). We could confirm similar tendencies, by comparing the stability between surfactant-free and surfactant-laden Janus droplets generated at Q_m/Q_s = 2/1 and 1/2 (Fig. 3.18b,c).

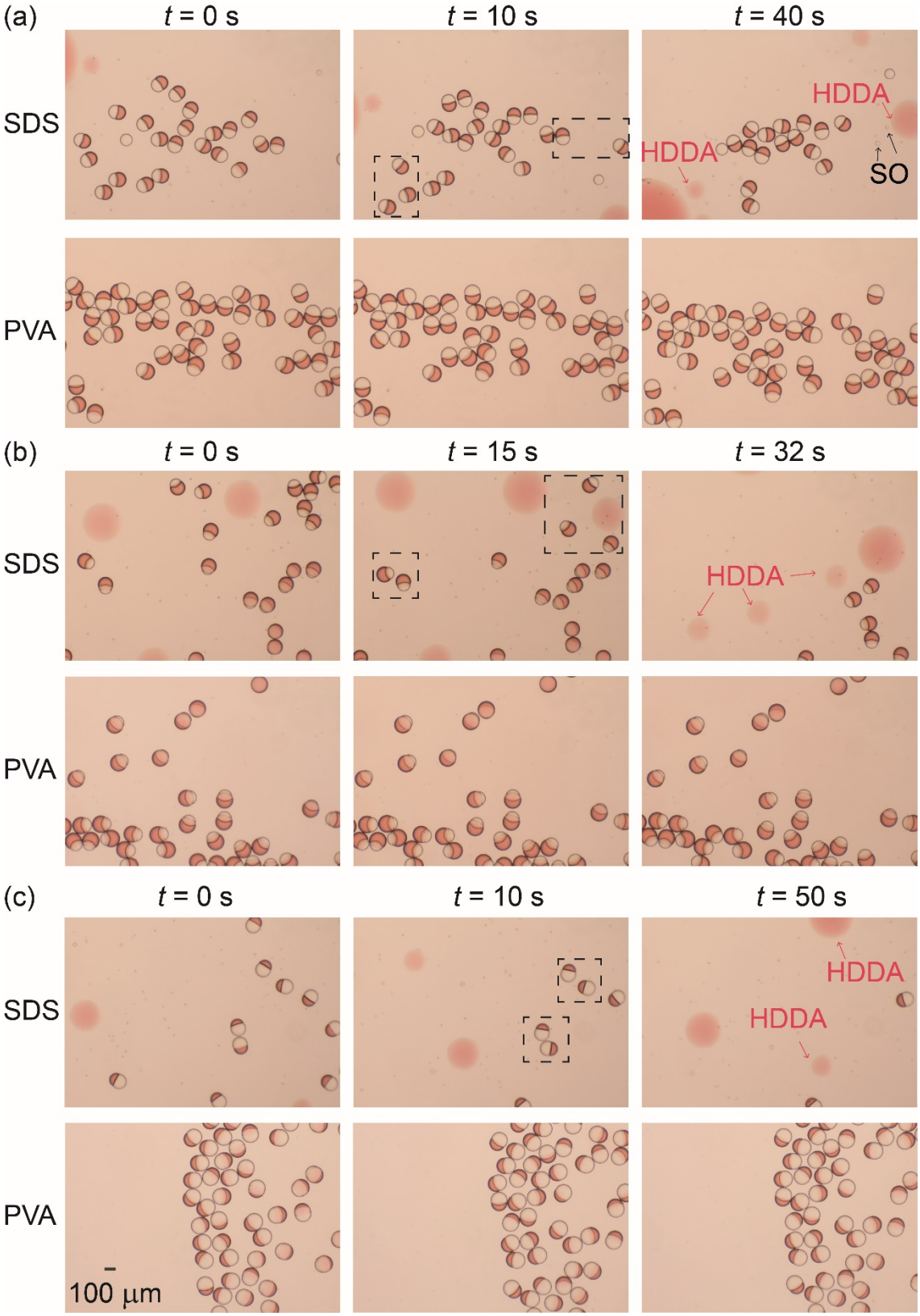
(a)
t = 0 s
t = 10 s
t = 40 s
SDS
HDDA
HDDA
SO
PVA
(b)
t = 0 s
t = 15 s
t = 32 s
SDS
HDDA
PVA
(c)
t = 0 s
t = 10 s
t = 50 s
SDS
HDDA
HDDA
PVA
100 μm

Figure 3.18 Comparison of off-chip stability between surfactant-free Janus droplets dispersed in the aqueous sodium dodecyl sulfate (SDS) solution (top) and surfactant-laden Janus droplets (0.1 wt.% in their silicone-oil segments) dispersed in the aqueous PVA solution (bottom) when (a) Q_m:Q_s = 1:1; (b) Q_m:Q_s = 2:1, and (c) Q_m:Q_s = 1:2. Droplets were produced at $Q_{d,\,total}$ = 0.6 mL h^{-1}, and Q_c = 8.0 mL h^{-1}.

To further investigate the stability of these Janus droplets, we increased observation time and counted the number of remaining Janus droplets over time (Fig. 3.19). The number of surfactant-free Janus droplets in the aqueous SDS solution rapidly decreased over time, and all of them ruptured within ~4 min. In contrast, for the surfactant-laden droplets in the aqueous PVA solution, no coalescence was observed for ~24 min, and it took ~176 min for all the droplets to lose their Janus morphology.

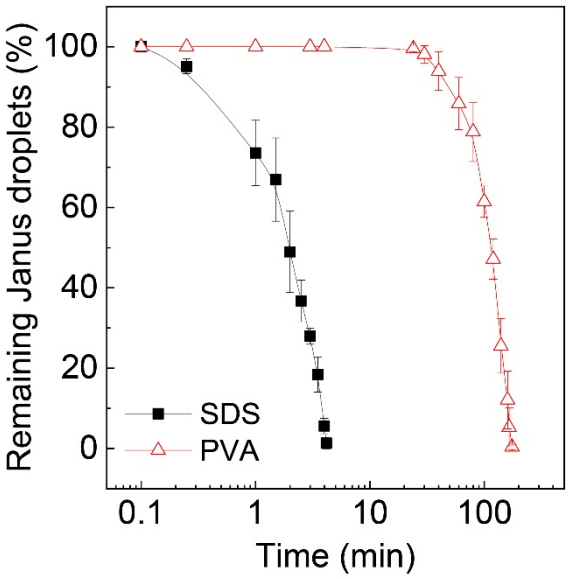

Figure 3.19 Decrease in Janus droplets by coalescence over time. Surfactant concentration in the SO phase of the Janus droplets in aqueous PVA solution is 0.1 wt.%. Droplets were produced at Q_m = Q_s = 0.3 mL h^{-1}, and Q_c = 8.0 mL h^{-1}. The error bars indicate the standard deviation of the measurements (n = 3).

This significantly enhanced stability of the surfactant-laden Janus droplets in the aqueous PVA solution might be attributed to the difference in molecular size between PVA

and SDS. The molecular size of PVA is much larger than that of SDS, thus causing steric hindrance to stabilize the droplets [26]. Also, this could be due to the decrease of the interfacial tensions at the dispersed phase/continuous phase interface [27]. For the Janus droplets in the aqueous SDS phase, the interfacial tensions were γ_{23} = 4.5 mN m^{-1} and γ'_{12} = 5.3 mN m^{-1} [8, 13]. Meanwhile, as described above, the SO containing the surfactant at 0.1 wt.% and the aqueous PVA solution caused a significant decrease of interfacial tension values (γ_{23} = 1.1 mN m^{-1} and γ'_{12} = 2.1 mN m^{-1}). Such a reduction in interfacial tension might also be responsible for the improved stability against coalescence. A previous study reported a similar phenomenon, where the addition of a surfactant (phosphatidylcholine) in the oil phase at a concentration of 3.0 wt.% decreased the interfacial tension at the oil/water interface to 0.5 mN m^{-1}, yielding more stable O/W Janus droplets with greater resistance to coalescence [28].

3.3.4 Fabrication and characterization of microlens-shaped particles

3.3.4.1 Microlens-shaped polymer particles via photopolymerization

Polymer particles of various lens shapes were fabricated from the surfactant-laden Janus droplets by photopolymerization. The bright-field image of the solidified particles in the aqueous PVA solution confirmed that the HDDA segment in the surfactant-laden Janus droplets was polymerized into particles (Fig. 3.20). As shown in Fig. 3.21, we confirmed that the shapes of the fabricated particles were concave-convex, planar-convex, or biconvex based on the concentration of the surfactant in the SO phase, consistent with the shape of the curable HDDA segment in the precursor Janus droplets. The concave-convex particles with different curvature radii of the concave surface could be obtained from the precursor droplets carrying the surfactant at lower concentrations (i.e., 0.1, 0.5, and 1.0 wt.%), where the particles with lower surfactant concentrations had more concave surfaces. On the other hand, the surfactant concentrations of 2.0 and 5.0 wt.% yielded planar-convex (i.e., hemispherical) and biconvex particles, respectively.

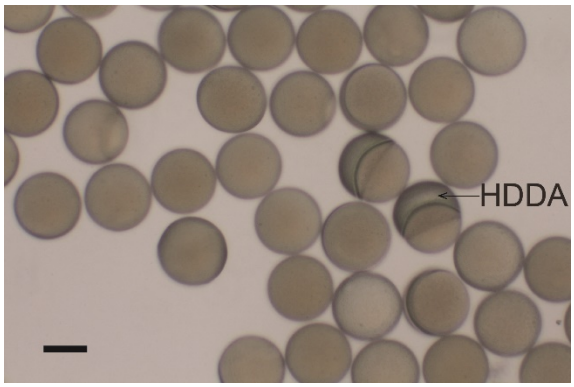

Figure 3.20 Bright-field image of the photopolymerized particles in the aqueous PVA solution with the concentration of surfactant in SO phase at 0.1 wt.%. $Q_m = Q_s = 0.3$ mL h^{-1}, and $Q_c = 8.0$ mL h^{-1}. Scale bar: 100 μm.

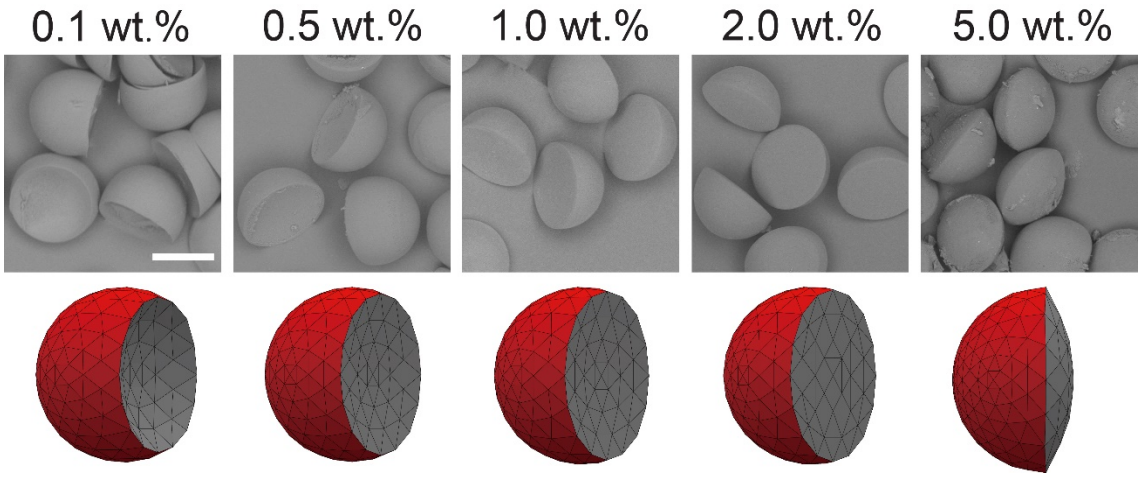

Figure 3.21 SEM images of concave-convex, planar-convex, and biconvex particles (top), and their simulated 3D models (bottom) prepared at different surfactant concentrations in silicone oil segments. Precursor Janus droplets were produced at $Q_m = Q_s = 0.3$ mL h^{-1}, and $Q_c = 8.0$ mL h^{-1}. Scale bar: 100 μm.

We confirmed similar shape variation from concave-convex to biconvex, by photopolymerizing droplets produced at Q_m/Q_s = 1/2 and 2/1, although the surfactant concentration for the transition of the inner curvature between concave and convex surfaces was different. The inner curvature of droplets shifted at the surfactant concentration of 1.0 wt.% for $Q_m/Q_s = 1/2$, and 5.0 wt.% for $Q_m/Q_s = 2/1$. All the shapes of the particles agreed

well with the shape of the HDDA segments in the precursor droplets as well as the estimated models (Fig. 3.22).

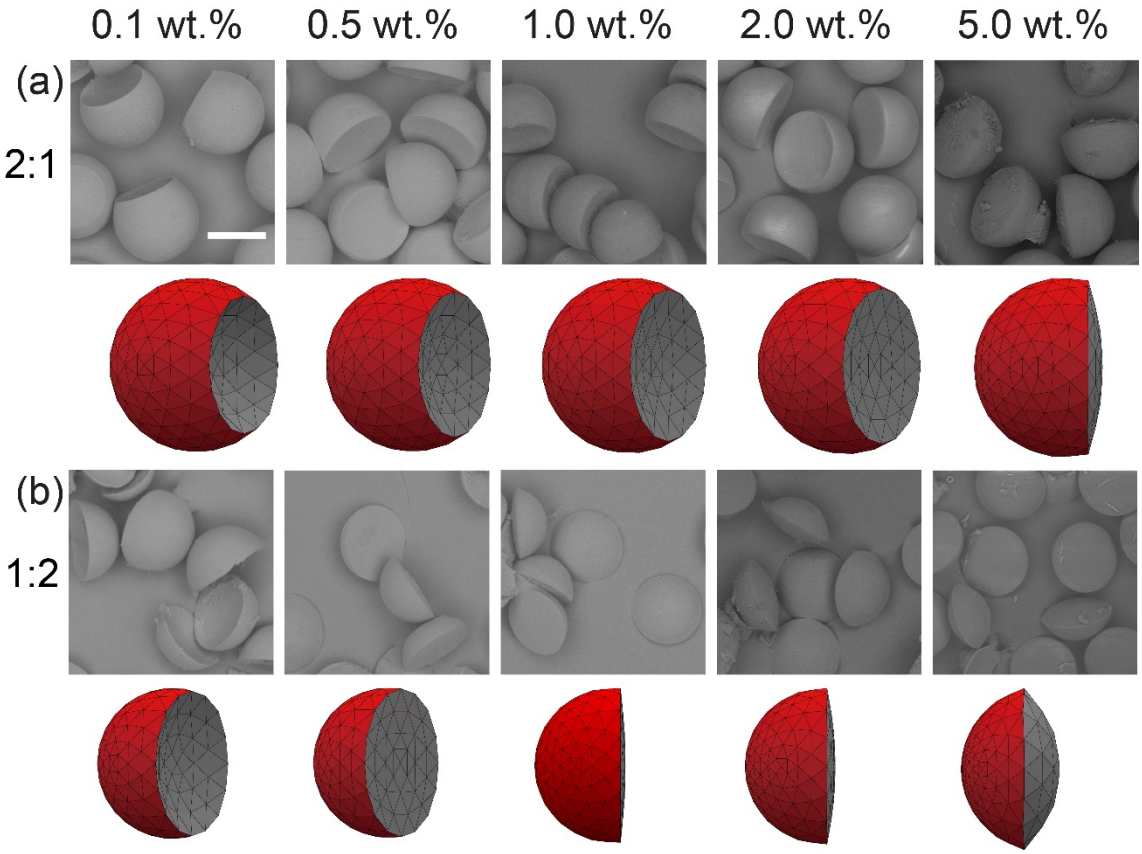

Figure 3.22 Lens-shaped polymer particles (top) and their Surface Evolver models (bottom) prepared at different surfactant concentrations and flow-rate ratios. (a) Convex-concave and biconvex particles templated from the Janus droplets produced at Q_m/Q_s of 2/1; (b) Convex-concave and biconvex particles templated from the Janus droplets produced at Q_m/Q_s of 1/2. The concentration of surfactant in the SO phase ranged from 0.1 to 5.0 wt.%. $Q_{d,\,total}$ = 0.6 mL h^{-1}, and Q_c = 8.0 mL h^{-1}. Scale bar: 100 μm.

3.3.4.2 Microlens-shaped polymer particles via thermally polymerization

We next attempted to fabricate polymer particles via thermal polymerization. In this case, the surfactant-laden Janus droplets with the surfactant concentration of 1.0 wt.% generated at Q_m/Q_s ratios of 2/1, 1/1, and 1/2 were used as templates. Similar to the photopolymerization approach, the bright-field image of the solidified particles confirmed

that HDDA segments in the surfactant-laden Janus droplets were thermally-polymerized into particles (Fig. 3.23).

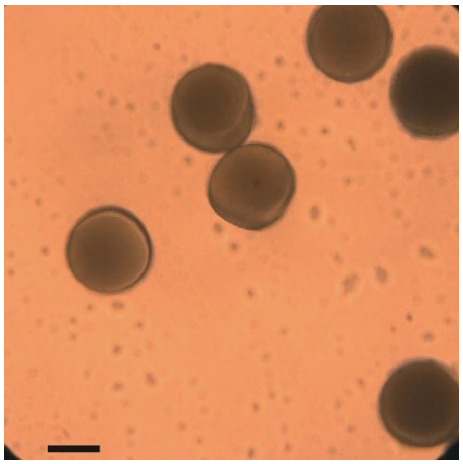

Figure 3.23 Bright-field image of thermally-polymerized particles in the aqueous PVA solution with the concentration of surfactant in the SO phase at 1.0 wt.%. $Q_m = Q_s = 0.3$ mL h^{-1}, and $Q_c = 8.0$ mL h^{-1}. Scale bar: 100 μm.

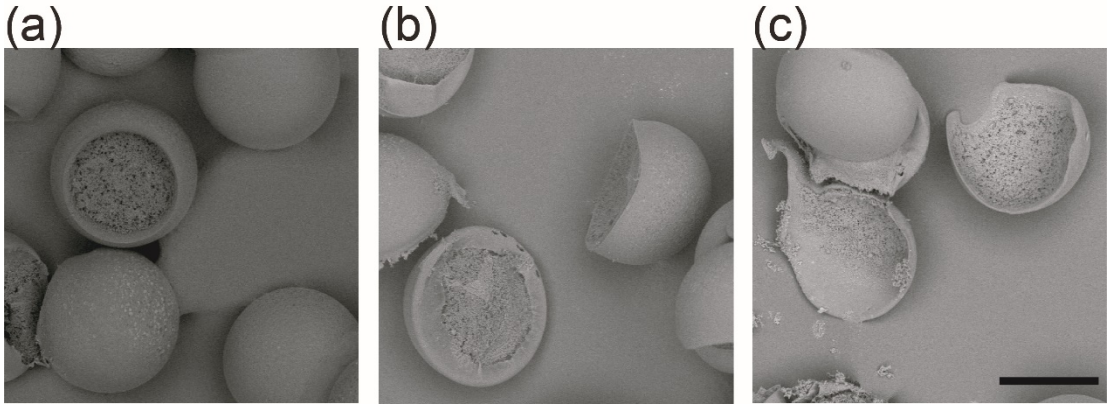

Figure 3.24 Thermally-polymerized polymer particles prepared with surfactant concentrations 1.0 wt%. (a-c) Particles fabricated at (a) Q_m:Q_s = 2:1; (b) Q_m:Q_s = 1:1 and (c) Q_m:Q_s = 1:2. $Q_{d,\,total} = 0.6$ mL h^{-1}, $Q_c = 8.0$ mL h^{-1}. Scale bar: 100 μm.

The SEM observation of the thermally cross-linked particles revealed that the fabricated particles reflected the shape of the curable HDDA segment in the precursor Janus droplets, resulting in the concave-convex and biconvex polymer particles (Fig. 3.24). However, unlike the particles having two smooth surfaces via photopolymerization, the

former HDDA/SO interface of the thermally-cured particles were rough and non-spherical, although the former HDDA/water interface was relatively smooth and spherical. One possible reason for this turbulent condition in the bath for the thermal polymerization. Another possible reason is because the production of nitrogen gas via Nitrogen−Nitrogen double bond cleavage of the initiator V-65 in the HDDA segment. The accumulation and release of the produced nitrogen bubbles might cause the formation of pores and deformation in the polymerized segment.

We believe that the enhanced stability of the surfactant-laden Janus droplets will be useful for industrial-scale fabrication of polymer particles via photo-induced or thermally-induced polymerization. In particular, the enhanced stability will be effective for thermal polymerization that needs a longer time for completion.

3.3.4.3 Advantages of the presented surfactant-laden Janus droplets

For the first time, we produced the surfactant-laden Janus droplets in an aqueous PVA solution at equilibrium. We believe that the present surfactant-laden Janus droplets are more suitable for fabricating templated particles owing to the advantages of significantly improved stability against coalescence and resultant high yielding efficiency.

Besides, for the first time, we revealed that the Janus morphology and resultant particle shapes could be altered simply by changing the surfactant concentrations in the non-curable phase, in addition to tuning the flow-rate ratios of the two disperse phases. We believe that the presented approach holding the advantage of fabricating novel particulate materials with precisely designed curvatures.

3.4 Summary

In this chapter, we described the surfactant-laden Janus droplets comprised of two immiscible curable and non-curable segments with high stability against coalescence and tunable morphologies, suitable for the fabrication of lens-shaped microparticles. The contents of each section are summarized below.

In the **Introduction** section 3.1, the limitations of the conventional method for preparing Janus droplets, as well as the advantages of microfluidic technology for

producing monodisperse Janus droplets were described. Furthermore, the approach to control the size/shape of the microfluidic Janus droplets was described, which led to the motivation of the present study.

In the **Materials and experimental methods** section 3.2, the microfluidic device, the materials for generating Janus droplets, methods for fabricating polymer particles, and the peripheral equipment for experiment and characterization were introduced.

Results and discussion section 3.3 is summarized below:

3.3.1 Formation of surfactant-laden droplets. We confirmed that the monodisperse Janus droplets of an acrylate monomer and SO containing surfactant could be produced in an aqueous PVA solution in a microfluidic Janus droplet generator.

3.3.2 Effect of inner surfactant concentration on Janus morphology. We could vary the curvature radii of the interface separating the two Janus lobes by adjusting the concentration of the loaded surfactant.

3.3.3 Stability assessment of Janus droplets. The produced surfactant-laden Janus droplets in the aqueous PVA sotluion had considerably higher stability against coalescence than the surfactant-free Janus droplets in the aqueous SDS solution

3.3.4 Fabrication and characterization of microlens-shaped particles. The concave-convex, planar-convex, and biconvex particles were fabricated via photo- or thermally-induced polymerization of surfactant-laden droplets, which provides a new route for fabricating novel particulate materials with precisely designed curvatures.

3.5 References

[1] Li, X.; Yang, Y. T.; Wu, L. J.; Li, Y. C.; Ye, M. Y.; Chang, Z. Q.; Meng, D. Q.; Serra, C. A. *Mater. Lett.* 42, 258 (2015).

[2] Varma, V. B.; Wu, R. G.; Wang, Z. P.; Ramanujan, R. V. *Lab Chip* 17, 3514 (2017).

[3] Xu, K.; Ge, X. H.; Huang, J. P.; Dang, Z. X.; Xu, J. H.; Luo, G. S. *RSC Adv.* 5, 46981 (2015).

[4] Gröschel, A. H.; Walther, A.; Löbling, T. I.; Schmelz, J.; Hanisch, A.; Schmalz, H.; Müller, A. H. E. *J. Am. Chem. Soc.* 134, 13850 (2012).

[5] Hasinovic, H.; Friberg, S. E. *Langmuir* 27, 6584 (2011).

[6] Nisisako, T. *Colloid Interface Sci.* 25, 1 (2016).

[7] Nisisako, T.; Torii, T.; Takahashi, T.; Takizawa, Y. *Adv. Mater.* 18, 1152 (2006).

[8] Nisisako, T.; Torii, T. *Adv. Mater.* 19, 1489 (2007).

[9] Nisisako, T.; Ando, T.; Hatsuzawa, T. *J. Jpn. Soc. Precis. Eng.* 79, 460 (2013).

[10] Nisisako, T.; Ando, T.; Hatsuzawa, T. *Small* 10, 5116 (2014).

[11] Nisisako, T.; Suzuki, H.; Hatsuzawa, T. *Micromachines* 6, 1435 (2015).

[12] Jeong, J.; Gross, A.; Wei, W. S.; Tu, F.; Lee, D.; Collings, P. J.; Yodh, A. G. *Soft Matter* 11, 6747 (2015).

[13] Nisisako, T.; Hatsuzawa, T. *Microfluid. Nanofluid.* 9, 427 (2010).

[14] Yang, Y. T.; Wei, J.; Li, X.; Wu, L. J.; Chang, Z. Q.; Serra, C. A. *Adv. Powder Technol.* 26, 156 (2015).

[15] Seo, K. D.; Doh, J.; Kim, D. S. *Langmuir* 29, 15137 (2013).

[16] Kim, S. H.; Abbaspourrad, A.; Weitz, D. A. *J. Am. Chem. Soc.* 133, 5516 (2011).

[17] Torza, S.; Mason, S. G. *Science* 163, 813 (1969).

[18] Kang, Z.; Kong, T.; Lei, L.; Zhu, P.; Tian, X.; Wang, L. *J. Micromech. Microeng.* 26, 075011 (2016).

[19] Ge, X.; Geng, Y.; Zhang, Q.; Shao, M.; Chen, J.; Luo, G.; Xu, J. *Sci. Rep.* 7, 42738 (2017).

[20] Zarzar, L. D.; Sresht, V.; Sletten, E. M.; Kalow, J. A.; Blankschtein, D.; Swager, T. M. *Nature* 518, 520 (2015).

[21] Nisisako, T.; Hatsuzawa, T. *Sens. Actuators B Chem.* 223, 209 (2016).

[22] Xu, S.; Nisisako, T. *Sci. Rep.* 10, 4549 (2020).

[23] Brakke, K. *Exp. Math.* 1, 141 (1992).

[24] Hui C.Y.; Jagota, A. *Soft Matter* 11, 8960 (2015).

[25] Guzowski, J.; Korczyk, P. M.; Jakiela, S.; Garstecki, P. *Soft Matter* 8, 7269 (2012).

[26] Baret, J. C. *Lab Chip* 12, 422 (2012).

[27] Raju, R. R.; Kosmella, S.; Friberg, S. E.; Koetz, J. *Colloids Surf. A* 533, 241 (2017).

[28] Kovach, I.; Koetz, J.; Friberg, S. E. *Colloids Surf. A* 441, 66 (2014).

[29] Malloggi, F.; Pannacci, N.; Attia, R.; Monti, F.; Mary, P.; Willaime, H.; Poncet, P. *Langmuir* 26, 2369 (2010).

[30] Hwang, D. K.; Dendukuri, D.; Doyle, P. S. *Lab Chip* 8, 1640 (2008).

[31] Nisisako, T.; Ando, T.; Hatsuzawa, T. *Lab Chip* 12, 3426 (2012).

[32] Lan, W.; Du, Y.; Guo, X.; Liu, A.; Jing, S.; Li, S. *Ind. Eng. Chem. Res.* 57, 212 (2017).

Chapter 4

Microfluidic formation of ternary emulsion droplets

未公表部

Chapter 5

W/O/W double emulsions produced in PDMS microfluidic devices

未公表部

Chapter 6

Parallelized microfluidic channels for generating biphasic droplets

未公表部

Chapter 7

Conclusion and outlook

7.1 Conclusion

Chapter 1 Introduction

Conventional emulsification methods and recent droplet-based microfluidic technology for making biphasic droplets (i.e., double emulsions and Janus droplets) were introduced. Then, the main objectives to carry out the studies in Chapter 2 to 6 in this thesis was described.

Chapter 2 Janus to core-shell transition of microfluidic biphasic droplets

Formation of Janus droplets and their subsequent Janus-to-core-shell structural evolution was applied to the fabrication of oil-filled polymer microcapsules with tunable shell thickness. The main contributions and novelties are summarized as follows:

(1) Formation of biphasic Janus droplets and their interfacial-energy-driven Janus-to-core-shell evolution was demonstrated, for the first time in a flow-focusing Janus droplet generator.

(2) The oil-filled polymer microcapsules with ultra-thin shell thickness could be fabricated from core-shell droplets via photo-and thermally induced polymerization, by increasing photo- and thermal initiator concentration.

(3) Compare to the photopolymerized capsules with smooth surfaces, the thermally polymerized polymer microcapsules had a porous surface morphology.

Chapter 3 Microfluidic formation of surfactant-laden Janus droplets

The formation of surfactant-laden Janus droplets with curvature controllability and enhanced stability against coalescence was studied. The main contributions and novelties are summarized as follows:

(1) Biphasic droplets, comprising an acrylate monomer segment and a silicone oil segment containing a surfactant, were produced in a co-flowing aqueous PVA solution. We found, for the first time, that the biphasic droplets comprising an acrylate monomer and a silicone oil segment containing a surfactant in the aqueous PVA solution formed a Janus geometry at equilibrium.

(2) By varying the concentration of the surfactant in the silicone oil phase, the curvature of the interface between the two lobes could be shifted among concave, planar, and convex shapes.

(3) The produced surfactant-laden Janus droplets had considerably higher stability against coalescence than the surfactant-free Janus droplets in the aqueous SDS solution.

(4) The concave-convex, planar-convex, and biconvex lens-shaped particles were fabricated via off-chip photopolymerization.

Chapter 4 Microfluidic formation of ternary emulsion droplets

Chapter 5 W/O/W double emulsions produced in a PDMS microfluidic device

未公表部

Chapter 6 Parallelized microfluidic channels for generating biphasic droplets

未公表部

7.2 Outlook

7.2.1 High throughput production of biphasic droplets

The parallelized microfluidic device for the scale-up production of core-shell droplets and Janus droplets was described in Chapter 6. Based on this approach, it will be possible to arrange more PDMS microfluidic channels in parallel on a single chip for further high throughput production of biphasic droplets to meet the industrial-scale prodution, which is supposed to be achieved by enlarging the size of the PDMS chip and the stainless-steel module at the same time, or numbering-up of the modules.

In Chapter 5, the formation of W/O/W double emulsions using a single PDMS-based microfluidic device was demonstrated. The parallelized microfluidic device in this thesis might also be applicable for W/O/W double emulsions in parallel if localized hydrophilic surface modification is combined.

7.2.2 Microfluidic nanoscale droplets and particles

The microfluidic systems for droplet formation on a micrometer scale were demonstrated in this thesis. On the other hand, the droplet formation in a smaller dimension such as nanoscale has attracted much attention recently. Therefore, it will be worth discussing the formation of nanoscale biphasic in the future, by fabricating microfluidic devices with nanoscale channels.

Appendix

A.1 Glass-based microfluidic device

The microfluidic droplets in Chapter 2 to Chapter 4 were generated through microgrooves fabricated on a planer glass chip (Fig. A.1 and Table A.1). To infuse fluidic phases, the prepared glass chip was assembled with a stainless-steel holder that comprised a supporting layer and a cover with a square-hole (Fig. A.2).

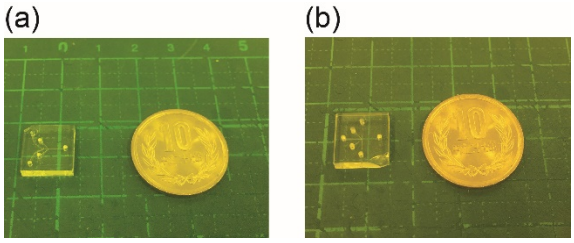

Figure A.1 Microgrooves fabricated on the planer glass chips for generating (a) core-shell or Janus droplets and (b) ternary emulsion droplets.

Table A.1 Planer glass chips

Function	Size (mm^3)	Number of inlets
Core-shell or Janus droplets formation	15 × 15 × 3.5	Four inlets
Ternary emulsion droplets formation	12 × 12 × 3.5	Five inlets

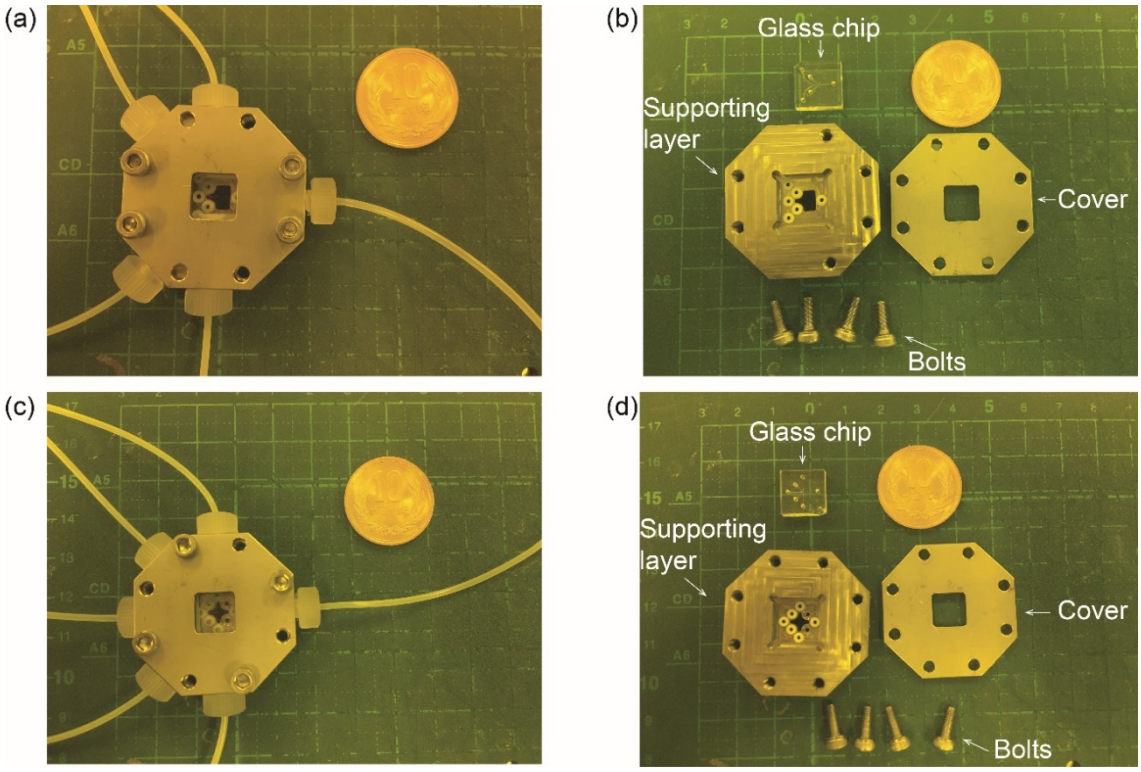

Figure A.2 Planer glass chips assembled with a stainless-steel holder. (a-b) Microfluidic device for generating biphasic droplets. (a) The assembled device; (b) Modules for assembling. (c-d) Microgrooves fabricated on the planer glass chips for generating (b) core-shell and Janus droplets and (b) ternary emulsion droplets.

A.2 Fabrication of PDMS microfluidic device

In Chapter 5 and Chapter 6, we used conventional soft lithography technique to fabricate PDMS microfluidic device [1]. In this technology, the micro-nano structures are fabricated by transferring the structure of the mold to elastomeric materials such as PDMS. One obvious advantage is that once the mold is prepared, it is possible to easily manufacture a silicone resin substrate to which the fine structure is transferred.

Following the introduction above, our microfluidic device fabricated by conventional soft lithography techniques are mainly divided in 7 steps: (1) Soft bake with the coating of the photoresist on a silicon wafer, (2) UV light exposure, (3) Post exposure bake, (4) Development, (5) PDMS casting, (6) PDMS mold release and (7) Assembly. The schematic of the PDMS microchannel fabrication process in shown in Fig. A.3

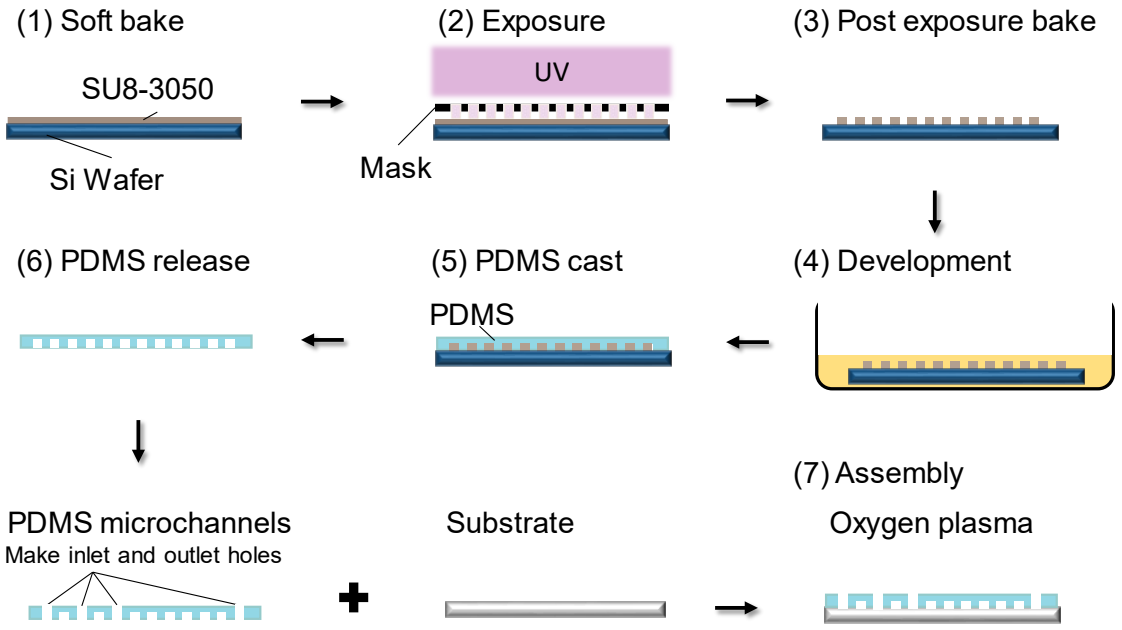

Figure A.3 Fabrication process of PDMS microfluidic device.

(1) Soft Bake

Prior to soft bake, the silicon wafer (diameter 76±0.5 mm, thickness 380±20 μm) was cleaned in ultrasonic machine (US-2, iuchi) using acetone, ethanol and deionized water for 5 min, respectively, and dried on hotplate (HP-2SA, AS ONE, JAPAN). Then after the plasma treatment at 50W for 3 min, the silicon wafer was ready for soft bake. For soft bake, we coated a layer of the negative photoresist SU-8 3050 (MicroChem) on the silicon wafer. To obtain the desired channel thickness (100 μm here), the spin coater (1H-D7, MIKASA, JAPAN) was used for uniformly spreading photoresist at 500 rpm for 10s, and 1400 rpm for 30s. Finally, the silicon wafer was placed on a hotplate at respectively 65°C for 5 minutes and 95°C for 40 minutes to cure the photoresist.

(2) Exposure

Prior to exposure, the Quartz glass mask (thickness: 0.175mm, resolution: 25400dpi, UnnoGiken) with designed geometry was placed in close contact to the cured photoresist. Then, using a mask aligner (MA-10, Mikasa, Japan), we exposed them to UV light. The exposure time is based on the UV light power.

(3) Post Exposure bake

After removing the silicon wafer from the mask aligner, it was placed on a hotplate and baked respectively for 1 minute at 65°C and 15 minutes at 95°C to promote the degree of cross-linking of the photoresist, so that they are stable later in the developer.

(3) Development

Firstly, we prepared a petri dish (3140-90, PYREX, GERMANY), poured the SU-8 Developer solution (MicroChem) and placed the silicon wafer inside it. Secondly, the petri dish was put on a shaker (Wave-SIslim, TITEC) for 10 min to wash out the remaining photoresist on the silicon wafer. Thirdly, we sprayed/washed the developed wafer with Isopropyl Alcohol (IPA) for 10 seconds. Then, after drying it with pressurized air, the silicon wafer was baked at 120°C on a hot plate for 5 minutes to further cross link the material.

(5) PDMS Cast

Here, The PDMS pre-polymer (Dow Corning, TORAY, Tokyo, JAPAN) and Sylgard 184 (Dow Corning, TORAY, Tokyo, JAPAN) was mixed in a ratio of 10:1 w/w. Next, the fabricated SU-8 mold was fixed on a polymeric petri dish with Kapton tape. To hydrophobize its surface, Chlorotrimethylsilane (0.5 mL; Tokyo Chemical Industry Co., Ltd., JAPAN) was dropped around the SU-8 mold and allowed to stand for 10 minutes. Then, it was placed and heated on a hotplate for 5 minutes at 120 °C. Finally, the prepared mixture of PDMS was poured on the top of the patterned silicon wafer in the polymeric petri dish.

(6) PDMS release

The petri dish was placed inside a degas machine (AS ONE, JAPAN) until all air bubbles in the PDMS mixture was removed. Then, the petri dish was hardened on a hotplate at 90°C for 1 hour. The hardened PDMS was then release to obtained our PDMS microchannels.

(7) Assembly

Following the release of the PDMS from the petri dish, inlets and outlet holes were punched in the PDMS microchannels. To assemble the PDMS microchannels for experiment, the PDMS microchannels was bonded to the glass or PDMS substrate through Oxygen plasma treatment (BP-1, SAMCO, JAPAN) at 20W for 30 second. Finally, the

assembled module was heated on the hotplate for 1 hour at 85℃, obtaining the PDMS microfluidic device.

A.3 Experiment setup and peripheral equipment

In this thesis, the main experiment platform is setup in the following Figure A.4, which consists of (1) Microfluidic device; (2) Observation and characterization instrument; (3) Infusing system and (4) Others. The (2) to (4) parts are described as below:

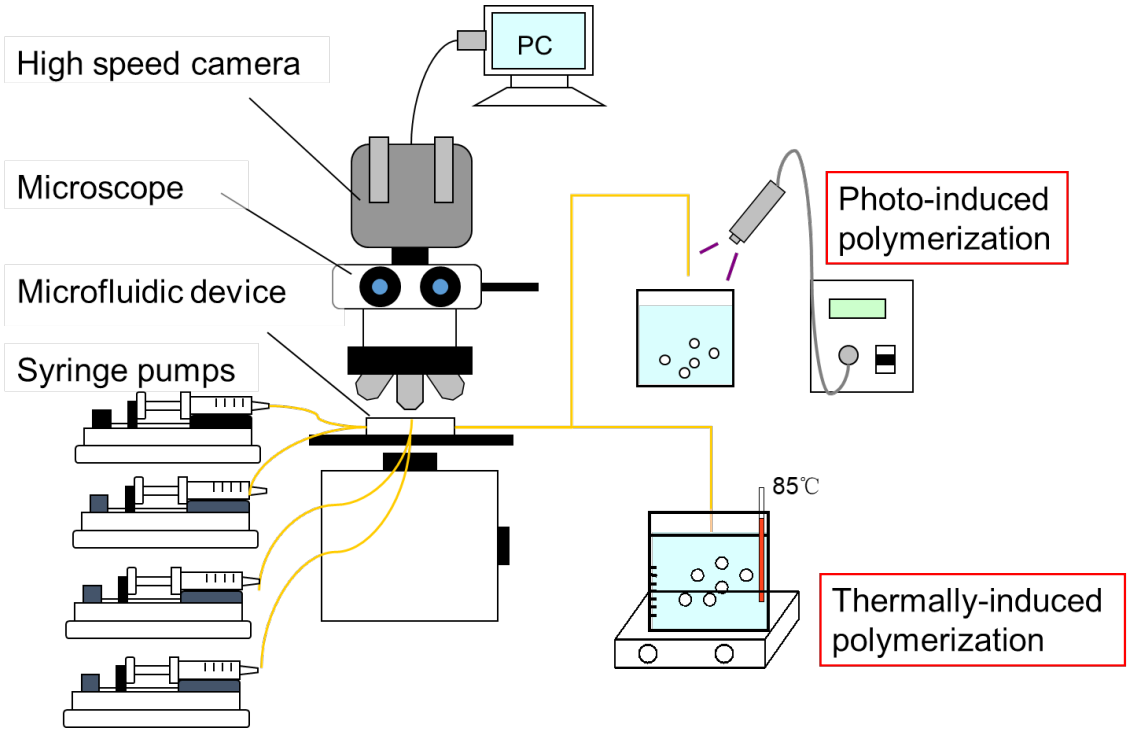

Figure A.4 Experiment platform

(1) Microfluidic device

The detail of the microfluidic device was introduced in A.1.

(2) Observation and characterization instrument

(a) Optical microscope

The upright optical microscope (BX-51, Olympus, Tokyo, Japan) was used for observation (Fig. A.5).

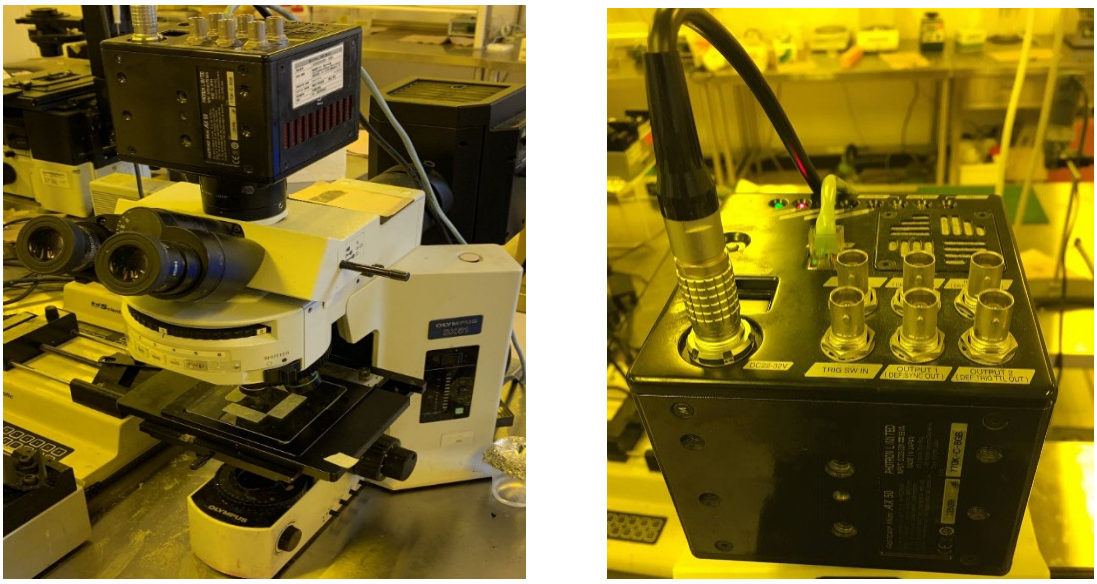

Figure A.5 The optical microscope (left) assembled with a high-speed video camera (right)

(b) High-speed carema

The high-speed video camera (Fastcam Mini AX50, Photron, Tokyo, Japan) was mounted on the optical microscope for observation in real-time (Fig. A.5).

(c) Scanning electron microscope

Scanning electron microscope (SEM, JSM-6610LA, JEOL, Tokyo, Japan) was used to observe the structure of microchannel and polymer particles (Fig. A.6).

Fig. A.6 Scanning electron microscope

(3) Infusing system

(a) Glass syringes

Glass syringes (1000 series, Hamilton Company, NV, USA) were used for infusing fluidic phases into microfluidic devices. For single microfluidic device, we used two syringe types with total volume of 1 ml and 10ml with luer-lock adaptor. We used syringe of 1 ml volume type to infuse the disperse phase and 10 ml volume type to infuse the continuous. For parallelized microfluidic device, both continuous phase and disperse phases were introduced into device by using 10 ml volume type (Fig. A.7).

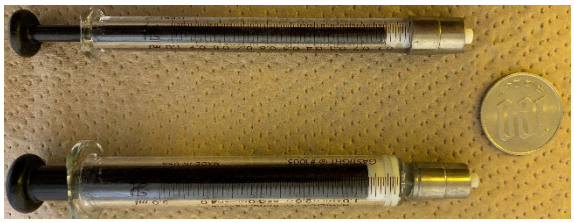

Figure A.7 Glass syringes of total volume 1 ml (top) and 10 ml (bottom)

(b) Syringe pumps

Syringe pumps (KDS 200, KD Scientific Inc., PA, USA) were used to infuse the fluidic phases in the glass syringes. The parameters are shown in the Table A. 2.

Table A.2 Parameters of syringe pumps

Parameter	KDS 200
Pump type	Push
Syringes	10 μL ~ 140 mL
Dimensions	28 × 23 × 15 cm
Weight	4 kg
Power	176 N (18 kgf)
Max. step rate	800 step/sec
Min. step rate	1 /100 secs
Accuracy	±1 %
Reproducibility	±0.1 %
Max. flow rate	8824 mL/h (140 mL syringe)
Min. flow rate	0.001 μL/h (10 μL syringe)

(c) PTFE tube

The (Poly Tetra Fluoro Ethylene (PTFE) connectors and tubes (outer diameter of 1.5mm) were used to transport liquid phases and products. The connector (screw size: No. 10-32UNF and 1/4-28UNF) used for linking supporting holder, and the connectors with luer-lock adaptor were used for linking the syringes (Fig. A.8).

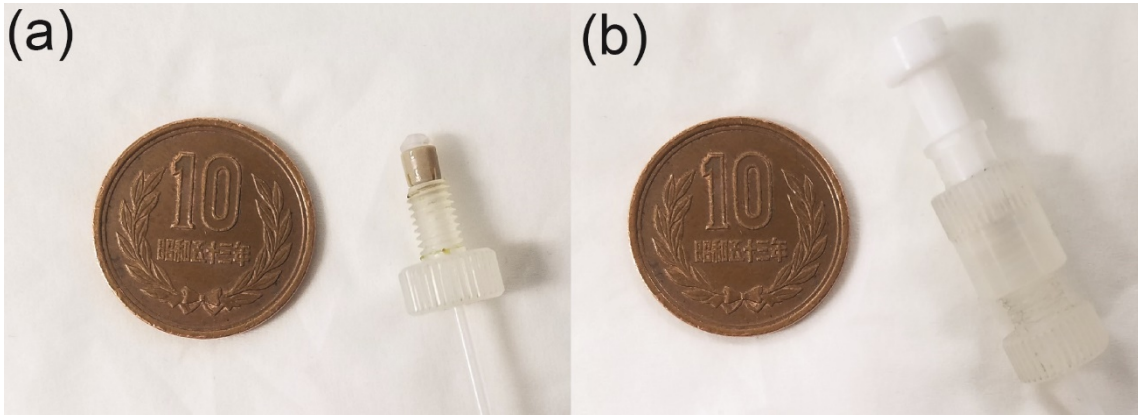

Figure. A.8 HPLC connectors in PTFE tubes for connecting the (a) holder and (b) syringes.

(4) Others

(a) Ultra-violet (UV) light source

To fabricate polymer particles using photo-induced polymerization, the collected droplets were exposed to a ultra-violet (UV) light source (LA-410UV, Hayashi-repic, Tokyo, Japan) continuously with the irradiation distance about 15–20 cm (Fig. A.9).

Figure A.9 The UV light source (left) and its head section (right) for photo-induced polymerization

(b) Ceramic hot stirrer

To fabricate polymer particles using thermally-induced polymerization, the collected droplets were heating to 80–85℃ using a ceramic hot stirrer (CHPS-170DN, AS ONE corporation, Tokyo, Japan), as shown in Fig. A.10.

Figure A.10 The ceramic hot stirrer for thermally-induced polymerization

(c) Filter

A nylon mesh (42 μm × 42 μm, Tokyo Screen, Tokyo, Japan) was put in a glass mesh holder (Glass Type KG-25, ADVANTEC, Japan) for removing smaller satellite particles through filtering (Fig. A.11).

Figure A.11 Images of filter device with each part (left) and assemble (right)

(d) Interfacial tension measure instrument

The interfacial tensions among the fluidic phases were measured using the interfacial tension measurement instrument based on the pendant-drop method (B100, Asumi Giken, Tokyo, Japan), as shown in Fig. A12.

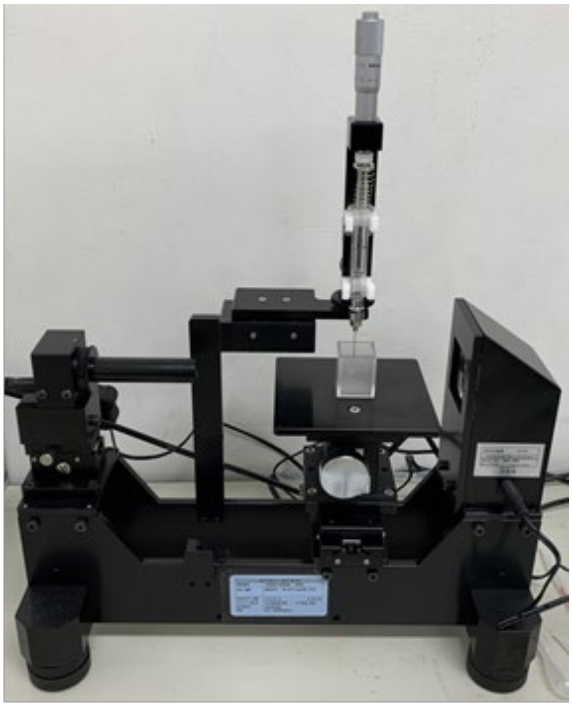

Figure A.12 Interfacial tension measurement instrument

A.4 Reference

[1] Duffy, D. C.; McDonald, J. C.; Schueller, O. J. A.; Whitesides, G.M. *Anal. Chem.* 80, 4974 (1998).

Acknowledgment

First and foremost, I want to thank my academic supervisor Professor Nisisako Takasi, who provided me many precious opportunities and constant support during my Ph.D. I believe that this thesis could not have reached its present form without his enlightening instruction and encouragement. I learned a lot from him such as what basic skills should be necessary as a researcher, what should be important in academic research. In addition, I am grateful for giving me valuable opportunities to attend academic domestic and international conferences, which is extremely useful for the research.

I would also like to express my gratitude to Assistant Professor Tottori Naotomo for his help and guidance in seminars, conferences and experiments.

I am deeply grateful to Mr. Shibiya Shogo from Panasonic Corporation for giving useful advices on the droplets formation in Chapter 5.

I would like to thank Semiconductor and MEMS Process Division, Open Facility, Tokyo Tech, for device fabrication.

I would also like to thank Materials Analysis Division, Open Facility, Tokyo Tech, for sample analysis.

In addition, I want to thank the following professors who gave me valuable advice and guidance during preparing thesis manuscript and presentation:

Tokyo Tech, Institute of Innovative Research, Professor Hatsuzawa Takeshi.

Tokyo Tech, Institute of Innovative Research, Professor Shinshi Tadahiko.

Tokyo Tech, Institute of Innovative Research, Professor Yanagida Yasuko.

Tokyo Tech, School of Mechanical Engineering, Associate Professor Ishida Tadashi.

I also want to thank all the doctoral and master students of Nisisako lab.

Finally, sincerely thanks to my parents for their great confidence in me all through these years.

2021 年 1 月

Tokyo, Japan

Achievements

Peer-reviewed journals

1. **Siyuan Xu**, Takasi. Nisisako, "Surfactant-laden Janus droplets with tunable morphologies and enhanced stability for fabricating lens-shaped polymeric microparticles", *Micromachines* 12, 29 (2021).
2. **Siyuan Xu**, Takasi. Nisisako, "Polymer capsules with tunable shell thickness synthesized via Janus-to-core shell transition of biphasic droplets produced in a microfluidic flow-focusing device", *Sci. Rep.* 10, 4549 (2020).

International conferences

(口頭発表, 査読有)

1. **Siyuan Xu**, Takasi Nisisako, "Parallel generation of biphasic droplets in microfluidic channels arrayed on slits", *The 18th International Conference on Precision Engineering (ICPE2020)*, H-1-4, Virtual, November 24–26 (2020).
2. **Siyuan Xu**, Takasi Nisisako, "Polymeric particles of controlled morphologies synthesized via microfluidic Janus droplets", *8th International Conference of Asian Society for Precision Engineering and Nanotechnology(ASPEN2019)*, D35, Matsue, Shimane, Japan, November 12–15 (2019).

(口頭発表, 査読無)

1. **Siyuan Xu**, Takasi Nisisako, "Surfactant-assisted morphological tuning of polymer particles synthesized via microfluidic Janus droplets", *International Chemical Engineering Symposia 2020 (IChES 2020)*, T315, Osaka, Japan, March 15–17 (2020).

Domestic conferences

1. 澁谷章吾, 大石公輝, 植田充彦, 前嶋完紀, **Siyuan Xu**, 西迫貴志, マイクロ流路を利用した薄膜多重エマルション生成・噴霧デバイスの開発, 2021 年度精密工学会春季大会学術講演会, オンライン, 3/16‐22 (2021). (発表決定済)

2. **Siyuan Xu**, Takasi Nisisako, Microfluidic synthesis of polymer microcapsules with ultra-thin shell via thermally-induced polymerization. 2019 年度精密工学会春季大会学術講演会, N19, pp.882–883, 東京電機大学東京千住キャンパス(東京), 3/13–15, (2019).

Awards

1. ASPEN2019,　Best Paper Reward,　2019 年 11 月